Thesis presented for the degree of:

LMD Doctorate

Option**:**

Physics of renewable energies

Entitled:

Simulation of cuprous oxide solar cells using SILVACO TCAD

Presented by:

Naceur Khadidja

Jury

Sengouga Nourdine	professor	U.M.K. Biskra	President
Tibermacine Toufik	professor	U.M.K. Biskra	Supervisor
Boumaraf Ramy	MCB	U.M.K. Biskra	Invited
Meftah Afak	professor	U.M.K. Biskra	Examiner
Charifi Zoulikha	professor	Univ M'sila	Examiner

Acknowledgement

Dedication

I dedicate this thesis to:

My great parents, who never stop giving constant love and support,

My dear brothers who encourage and support me,

Also, I dedicate it to all the people in my life who believed in my dream.

الملخص

في هذا العمل، أجرينا دراسة عددية للخلايا الشمسية القائمة على أساس أكسيد النحاس (Cu₂O) باستخدام برنامج المحاكاة Silvaco- atlas. في البداية، قمنا بمحاكاة الخلية Cu₂O / AZO بدون طبقة عازلة حيث كان أكسيد النحاس (Cu₂O) طبقة نشطة (طبقة ماصة) وأكسيد الزنك المشبع بالألمنيوم (AZO) كطبقة نافذة وتمكنا من الوصول إلى اتفاق جيد بين نتائج المحاكاة والقياسات التجريبية لهذه الخلية الشمسية (حيث كانت كفاءتها 2.578 بالمئة). كدراسة ثانية، بناءا على البيانات التجريبية قمنا بدمج أربع مواد مختلفة كطبقات عازلة ZnO و ZMO و AGO و ZGeO بين طبقتي AZO و Cu₂O ، وقارنا النتائج التي تم الحصول عليها مع نتائج العمل التجريبي للتحقق من مدى توافق النتائج المتحصل عليها مع النتائج التجريبية لهاته الخلايا الشمسية، حيث وجدنا أن كفاءة الخلايا الشمسية ارتفعت بشكل ملحوظ من 4.26 إلى 8.72 %، وهو ما يتوافق جيدًا مع القيم المقاسة (4.13 - 8.23 %). كدراسة ثالثة، و من أجل تحسين أداء الخلية الشمسية (ZnO / Cu₂O) تم اقتراح دمج العديد من المواد كطبقات نقل ثقوب (CuI و CuSCN وNiO) ، كما تم تحسين الكفاءة عن طريق تغيير سمك الطبقة الماصة، وكذلك سمك وتركيز المنشطات لطبقة نقل الثقوب، وكذلك تأثير مواد مختلفة من القطب الخلفي. حققت الخلية المحسّنة كفاءة تحويل ملحوظة حيث بلغت 6.36 %. كدراسة أخيرة، قمنا بتحسين كفاءة الخلية الشمسية غير المتجانسة ZGeO/ Cu₂O من خلال دراسة تأثير فجوة الحزمة وتقارب الإلكترون للطبقة العازلة وتأثير تقارب الإلكترون في النافذة الأمامية، في ظل هذه الاعتبارات، كفاءة الخلية تحسنت حيث وصلت إلى 11.30 %.

الكلمات المفتاحية: الخلايا الشمسية، أكسيد النحاس، الوصلات الغير متجانسة، المحاكاة، سيلفاكو–أطلس، التحسين

Abstract

In this work, we have done a numerical study of solar cells based on cuprous oxide (Cu_2O) using the simulation program Silvaco Atlas. In the beginning, we simulated the AZO/ Cu_2O solar cell without a buffer layer where cuprous oxide (Cu_2O) was an active layer (absorber layer) and aluminum-doped zinc oxide (AZO) was a window layer, we were able to reach a good agreement between the simulation results and experimental measurements of this solar cell (where its efficiency was 2.578 %). As a second study, based on the experimental data, we combined four different materials as buffer layers ZnO, ZMO, AGO, and ZGeO between the two AZO and Cu_2O layers, it compared the obtained results with the results of the experimental work, for verify the compatibility of the obtained results with the experimental results of these solar cells, where we found that the solar cell's efficiency has significantly risen from 4.26 % (ZnO) to 8.72 % (ZGeO), which is in good accord with the measured values (4.13–8.23 %). As a third study, in order to improve the performance of the ZnO/ Cu_2O heterojunction solar cell, it was proposed to combine many materials such as hole transport layers (CuI, CuSCN, and NiO). Also, the efficiency was improved by changing the thickness of the absorber layer, as well as the thickness and doping concentration of the holes transport layer, as well as the effect of different materials of the back electrode, where the optimized cell has achieved a remarkable conversion efficiency where it reached 6.36 %.

As a final study, we have improved the efficiency of the ZGeO/Cu_2O heterojunction solar cell through the influence of the bandgap and electron affinity of the buffer layer and the effect of the electron affinity of the front window, under these considerations, cell efficiency improved where it reaching 11.30 %.

Keywords: Solar cell, Cuprous oxide, Heterojunction, Simulation, Silvaco-atlas, Optimization

Table of contents

Chapter 3: SILVACO-ATLAS simulation process

List of figures

List of tables

List of acronyms

Symbol	Description
I_{sc}	Short-circuit current
J_{SC}	Short-circuit current density
V_{OC}	Open-circuit voltage
FF	Fill factor
η	Conversion efficiency
P_{in}	Input power
P_m	Maximum power
ρ	Resistivity
E_g	Band gap energy
I_{ph}	Photogenerated current
I_s	Dark saturation current
q	Electric charge
n	Ideal factor
T	Temperature
R_s	Series resistance
R_{sh}	Shunt resistance
K	Boltzmann constant
μ_n	Electron mobility
μ_p	Hole mobility
PLD	Pulsed-Laser Deposition
ALD	Atomic Layer Deposition
BL	Buffer layer
I_m	Maximum current
V_m	Maximum voltage
ECD	Electrodeposition
TCO	Transparent Conductive Oxide
ZMO	Zinc– Magnesium –Oxide
AGO	Aluminum–Gallium–Oxide
ZGeO	Zinc-Germanium-Oxide
SQL	Schockley–Queisser limit
TCAD	Technology Computer Aided Design

SILVACO	*Silicon valley corporation*
*PC*1D	*Personal Computer One Dimensional*
SCAPS	*Solar Cell Capacitance Simulator*
AMPS	*Analysis of Microelectronics and Photonics Structures*
AFORS − HET	*Automat for simulation of HET ero structures*
HJSC	*Heterojunction solar cell*
MgF_2	*Magnesium Fluoride*
CBO	*Conduction Band Offset*
HTM	*Hole transport materials*
φ	*Metal work function*

General Introduction

General Introduction

The recent noticeable increase in the population around the world led to the need for continuous use of energy sources based on fossil fuels (oil, coal, and gas) as a result of the increasing demand for energy, but this in turn led to the creation of more challenges, including the depletion of fossil fuel reserves, greenhouse gas emissions and other environmental issues, geopolitical and military conflicts, and ongoing fuel price fluctuations. These issues will lead to unsustainable circumstances, which will ultimately put human civilizations in danger that may be impossible to reverse. Despite this, green energy sources which employ renewable energy sources such as wind, biomass, sun, wave, and geothermal are the best option and the only way to address the problems that are getting worse [1]. Of all these energy resources renewable, solar energy is the largest and has the potential to meet all our energy needs, and appears to be the most promising long-term choice, it is the most plentiful, inexhaustible, and environmentally friendly alternative available today [2].

Indeed, in recent times, we have begun to notice the increasing dependence on renewable energies, especially solar energy; this is through enhancing communities' awareness of existing environmental problems, developing their sense of responsibility towards them, and urging them to rely more on it. Where the addition of 200 GW of net worldwide power output using different renewable energy technologies as of 2020 is depicted in Figure 1(a), with solar PV accounting for nearly 60 % of all additions. The International Energy Agency (IEA) anticipates that the capacity of electricity produced by wind and solar PV energy will first surpass the capacity of electricity produced by natural gas in 2023 and will also surpass coal in 2024 due to the growing reliance on renewable energy sources, particularly solar and wind energy (see Figure 1 (b)) [3].
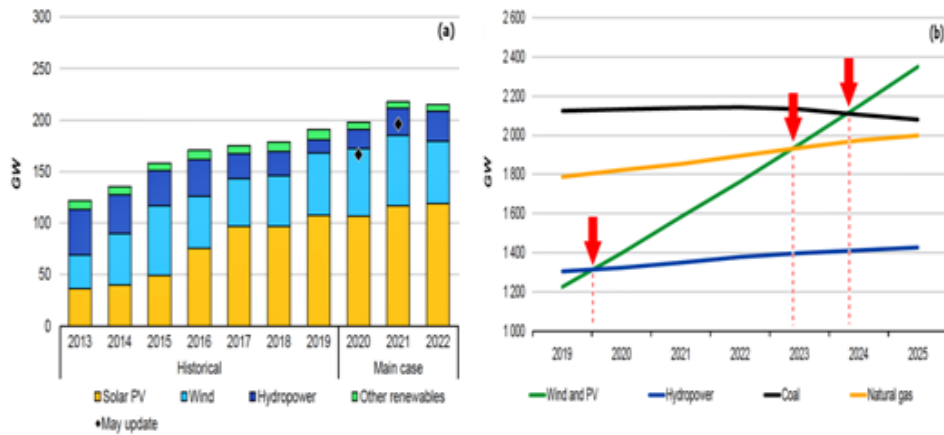
Figure 1: (a) Additions in net renewable power capacity by technology from 2013 to 2022 .(b) Total installed capacity of power by fuel and technology between 2019 and 2025 [3].

In order for photovoltaic cell technology to play a major and competitive role in the energy production market, it must provide electrical energy at an abundant and reasonable price, with the lowest level of environmental pollution compared to traditional electric power plants. Indeed, this is what researchers are racing for, which has led to paying more attention to solar cells based on low-cost materials such as cuprous oxide, although there are new, exciting, and evolving PV technologies like dye-sensitized [4] and perovskite [5] solar cells can achieve high conversion efficiencies [6], but they degrade over time [7]. Furthermore, proven solar cell technologies such as Cadmium Telluride (CdTe) [8], Copper Indium Gallium Selenide (CIGS) [9], and Indium Phosphide (InP) [10] have high conversion efficiencies [10, 11], but are either costly to manufacture or use hazardous or scarce materials (or both) [12-14]. On the other hand, oxide PV cells are chemically stable and can be manufactured cheaply, and which among them is a cuprous oxide (Cu_2O), as it is an abundant and non-toxic material [15] with direct band gap energy [16] and a high absorption coefficient [17, 18]. Cu_2O-based solar cells have achieved conversion efficiencies of around 8% [19], with a theoretical efficiency cap of around 20 % [20]. But the difficulty of the way to make a Cu_2O homojunction [21], that's what led the experts to turn toward the field of Cu_2O-heterojunction solar cell research. This is what we see through there are many reports on heterojunction solar cells based on cuprous oxide (Cu_2O).

In view of the continuous efforts in the field of manufacturing solar cells, simulation of solar cells is necessary and useful before the actual manufacture of them because this will save a lot of effort, money, and time. There are many simulation programs that allow improving the yield of cells before manufacturing, including Silvaco Atlas. This thesis seeks to develop a

model simulation to be used and expanded in the future to assist advanced Cu_2O solar cell developers to make a better solar cell through numerical modeling by SILVACO-ATLAS software for Cu_2O heterojunction solar cells in order to determine the technical and electrical parameters through the optimal construction that provides the highest of efficiency.

The aim of this work is firstly to simulate, using SILVACO Atlas TCAD software, an AZO/Cu_2O solar cell without a buffer layer, then the effect of adding four different buffer layers (ZnO/ ZMO/ AGO/ ZGeO) on its performance. In addition, optimizing the structure of a ZnO/Cu_2O solar cell; for this, we study the effects of different hole transport layers on ZnO/Cu_2O structures and study the effect of other parameters (thickness of both are absorber and HTL layer and doping of HTL,..). And as a final step, we study the effect of changing the different parameters (the band gap of the buffer layer, and electron affinity of both buffer and window layer) for a $ZGeO/Cu_2O$ solar cell structure in order to achieve the optimal construction that provides the highest efficiency.

This thesis is organized into four chapters as follows:

Chapter one

The brief theoretical background of basic semiconductor physics and the base concepts of the PN solar cell are discussed.

Chapter two

This chapter will be an overview of cuprous oxide and its basic properties and deposition methods it's, also will talk about the history and evolution of Cu_2O-based solar cells for both homojunction and heterojunction. Then, the buffer layers used in heterojunction Cu_2O-based solar cells and their properties will be discussed. As well as the Challenges associated with the poor performance of Cu_2O-based solar cells will be discussed briefly.

Chapter three

This chapter will provide an explanation of the simulation program Silvaco-Atlas that is used in this study and everything related to its basics of working, as well as the various commands and instructions needed in it.

Chapter four

In this chapter, we present the results of the simulation and optimization of the cuprous oxide (Cu_2O) solar cell and the details of our results, and the discussion of it.

Chapter 1

Fundamental of semiconductors and solar cells

1.1   Introduction

Most modern electronic devices depend in their work on materials with distinctive physical and chemical properties, namely semiconductors, which possess the properties of insulators at low temperatures and have the ability to conduct electricity when their temperature rises to a certain extent. Extensive research began to identify the structural, optical, and electrical properties of these materials and the possibility of making maximum use of them in practice, as this research resulted in the manufacture of resistors, diodes, and transistors. And then solar cells, as well as the manufacture of integrated electronic circuits, which is the modern background of the transistor Thus, the field of semiconductor physics has become one of the most important fields of applied physics, which is still developing and advancing with rapid steps until it has entered most areas of daily life. Recently, it has become increasingly used in the manufacture of solar cells, thus becoming semiconductors of the most important materials used for the manufacture of electronic and optoelectronic devices. The future is still promising to use these materials more and more. In this chapter, we will address about semiconductors and will explain the most important knowledge that must be known about semiconductors, including definitions, types, characteristics, and others, we will also discuss solar cells and their characteristics in detail.

1.2   Theoretical aspects of semiconductors

A metal, a semiconductor, and an insulator are types of materials. There are two common ways to categorize a material and distinguish between them. The first way to tell them apart is by their electrical resistance at room temperature. An insulator's resistivity ranges from 10^8 to 10^{18} (Ω cm), while semiconductors' resistivities range from 10^{-3} (Ω cm) to 10^8 (Ω cm). Metals (conductor), on the other hand, have much smaller resistivities where it has a resistivity between 10^{-3} and 10^{-8} (Ω cm) [22], as shown in Figure 1.1.
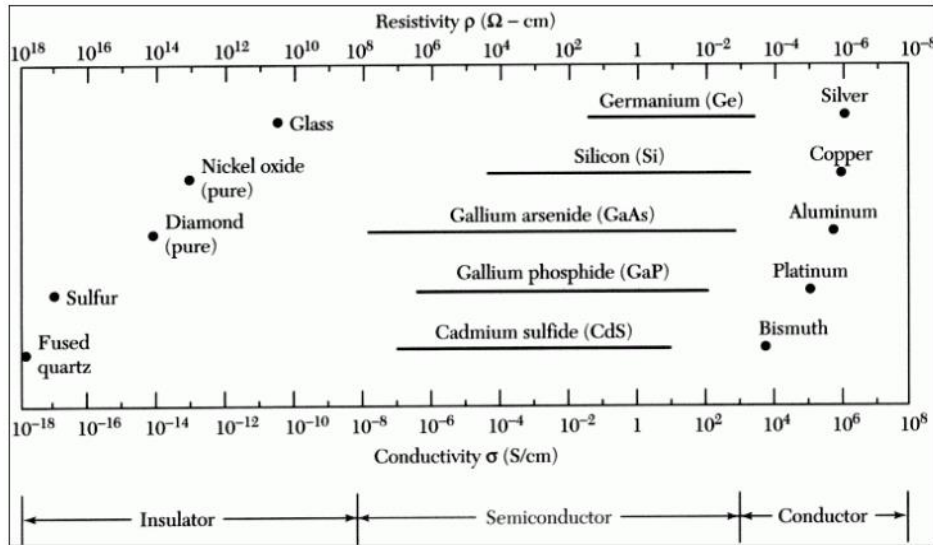
Figure 1.1: Resistivity for different type of material [22].

The second way to classify them is by the importance of their bandgap value where the energy difference separating the conduction and valence energy bands of material is known as the bandgap. "The bandgap Eg" [23], also known as the "forbidden band", contains no permitted energy levels for electrons to occupy [24]. Bandgap differences between conductors, semiconductors, and insulators are shown in Figure 1.2. For conductors (metal), the conduction and valence bands overlap, leading to no bandgap. Electrons are free to move immediately at any temperature above absolute zero, as they do not require any energy to be freed from the valence band. Semiconductors behave like insulators at 0 K, through a packed valence band and an empty conduction band separated by a bandgap. Since valence electrons must gain energy equal to or greater than the bandgap to conduct charge, conductivity within the material increases exponentially with temperature [23, 24], whereas in insulators; the full valence band and empty conduction band are separated by a large band gap.
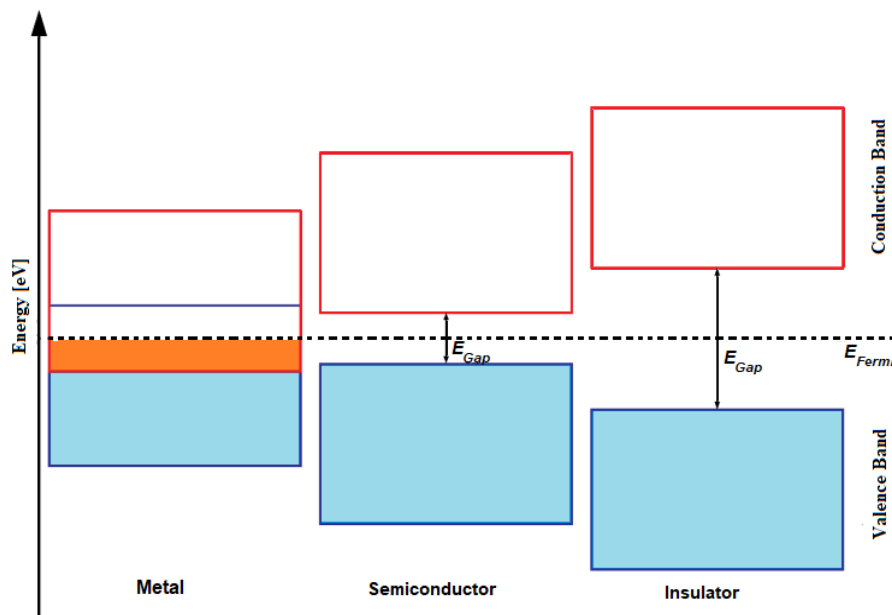
Figure 1.2: The energy bands of (a) metal (conductor), (b) semiconductors, and (c) insulators.

A basic property of semiconductors is the difference between the valence and conduction bands, or "gap." Figure 1.3 shows the transitions that can be made based on the gap's type. When a semiconductor material is exposed to external excitation, such as an incoming photon with an energy E equal to hυ higher than the material's gap energy, an electron can cross from the valence band to the conduction band which means that in this case, the photon can be easily absorbed and will then, in general, create a single electron-hole pair. Unlike if the energy of the photon is not high enough to be absorbed. The photon will either be reflected or absorbed elsewhere, and its energy is lost.

As for the interaction between the incoming light and the semiconductor itself, when an incoming photon may be absorbed directly without the interaction of a phonon within the semiconductor, the semiconductor has a "direct gap" where the valence band's maximum corresponds to the conduction band's minimum in this case as shown in Figure 1. 3 (a). And on the other hand, when an incoming photon can only be absorbed through interacting with a phonon within the semiconductor, the semiconductor is said to have an "indirect gap" where the maximum of the valence band does not match the minimum of the conduction band because a phonon must now be emitted (or absorbed) for a photon to be absorbed in this second case as shown in Figure 1.3 (b).
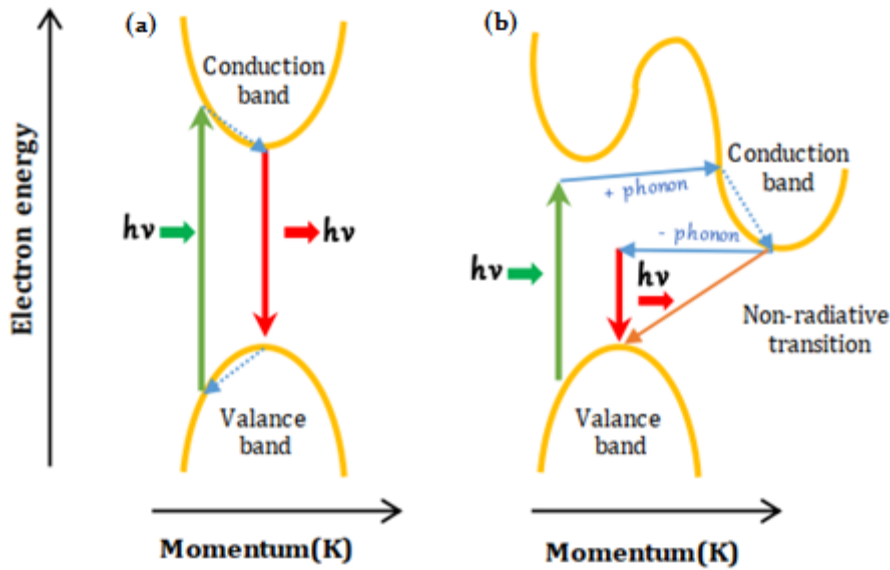
Figure 1.3: Direct and indirect electron excitations in semiconductors. a) Direct bandgap. b) Indirect bandgap.

1.2.1 Types of semiconductors

1.2.1.1 Intrinsic and Extrinsic type of semiconductors

Intrinsic and extrinsic semiconductors are two major categories of semiconductor materials. Intrinsically semiconductors are semiconductors that are chemically pure, or devoid of impurities [22]. Undoped semiconductors or "i-type semiconductors" are other names for these materials. The quantity of holes and electrons is thus governed by the material's characteristics rather than the amounts of the impurity species present. In an intrinsic semiconductor, the conductivity depends on the ambient temperature where room temperature, allows a very small amount of current to flow due to high resistance. Adding certain impurities to intrinsic semiconductors can drastically change their conductivity.

Extrinsic semiconductors are those that have impurities added to them also called 'impurity' or 'doped' semiconductors [25], where the impurities are introduced into semiconductor materials in a targeted manner to manipulate their electrical properties. It makes it more suitable for electronic devices. The process of adding impurities is called doping, and the atoms used as impurities are called dopants. And depending on that, the extrinsic semiconductors are further classified into p-type and n-type semiconductors [25].

A dopant atom whose outer layer is rich in electrons will tend to introduce excess electrons vis-à-vis the rest of the lattice and induce n-type doping, while a dopant atom poor in electrons will tend to introduce holes and induce p-type doping. The best-known example is that of silicon, which can be n- or p-doped with phosphorus and boron respectively. The silicon atom has 4 electrons in its outer shell, each of which can pair with an outer electron of another nearby silicon atom to form a covalent bond. In total, each silicon atom then has 8 electrons in its outer shell and respects the octet rule. Phosphorus in its outer shell has 5 electrons. By replacing a silicon atom with a phosphorus atom, it appears that the latter can only bind to 4 silicon atoms and therefore only 4 electrons from the phosphorus can form a covalent bond with a silicon atom. The phosphorus atom will be surrounded by 9 electrons and not 8, including a weakly bound electron. The latter can easily be excited towards the conduction band and thus become a free electron participating in the conduction of the material: the phosphorus atom has introduced an electron potentially available for conduction and therefore n-type doping. Conversely, boron has only 3 electrons in its outer layer, so when these are included in silicon, it can bond with 4 silicon atoms but one of the 4 bonds will only be with a single electron. It will therefore miss an electron compared to silicon, so a hole has been introduced. This gap can be filled by an electron coming from another bond, but this other bond will then present a gap: the gap has moved, which means that the hole has moved. The introduction of boron, therefore, introduced a mobile hole in the material and consequently p-type doping (Figure 1.4 and Figure 1.5).
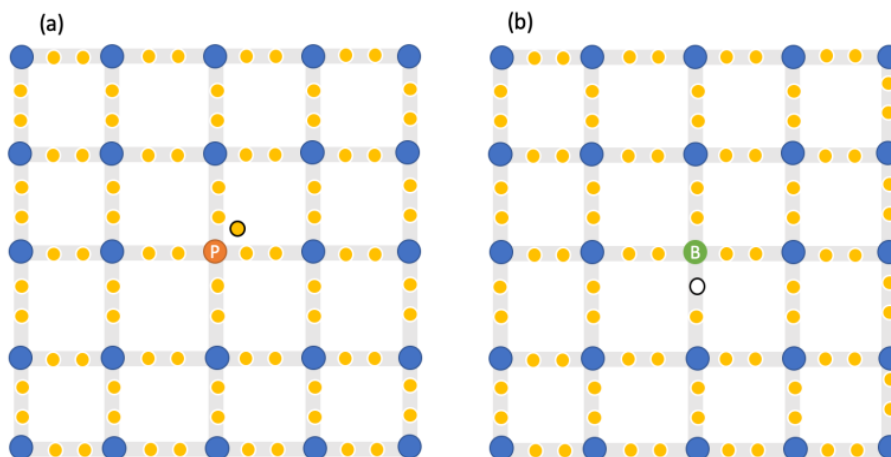
Figure 1.4: A simplified diagram of extrinsic semiconductors (a) phosphorus-doped n-type semiconductor. (b) boron-doped p-type semiconductor.
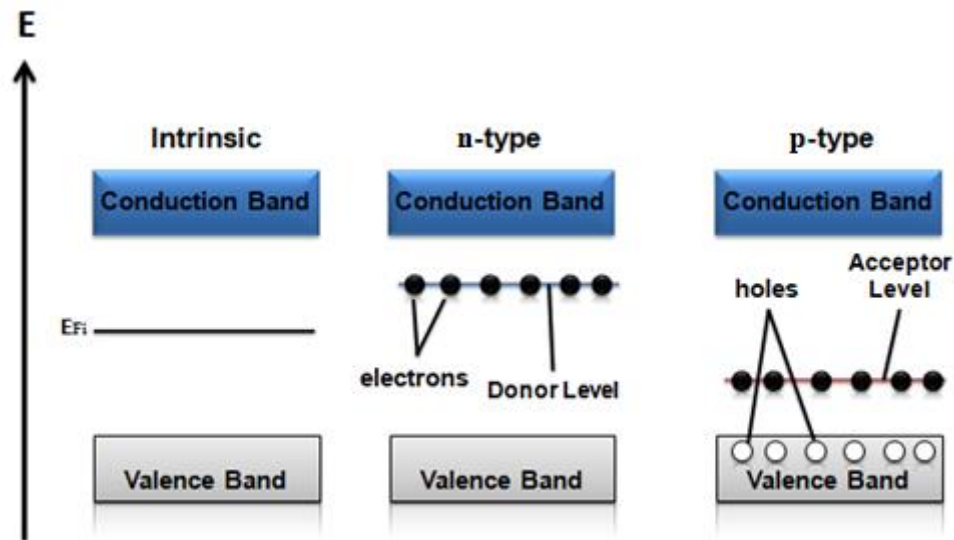
Figure 1.5: Diagram of energy bands of intrinsic semiconductors and extrinsic semiconductors with n and p type doping.

1.3 P–N Junctions in solar cells

1.3.1 History of Solar Cell

The story of the solar cells goes back to an early discovery of the photovoltaic effect, it was in 1839 [26] when Edmund Becquerel discovered this phenomenon where he noticed a silver-coated platinum electrode submerged in electrolyte created an electric current when it was exposed to light [26, 27]. After that, Charles Fritts built the first true solar cells utilizing selenium in 1883 [28]. The devices developed by Fritts were inefficient, converting less than 1% of absorbed light into electrical energy. Then, Russell Shoemaker Ohl made the next big advancement in solar cell technology in 1941; he developed the silicon solar cell [29], which was about one percent efficient [30].

In 1954, three more researchers "D.M. Chapin, C.S. Fuller, et G.L. Pearson" working at Bell Labs, demonstrated a silicon solar cell when used in direct sunlight, gives 6 % energy-conversion efficiency [30, 31]. Within a few years, solar cells were commonly used to power satellites, and other applications followed, where improvements in solar module manufacture, performance, and quality contributed to lowering the cost in the 1970s. This opened up a lot of possibilities for powering remote terrestrial applications, such as navigational aids, signals, telecommunications equipment, and other low-power requirements. Following the energy

crises of the 1970s, substantial efforts were made to create solar power systems for home and commercial purposes.

1.3.2   **Basics of Solar Cells**

A solar cell is an electronic device that directly converts solar radiant energy into electricity using the photovoltaic effect, when light hits a solar cell, an electric current flows through the material and produces electricity [32]. Radiant intensity, the spectral distribution of radiation, light-absorbing materials, and the design of external circuits are all key elements of this process. For effective photovoltaic energy conversion, semiconductor materials in the form of pn junctions are also necessary. The production of p-n junctions and basic concepts of semiconductor materials are first discussed in order to comprehend the operating principle of conventional photovoltaic devices.

Joining p-type and n-type semiconductor materials result in a p-n junction. The junction is considered a homojunction if the connecting components are made of the same material. And heterojunction refers to a junction that is made up of two distinct components. When an n-type material comes into contact with a p-type material, the n-type material's electron mobile tries to diffuse through the junction and fill the p-type material's holes. Similarly, the holes in the p-type side will diffuse toward the n-type material and fill the electrons [33, 34]. Meanwhile, these charges leave behind immobile ions that have a negative charge on the p side and a positive charge on the n side around the junction. These immobile charged ions provide an electric field that acts against the movement of electrons and holes through the junction, pushing mobile positive charges toward the p-type material and mobile negative charges toward the n-type material [34]. The electric field builds up as the diffusion process continues, until bringing the passage of charged carriers through the junction to a halt. As a consequence, there creating of a depletion region at the junction, however, some charge carriers may have sufficient energy to cross through this region by diffusion, even in thermal equilibrium [34]. This creates a so-called diffusion current, which they become minority carriers before recombination. Then, when minority charge carriers reach the edge of the depletion region, it is swept by an electric field and produces a so-called drift current. In equilibrium, the drifts current and the diffusion current is exactly balanced for both electrons and holes, as shown in Figure 1.6. The net current through the device is zero [33].
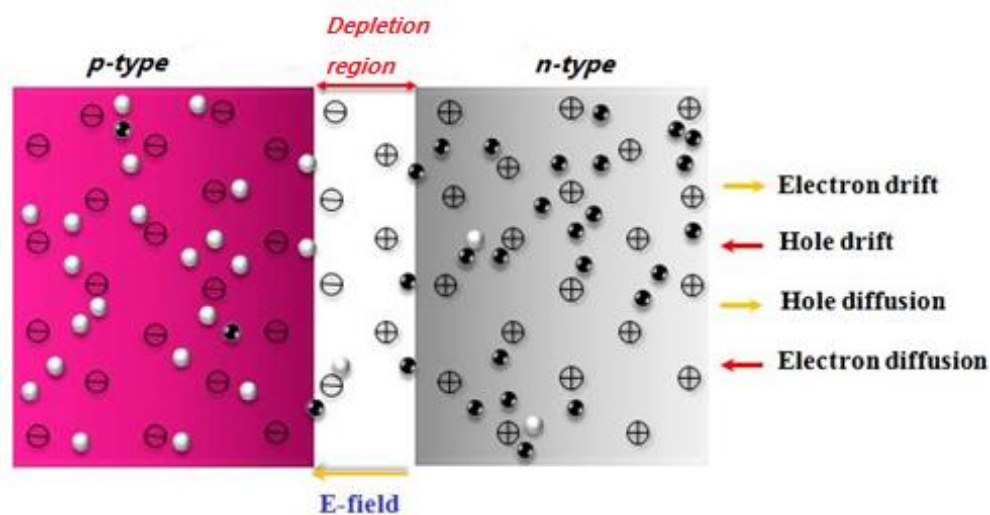
Figure 1.6: The p-n junction.

When a bias voltage is applied externally across the p-n junction, where the p-type semiconductor is connected to the positive side whereas; the n-type semiconductor is connected to the negative side. So, the junction is in a forward-biased case as shown in Figure 1.7 (a). In this case, the voltage source's applied electric field is in the opposite direction of the built-in electric field in the depletion zone. It is also weakening the net electric field, thus the barrier to the diffusion of the charge carriers from one side of the junction to the other is reduced. The diffusion current rises as a result of this. Since the external circuit supplies the bulk of the carriers, a net current flows under a forward bias voltage. While in the reverse bias state (Figure 1.7 (b)), the negative side is connected to the p-type semiconductor, while the positive side is connected to the n-type semiconductor, wherein the width of the depletion region rises with the increase of barrier potential, the applied electric field by the external voltage source is in the same direction as the built-in electric field the depletion region, this leading to the increased electric field, which reduces the diffusion current because the probability that charge carriers diffuse is reduced [33].
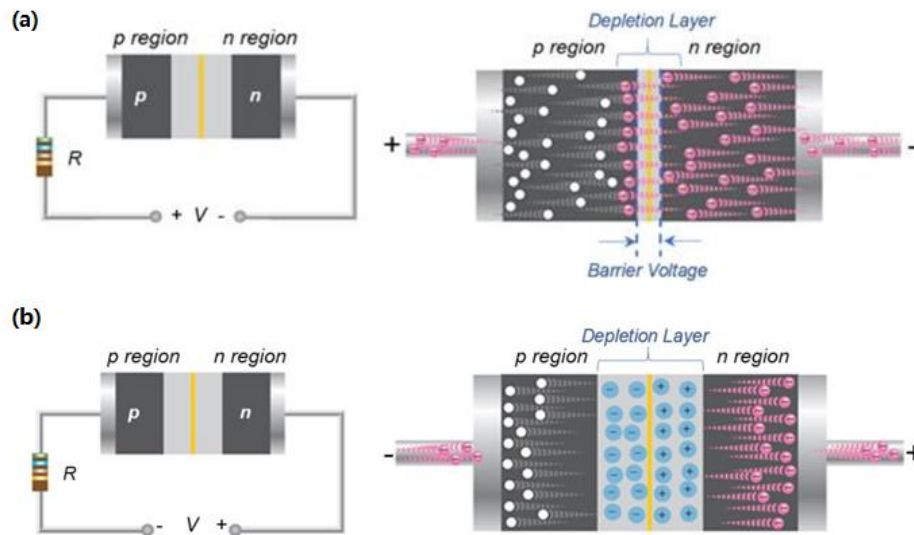
Figure 1.7: (a) Forward biased pn junction (b) Reverse biased pn junction.

The illumination on the p-n junction creates electron/hole pairs in the depletion region, due to the "built-in" electrical field in this region, the photo-generated holes and electrons will move toward the p-side and the n-side, respectively [29]. As a result, the p side accumulates more holes, while the n side accumulates more electrons. This charge separation creates an electric field at the p-n junction that is in contrast to the one already present, lowering the net electric field and increasing the diffusion current. Preventing the photogenerated carriers from leaving the photovoltaic device raises the forward bias of the p-n junction to a level where the photogenerated current is equal to the forward bias diffusion current and the net current is zero.

When an external load is added to the device, the photogenerated electrons are provided an external direction while the holes remain trapped in the p-type semiconductor. The electrons will flow from the n-side to the load, where they will recombine with holes waiting on the p-side to complete the circuit. In this case, the p-n junction's forward bias decreases to the point that the photogenerated current equals the load current. Since the net electric field around the p-n junction increases, the diffusion current decreases (Figure 1.8).
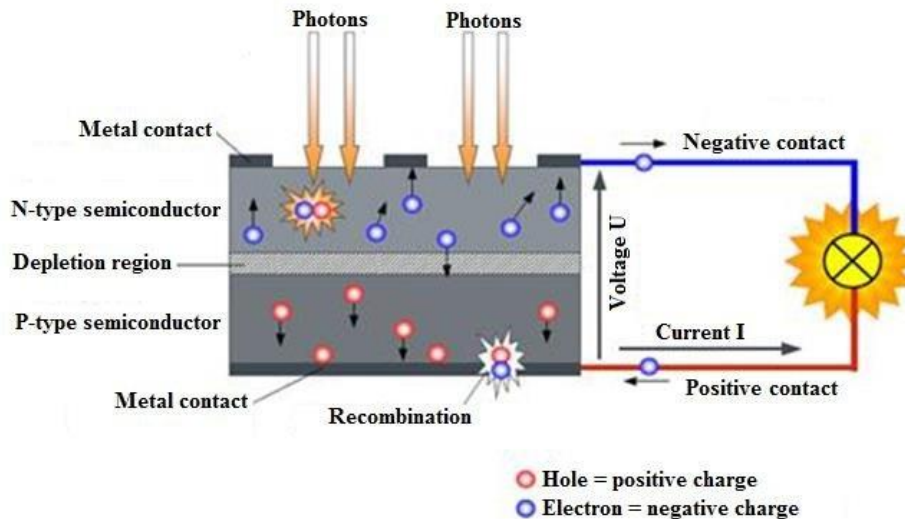
Figure 1.8: Schematic representation of a photovoltaic cell [35].

1.3.3   Solar cell output parameters

Figure 1.9 (a) displays the dark and illuminated J-V curves produced by the solar cell. The output power is often plotted on the illuminated J-V curve in the first quadrant, where the performance of a photovoltaic device is primarily characterized by the illuminated (J-V) curve, as seen in Figure 1.9 (b). It is used to extract the output parameters of the solar cell including the short circuit current density (Jsc), open-circuit voltage (Voc), maximum power (Pm), fill factor (FF), and efficiency (η). Since are all these important parameters to consider when evaluating the performance of a solar cell i.e. these parameters are the key used to characterize the performance of solar cells.
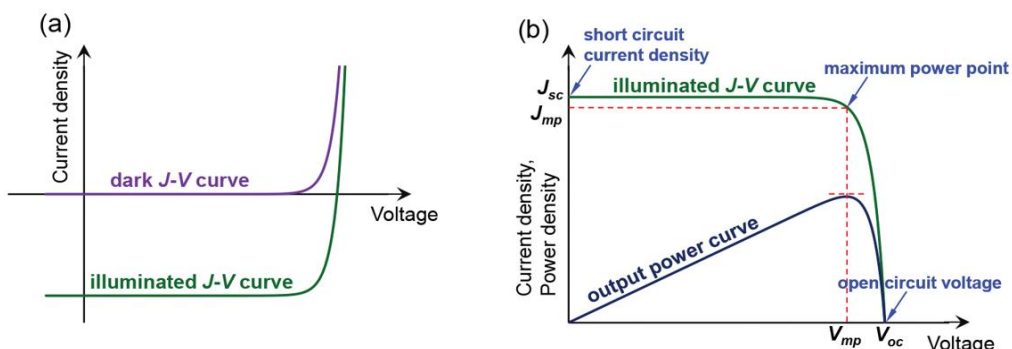
Figure 1.9: (a) J-V curves of the solar cell in the dark and under illumination. (b) A typical illustration of an illuminated J-V curve and a output power density curve as a function of voltage [36].

Chapter 1: Fundamental of semiconductors and solar cells

1.3.3.1 Short circuit current I_{sc}

The short-circuit current (I_{sc}) is the current flowing in the cell under illumination and by shorting the terminals of the cell (when the voltage across the device is zero) where it is the maximum current, which can be obtained from a solar cell. The flow of I_{sc} is due to the generation and collection of light-generated carriers. It mainly depends on the number of incident photons as well as the spectrum, area of the solar cell, optical properties, and the collection probability of photogenerated carriers [37]. The graphical representation of I_{sc} is given in Figure 1.9 (b).

1.3.3.2 Open circuit voltage V_{oc}

The open-circuit voltage (Voc) is the maximum voltage obtained from a solar cell. When a solar cell is open-circuited and no load is connected across it, the current will be at its minimum (zero), while the voltage is at its highest [37, 38]. Voc corresponds to the forward bias voltage, at which the photocurrent density is compensated by the dark current density. If the net current is zero, Voc depends on the photo-generated current density [39] and can be calculated using the below Equation [40, 41], the schematic of the open-circuit voltage on the I-V curve is in Figure 1.9 (b).

$$I_T = I_{ph} + I_d \tag{1.1}$$

$$I_T = I_{ph} - I_S \left[exp\left(\frac{qV}{nK_BT}\right) - 1 \right] \tag{1.2}$$

When; $I_T = 0, V = V_{OC}$ we find:

$$V_{OC} = \frac{nK_BT}{q} ln\left[\left(\frac{I_{ph}}{I_S}\right) + 1 \right] \tag{1.3}$$

Where;

I_{ph}: Photo-generated current by the solar generator under illumination (A).

I_d: The direct current of a solar cell (A).

V: Voltage across the cell (V).

I_S: Saturation current of the solar cell (A).

K_B: Boltzmann constant and equal $1.38 \times 10^{-23} J/K$.

n: Ideal factor of the solar cell.

T: Temperature (K).

q: Electric charge (C).

1.3.3.3 Maximum power P_m

The output power of the cell (or generator) is the product of the output current delivered by the latter and the voltage across its terminals, and is defined as:

$$P_{out} = V_{out} \times I_{out} \tag{1.4}$$

Under short and open circuit conditions, no power is generated. The power output will be zero if both or anyone will be zero. The power between these two points is positive and the maximum power point (PPM) of coordinates obtained for $V = V_m$ and $I = I_m$ [42] so we get

$$P_m = V_m \times I_m \tag{1.5}$$

1.3.3.4 Fill factor FF

The fill factor (FF) is the ratio of the maximum produced power (Pm) by the solar cell to the product of open circuit voltage V_{OC} and short circuit current I_{SC} [37]. As given in the below equation:

$$FF = \frac{P_m}{I_{SC} \times V_{OC}} = \frac{I_m \times V_m}{I_{SC} \times V_{OC}} \tag{1.6}$$

Where, V_m = Voltage at the maximum power point,

I_m = Current at the maximum power point,

V_{OC} = Open circuit voltage

I_{SC} = Short circuit current.

1.3.3.5 The Conversion efficiency η

The performance of a photovoltaic device is usually indicated by its power conversion efficiency (η), which is one of the most important parameters considered while assessing the performance of solar cells. Where the efficiency represents the ratio between the electrical power generated by the cell and the photovoltaic power it receives [29]. This parameter is calculated by [43]:

$$\eta_{photovoltaic} = \frac{P_m}{P_{int}} = \frac{I_m V_m}{P_{int}} = \frac{I_{SC} \times V_{OC} \times FF}{P_{in}} \tag{1.7}$$

Where:

$$P_{int} = E \times S \tag{1.8}$$

E: The intensity of illumination in W/cm^2

S: The area of the solar cell.

1.3.4 Losses in solar cells

Simply put, efficiency is a measurement of the amount of power that can be obtained from a solar cell, and of course, to be cost-effective, it would be desirable for the solar cell to be highly efficient. In the ideal case, the efficiency of the solar cell will be 100 %, as each photon impacting the surface of the solar cell transmits its whole energy to an electron-hole pair, and all carriers keep the absorbed energy and send it to the contacts of the device. There would be the solar cell with no losses in this circumstance. In fact, in practice no solar cell is ideal. This is due to many loss processes lowering the potential efficiency of a solar cell. Below we will mention some of these mechanisms:

1.3.4.1 Optical losses

Optical losses reduce a solar cell's efficiency by decreasing the short circuit current and preventing the creation of an electron-hole pair for each photon that strikes its surface [44]. Following is a summary of the causes of optical losses:

- Reflection of the light at the interfaces between the several solar cell layers as well as the reflection of light from the solar cell's first layer.
- When the top electrode shades the solar cell's active surface, light is reflected rather than allowed to enter [45].
- Long-wavelength photon transmission through the absorber.

1.3.4.2 Recombination

The recombination is the major cause of the loss of photo-generated carriers and due to this overall efficiency of a solar cell is affected, where some of the charge carriers that are produced are not collected at the electrodes; instead, some of them recombine, such as when an electron and a hole combine to send a photon. And this is what affects the current, I_{sc}, and the V_{OC}. Recombination typically takes place in the bulk, at the interfaces, and at the junction's surfaces. Charge carriers recombine at lattice defects or impurity atoms with energy transition levels inside the semiconductor's bandgap [46, 47].

1.3.4.3 Thermalization

In single-junction solar cells, where photons with energies greater than the bandgap energy of the absorbing layer form electron-hole pairs, thermalization loss is one of the main losses. Heat in the semiconductor network is produced from the excess (extra) energy received by the electron-hole pairs from the photons. This is known as the loss of energy by thermalization [48]. The bandgap should be as large (wide) as possible to reduce the effect of thermalization [49].

1.3.4.4 Electrical losses

1.3.4.4.1. Series and shunt resistance effect

Figure 1.10 shows an example of an equivalent circuit of a solar cell with one diode, where the solar cell can be seen as a current generator, the current is produced by injection from light. To better analyze the electrical behavior of the solar cells, the equivalent electrical model based on electrical components is been created. This circuit is composed of a current source, a p-n junction diode, and a shunt resistor (R_{sh}) in parallel along with a parasitic series resistor (R_s).
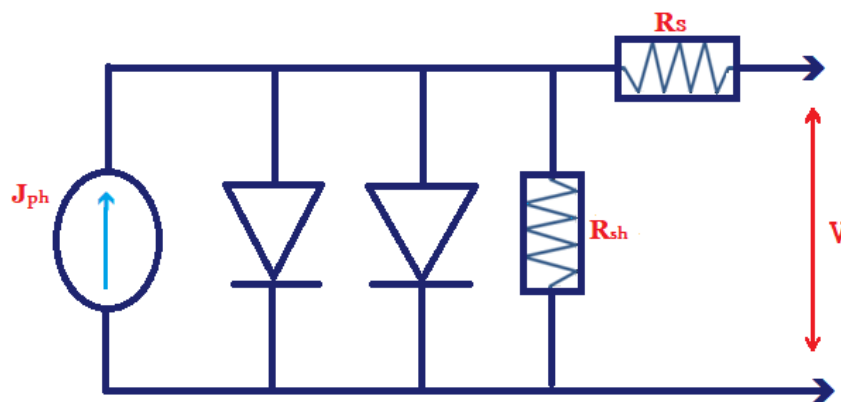
Figure 1.10: Equivalent circuit model for a photovoltaic device.

When characterizing a solar cell, the shunt and series resistances (R_{sh} and R_s, respectively) are two key factors to determine. This due to series resistance R_s is a description of the ohmic losses in the solar cell's front contacts and the metal-semiconductor interface. On the other hand, shunt resistance R_{sh}, represents leak currents at the solar cell's edges and anywhere a short circuit of the p-n junction occurs [23], where low R_{sh} causes solar cell power losses than the quantity of current flowing through the solar cell junction and the voltage generated by the solar cell are both reduced as a result of this type of diversion. The R_{sh} effect is more

pronounced at low light levels because there is less light-generated current. As a result, the losses in this current to the R_{sh} have a greater impact.
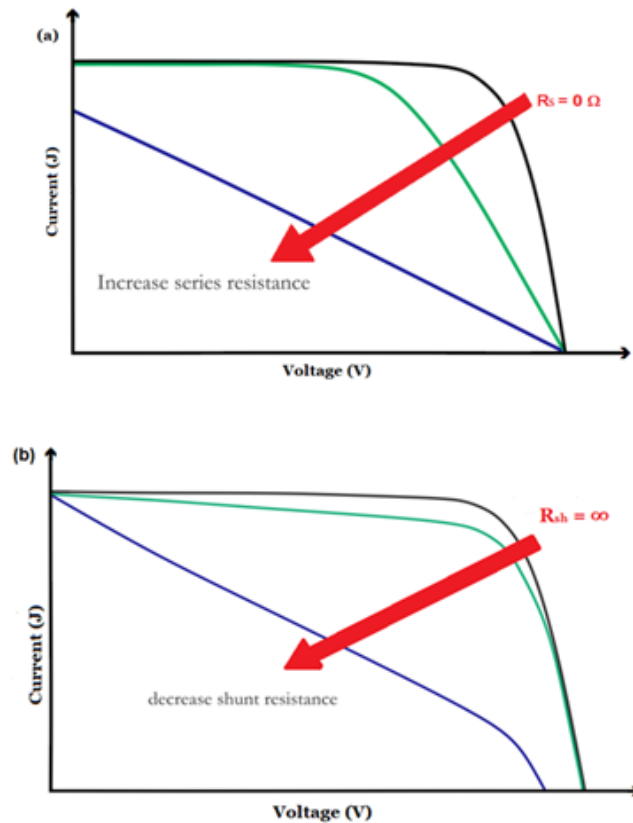
Figure 1.11: Effect of (a) series resistance and (b) shunt resistance on solar cell performance.

From the figure, we can indicate that the shunt and series resistances have a significant influence on the module's output characteristic, the major effect of both resistances is to influence the Fill-Factor [23], although, at a high-value Rs and a low-value R_{sh}, they can also reduce the Voc and Isc, respectively [42, 50, 51].

Chapter 2

Cuprous oxide material and solar cell

Chapter 2: Cuprous oxide material and solar cell

2.1. Introduction

Among the metal oxides, cuprous oxide (Cu_2O), which has long been researched, where was one of the first materials, other than selenium, to be recognized as a semiconductor. Also, and it is desirable since they are affordable, non-toxic, and widely available on earth [15, 18, 52], It also has several interesting characteristics i.e. a good absorption coefficient [17, 18, 53], good mobility of the charge carriers [20], and a diffusion length of the minority carriers of a few micrometers. Also, it has many advantageous optical and electrical characteristics that it has a significant impact on cell performance. All these combined properties enable Cu_2O material to be a serious candidate for several applications between it is solar cells [54]. Especially, current research is increasingly focused on their usage as a p-type absorber layer in cuprous oxide-based solar cells. This chapter is a review of the fundamental properties of copper oxides, including some debating points, and also the methods of deposition and we discussed a review of the Cu_2O-based solar cell, as well as some disputed issues and current developments in cuprous oxide-based solar cells.

2.2. General Presentation

Cuprous oxide (Cu_2O) material exists in natural form, under the name "Cuprite" [55], it is also one of the principal oxides of copper. Among the transition metal oxides, it is stable, abundant, low cost, and non-toxic [56]. It is a solid that can have a yellow or red appearance, depending on the size of the particle.

Cuprous oxide is one of three stable copper oxides together with Cupric oxide with the mineral name tenorite (CuO) and Paramelaconite (Cu_4O_3) [55] it is a transitional phase between cuprite and tenorite, which represents a potential energetically very close to those of CuO and Cu_2O [57]. According to the literature, this phase is a metastable mixed-valence intermediate compound between Cu_2O and CuO [58].

Cu_2O, Cu_4O_3, and CuO all have crystal symmetries that range from cubic to tetragonal and monoclinic, which gives rise to their diverse range of optical and electrical characteristics [59], where Figure 2.1 shows the natural forms of the three oxides with a drawing showing their structures.
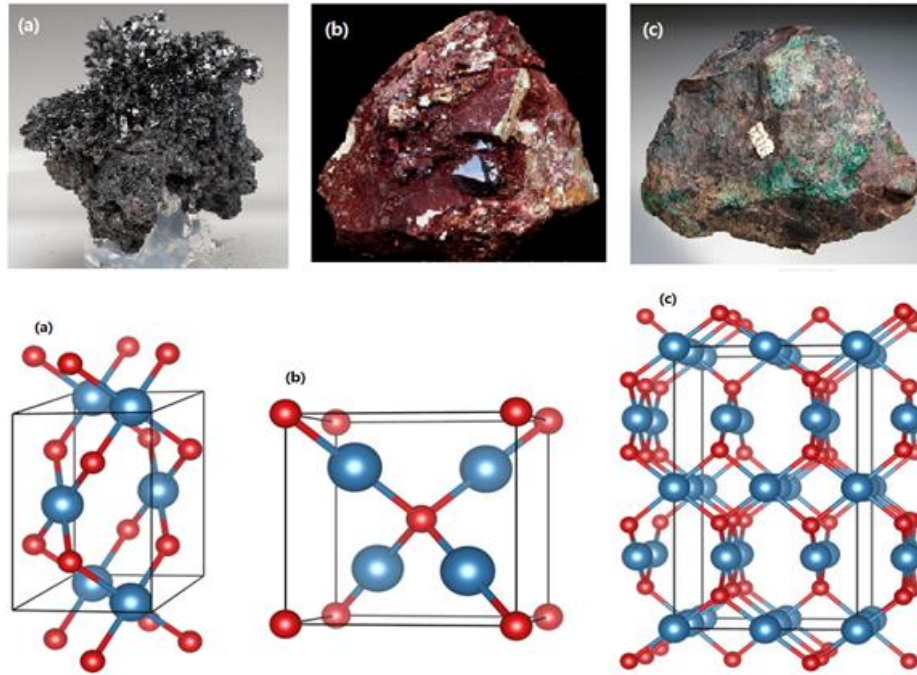
Figure 2.1: Crystal natural and structure of copper oxide compounds: (a)

CuO, (b) Cu_2O, and (c) Cu_4O_3 [55, 60].

2.3. Basic Properties of Cu_2O

Cu_2O is a semiconductor material with a band gap of 2.1 eV and p-type conductivity [2], although it is insoluble in water [61]. Unlike most other metal oxides, it Cuprous oxide is a reddish solid with a density of 6.0 g/cm^3. And it has a melting point of 1235°C.

The material's structural, electrical, optical, and thermal properties are often necessary when material selection and processing decisions are being made during the design of a device. As shown in Table 2.1 the basic properties clarify the identity of Cu_2O also its physical and crystallographic properties.

Table 2.1: Physical properties of Cu_2O [54, 55, 61].

Properties	value
Density	6 g/cm^3
Molar volume	23.44 (cm^3.mol^{-1})
Melting point	1235 °C
Relative permittivity	7.5
Specific heat capacity (Cp)	70 J/(K mol)
Thermal conductivity (k)	4.5 W/(K m)
Thermal diffusivity (α)	0.015 cm^2/s
Molecular mass	143.092 g/mol
Solubility	Insoluble in water

2.3.1. Structural properties

The crystal structure of Cu_2O is the cubic cuprite structure and belongs to $Pn\overline{3}m$ space group, which incorporate a full octahedral symmetry, the structure can be viewed as two sub-lattices, a bcc oxygen sub-lattice interpenetrating an FCC copper sub-lattice that has been translated by a (1/ 4; 1/4; 1/4), where lattice parameter 4.2696 Å [62], as represented in the Figure 2.2.
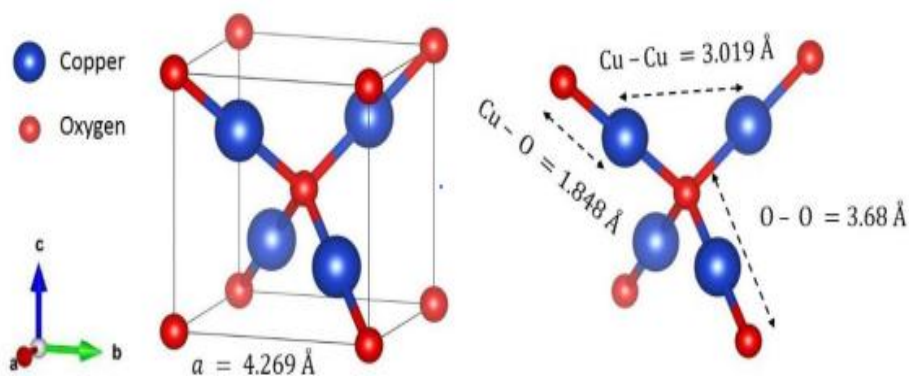
Figure 2.2: Crystal structure of cuprite Cu_2O.

Chapter 2: Cuprous oxide material and solar cell

2.3.2. Native defects in bulk Cu_2O

Figure 2.3 depicts the formation of native point defects, such as copper (V_{Cu}) and oxygen (V_O) vacancies, copper (Cu_O) and oxygen (O_{Cu}) antisites, and copper ($Cu_{i(oct)}$, $Cu_{i(tet)}$) and oxygen ($O_{i(oct)}$ and $O_{i(tet)}$) interstitials, at two different sites, the octahedral (with subscript "oct") and tetrahedral (with subscript "tet"). The interstitial atom at the octahedral interstitial site is surrounded by six Cu atoms, whereas the tetrahedral interstitial site is surrounded by four Cu atoms. An antisite is formed when a Cu atom is replaced with an O atom, and vice versa, i.e., oxygen in a metal-atom site.

A so-called copper split-vacancy complex defect, indicated by $V_{Cu}(s)$, was also investigated. This defect is caused by the insertion of an interstitial copper atom between two V_{Cu}, resulting in the formation of a defect complex. This causes a local geometry distortion around the Cu vacancy site, V_{Cu}, in which a copper atom close to a V_{Cu} is structurally pushed toward the unoccupied site and gets coordinated to four oxygen atoms (i.e., two of which were previously coordinated to the displaced copper atom) [63].

Copper oxide is naturally p-type. Excess oxygen, exhibited as oxygen interstitial, O_i, or copper vacancies, V_{cu}, is the primary source of p-type conductivity in copper oxide [64].
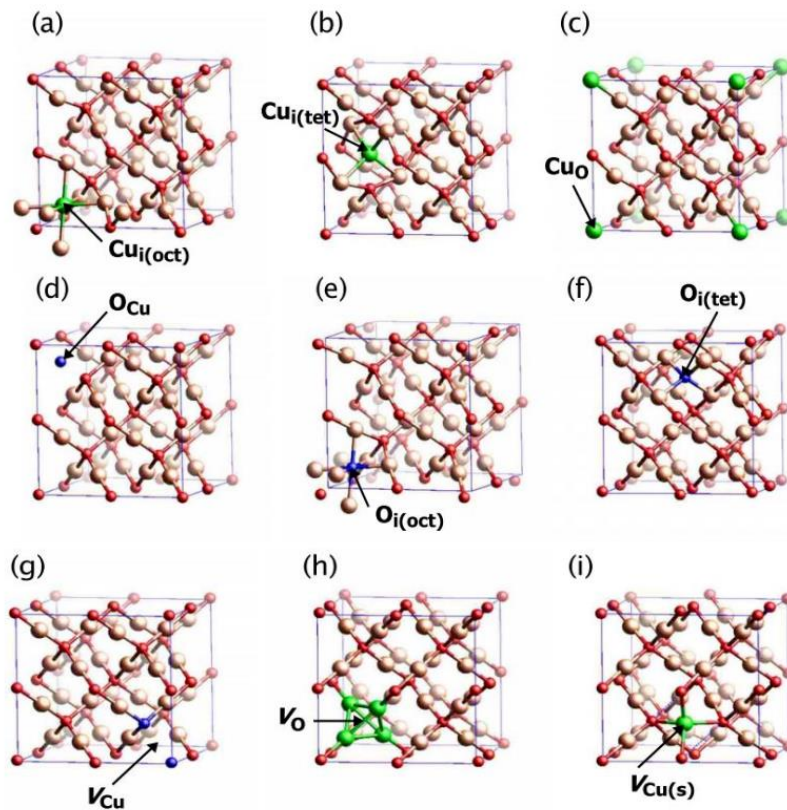
Figure 2.3: Native defects in cuprous oxide super-cell with optimized atomic geometry: a) $Cu_{i(oct)}$, b) $Cu_{i(tet)}$, c) Cu_O, d) O_{Cu}, e) $O_{i(oct)}$, f) $O_{i(tet)}$, g) V_{Cu}, h) V_O, and (i) $V_{Cu(S)}$. The atoms of copper and oxygen are represented as orange and red spheres, respectively [63].

2.3.3. Dopants

The concomitant low Cu_2O carrier density, which leads to high electrical resistivity and lowers both the fill factor and the efficiency of the cell, is one of the most notable reasons for the cell's restricted performance [65, 66]. To get around this, doping Cu_2O with the right impurity could be the best option where the doping or the addition of an impurity atom plays an important role in the properties of a semiconductor such as conductivity has been greatly improved and the resistivity value in the Cu_2O sheets [67, 68], though the concentration of impurity may be very small. For enhanced the properties of Cu_2O by doping external atoms. There are several prospects for extrinsic acceptors, including sodium, magnesium, calcium, nitrogen and nickel, to name a few. Many transition metals have also been tested as dopants with varying degrees of success, whereas Table 2.2 lists some of these elements.

Table 2.2: Some of the different elements used in the doping of Cu_2O.

Element	Chemical formula	Doping content	Temperature	Methods	Ref
Ca	Ca:Cu2O	1%, 2% ,3%	280°C	nebulizer spray technique (NST)	S. Kumar Jacob et al [69]
Ni	Cu2O:Ni	0%, 0.5% and 2%	500°C	pulsed-laser deposition (PLD)	N. Kikuchi et al [70]
Mn	Mn-doped Cu_2 O	5%	700°C	pulsed-laser deposition	M. Ivill et al [71]
Mg	Cu2O:Mg	5%	450°C	aerosol-assisted metal-organic chemical vapor deposition (AA-MOCVD)	J. Resende et al [72]
N	N-doped Cu2O	0.92 at %	280°C	reactive magnetron sputtering	Wang et al. [73]
Na	Na-doped Cu2O	1.39 at %	60°C	The electrochemical	G. Elfadill et al [74].

2.3.4. N-type Cu_2O

It has been shown to be challenging to obtain n-type conductivity in Cu_2O. Meyer et al [75]. Through the effective mass theory, estimated that the donors in Cu_2O had higher binding energies (266 meV) than the acceptors (156 meV), because of the high intrinsic acceptor concentration and high ionization energy, very large donor concentrations would be needed to overcome the p-type conductivity at room temperature. Despite Cu_2O's inherent p-type conductivity, n-type behavior has been documented in the literature [17, 76-78].

The literature is still divided on the origin of n-type doping. The oxygen vacancies (V_O) [79, 80] and copper anti-sites (Cu_O) [81] are suggested. These were later refuted by a DFT study that found that Cu_2O's n-type behavior cannot be caused by intrinsic defects [82]. They come to the conclusion that the deep transition levels of the intrinsic n-type defects rule out those defects as possibilities. The most intuitive candidate, V_O, is stated no to have a transition in

the bandgap at all, disqualifying him or her for this task. One theory is that the n-type conductivity results from extrinsic impurity doping by substances like Cl or F, which have been suggested as potential donor dopants in Cu_2O [79, 82, 83].

2.3.5. Cu_2O Band Structure

From a work, by Heinemann et al [84]. The Cu_2O band structure was calculated using density functional theory (DFT). This result is shown in Figure 2.4, in the upper image the band structure, and in the lower image the corresponding Brillouin zones for Cu_2O [84]. In the shaded area around point Γ of the band structure, the two parabolic lines represent the valence band (bottom) and the conduction band (top). The gap between these two bands is the Cu_2O bandgap and is approximately 2.2 eV in this image. There is another parabolic band just above the conduction band and the space between that band and the valence band is about 2.6 eV. These two gaps are shown again in Figure 2.5, but in this case, the only point in the Brillouin zones is point Γ. The first gap is at 2.17 eV, while the second gap is at 2.62 eV, which is 0.45 eV wider. The direct bandgap (2.17 eV) and the optical gap (2.62 eV) are the terms used to describe these two bandgaps [75].
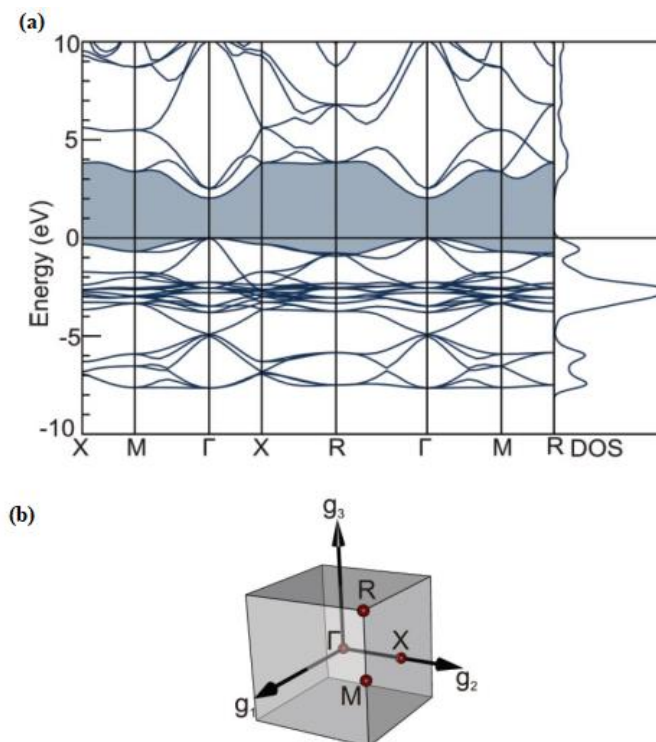
Figure 2.4: (a) The Cu_2O band structure and state density from DFT calculations. (b) Brillouin zones of cubic Cu_2O [84].
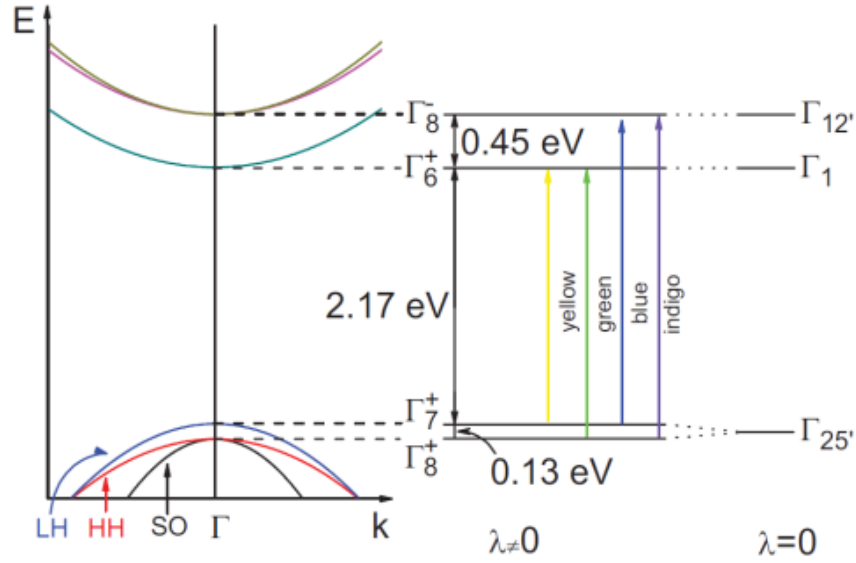
Figure 2.5: Cu_2O energy band diagram around the Γ –point [75].

2.3.6. Origin of p-type conductivity
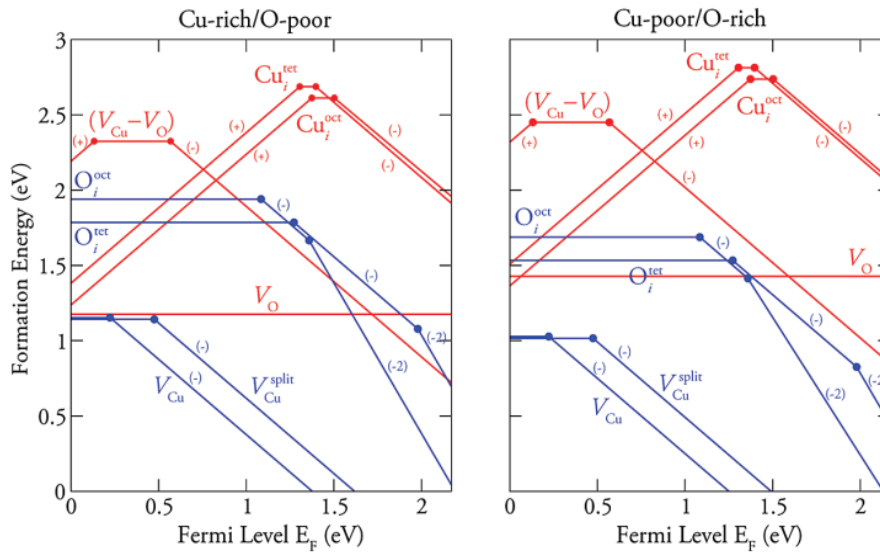
Figure 2.6: Formation energies as a function of Fermi level position for native point defects in Cu_2O [82].

The computed formation energies (solid lines) and transition (i.e. ionization) energies of intrinsic point defects in Cu_2O under both Cu-rich/O-poor and Cu-poor/O-rich circumstances are shown in Figure 2.6, demonstrating that Cu_2O meets all of the aforementioned

requirements. Copper vacancies (V_{Cu}) and oxygen interstitials (O_i) are the two probable native acceptors in Cu_2O. Because O_i (in tetrahedral and octahedral configurations) have deep acceptor levels (i.e. very high ε (0/–) and ε (–/2–) transition levels with respect to the V_{BM}), they cannot form holes. ε (q/q') denotes the transition level at which the charge state of defects changes (i.e. q→ q'); for example, ε (0/–) denotes the transition level at which the charge state changes from charge-neutral to (-1) charge state. V_{Cu}, on the other hand, has the lowest formation energy with a shallow acceptor level (i.e. tiny ε (0/–) ionization energy of EV + 0.28 eV) under both Cu-rich and Cu-poor circumstances [85]. This suggests that V_{Cu} is the primary source of Cu_2O holes and that it meets conditions (a) and (b).

Oxygen vacancies (V_O) and copper interstitials (Cu_i) are two potential native donors in Cu_2O. Despite V_O having low formation energy, it does not have a charge transition level inside the bandgap, as seen in Figure 2.6. As a result, they can only exist in the charge-neutral state and so cannot compensate for the holes generated by V_{Cu}. Furthermore, despite Cu_i having a positive charge state, it has far greater formation energy than V_{Cu}, making them incapable of efficiently compensating holes [85]. As a result, the p-type conductivity attributed to V_{Cu} dominates in Cu_2O, and the p-type conductivity of Cu_2O is fundamentally stable under all growth circumstances.

2.3.7. Optical properties

Thin films of Cu_2O have many optical properties that distinguish them from other materials and make them the focus of researchers' attention, where band structure, band gap energy, and optically active defects are among the physical characteristics of thin films that may be determined using optical characterization. These data were used to calculate the band gap and the kind of electrical transitions. An electron is moved from the valence band to the conduction band after a semiconductor absorbs a photon with energy greater than its energy band gap. As a result, the material's absorbance to the wavelength corresponding to the band gap energy abruptly rises [86].

Numerous theoretical calculations and experimental studies have already been conducted on the band gap and optical properties of Cu_2O, where Cu_2O has a direct forbidden gap of about 2.17 eV and a direct optically permitted band gap of 2.38- 2.62 eV (low-temperature values), which are well known from experiments [58, 87], Cu_2O's optical gap changes depending on the elaboration and shaping. Cu_2O's optical gap is near 2 eV in the bulk state [76], but higher values have been seen on films [64]. A quantum confinement effect connected to a decrease

in particle size is used in the literature to explain this increase in the gap [88] since it has a wide band gap of 2.137 eV, light with a wavelength longer than 580 nm (in the yellow region) can travel through it in a thin layer. However, it should be noted that in thin layers, the prohibited band may differ from this value, which applies to solid and pure oxide. Additionally, for thin films, the optical gap rather than the prohibited band is frequently taken into account. Green radiation is partially transmitted whereas blue radiation is either completely absorbed or partially transmitted when the wavelength of the light is below 580 nm. Thin layers of Cu_2O, therefore, seem clear yellow to the unaided eye. This is related to the fact that the band gap in thin films can vary depending on the deposition conditions [89]. All this partial transparency to visible light, together with its semiconducting properties, makes cuprous oxide a good candidate as a transparent p-type conductive oxide.

2.4. Methods of fabrication of Cuprous Oxide

Cuprous oxide (Cu_2O) has sparked a flurry of research on how to grow it using a wide range of techniques, from chemical to physical, under vacuum or at atmospheric pressure, where the popular methods for obtaining it include thermal oxidation, chemical vapor deposition (CVD), sputtering, sol-gel, and electrodeposition (ECD). And due to the many sedimentation techniques, we have sufficed with only three techniques, which are as follows:

2.4.1. Thermal oxidation

Thermal oxidation has been widely utilized to manufacture several high-quality metal oxides due to its simplicity and low cost [90]. Where clean wafers are sited in the wafer load station and introduced dry nitrogen (N_2) is into the chamber, while the furnace achieves the appropriate temperature (a horizontal or vertical tube furnace), where the nitrogen prevents oxidation. When the chamber reaches the desired temperature, the nitrogen gas flow is shut off and oxygen (O_2) is introduced, where the source of the oxygen might be a gas or water vapor. Depending on the process used (Wet or dry thermal oxidation), Heat is used in both processes to speed up the reaction rate. Dry oxygen is pumped into a heated process chamber in dry oxidation, whereas oxygen-saturated water vapor or steam is utilized in wet oxidation. [91]. Then nitrogen is reintroduced into the chamber once the oxidation is complete and the oxide layer has reached the desired thickness to prevent further oxidation. The wafers are then taken out of the chamber and checked before being ready for further processing [91]. Cu_2O sheets had previously been produced via thermal oxidation of copper films in the air at

appropriate temperatures for a few minutes to a few hours, according to earlier studies. Atmospheric oxygen diffuses into copper sheets during the thermal oxidation process, and the possibility of the formation of a mixture of two major oxide products, such as CuO and Cu_2O cannot be ruled out during the annealing process. And it is entirely dependent on the amount of oxygen present during the annealing process, that Cu_2O is formed first, followed by CuO after a sufficiently long period of oxidation [62, 90].
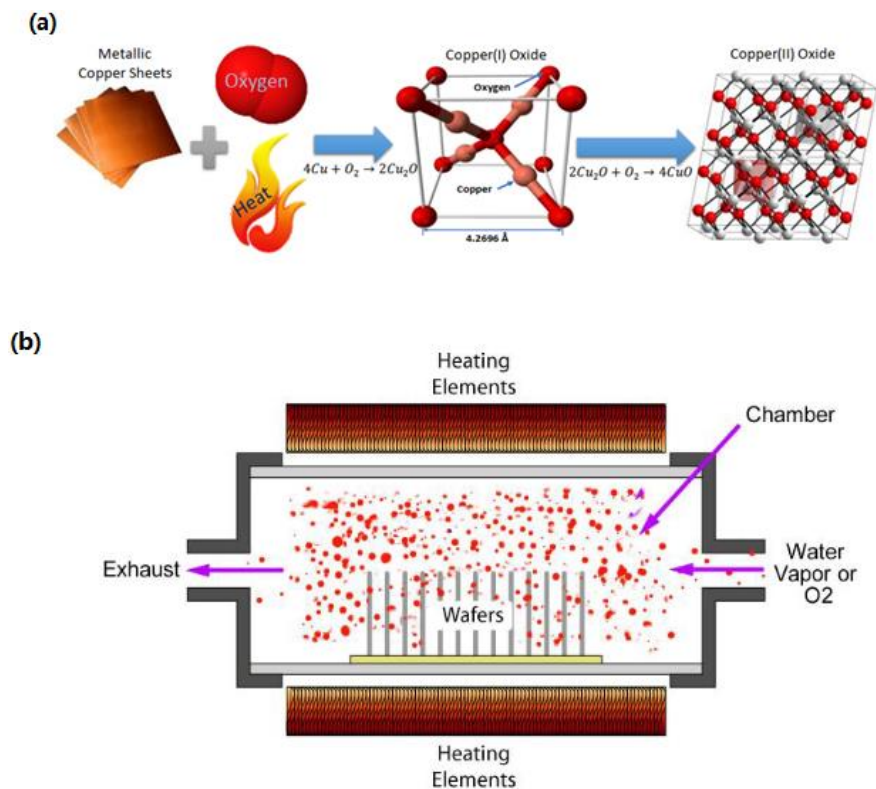
Figure 2.7: (a) Formation of Cu_2O and CuO. (b) Thermal Oxidation Furnace.

2.4.2. Electrodeposition

Electrodeposition has piqued the interest of researchers in recent years, it is the most promising technology for forming Cu_2O due to its ease of usage, low cost, low-temperature method (100 ºC), and simple control of film quality [92]. Electrodeposition can be done using a one- or two-electrode setup, with a reference electrode as the third electrode. A working electrode, which is a conduction substrate, a counter electrode, which might be a metal or carbon piece, a voltage source, and an electrolyte solution are all required for electrodeposition [93-95]. The reduction of Cu^{2+} ions to Cu^+ ions is the initial stage in this

deposition process. Because the ion is not stable, the second step is the precipitation of these Cu^+ ions to create Cu_2O. As illustrated in Equations (2.1 (a)) and (2.2 (b)) [96].

$$Cu^{2+} + e^- \leftrightarrow Cu^+ \qquad\qquad\qquad (2.1\ (a))$$

$$2Cu^+ + H_2O \leftrightarrow Cu_2O + 2H^+ \qquad\qquad\qquad (2.2\ (b))$$

$$2Cu^{2+} + H_2O + 2e^- \leftrightarrow Cu_2O + 2H^+ \qquad\qquad\qquad (2.3\ (c))$$
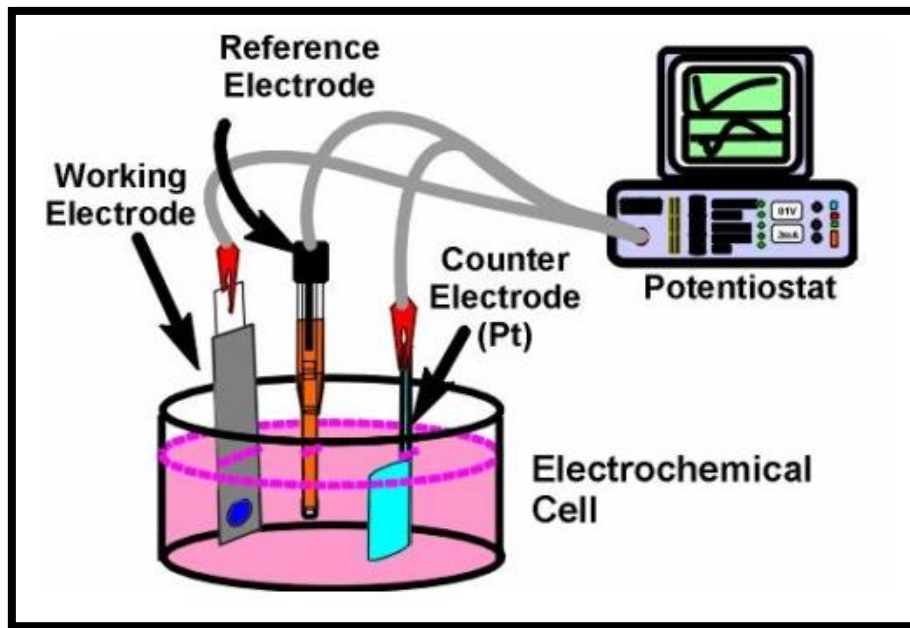
Figure 2.8: The schematic of Electrodeposition system [97].

2.4.3. Magnetron sputtering

Magnetron sputtering is an ionized gas, preferably inert (argon gas), accelerated by an electric field towards the cathode where the target materials are located in a sputtering deposition. During the procedure, High-energy ions erode the surface of the target within the plasma, and the liberated atoms travel through the vacuum environment and deposit onto the substrate to create a thin layer [98, 99]. The schematic representation of the magnetron sputtering set-up is shown in Figure 2.9.
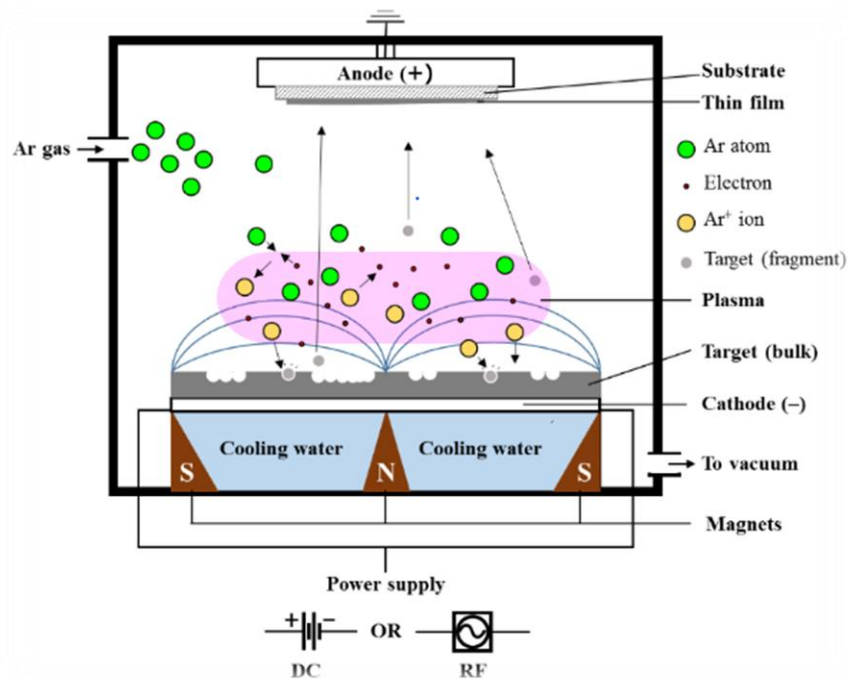
Figure 2.9: Schematic of a magnetron sputtering system and the deposition process [100].

2.5.   Cu₂O based- Solar Cells

The problem that photovoltaics mainly address is that the component elements of commercial photovoltaic technologies have some concerns and drawbacks as amorphous silicon is easily degradable, cadmium is highly toxic, tellurium and indium are not present in sufficient quantities in the lithosphere element, all these make difficulty large scale production of these materials economical. On the other hand, direct bandgap and it in the visible near-infrared range, earth-abundant, non-toxic materials, easily repeatable deposition process, appropriate for large-scale production; good PV conversion efficiency; long-term stability are the general characteristics of the perfect SC material [101]. This explains the great demand that cuprous oxide has received in this field because according to this perspective, a very promising Cu_2O solar cell device. Another one of the motivations for the study of Cu_2O as a material of the solar cell is that it has a theoretical power conversion efficiency limit of around 20 % according to (the Shockley-Queisser efficiency limit) [102]. Although the earlier discovery of Cu_2O received little attention at that time, except that Cu_2O was revived as a prospective material for low-cost solar cell manufacture in the 1970s as a viable energy solution following the oil crisis [103]. And so the research on it continues to this day.

2.5.1. Homojunction Cu$_2$O solar cells

the main factor limiting the maximum efficiency of Cu$_2$O cells was attributed to the lack of n-type Cu$_2$O since an approach to achieving n-type doping has not yet been fully developed therefore lack of deposition techniques for the production of high-performance n-type Cu$_2$O solar cells [104, 105]. Whereas due to the lack of interface strain in homojunction Cu$_2$O, it was widely assumed that the only option to obtain high-efficiency Cu$_2$O-based solar cells was to fabricate homojunction Cu$_2$O. But this issue led to it has not been possible to make an efficient homojunction of the type n-Cu$_2$O/p-Cu$_2$O, although there are some reports on n-type Cu$_2$O fabricated [96, 106, 107]. For example, Siripala et al. demonstrated the development of n-type Cu$_2$O films employing the electrodeposition method in 1986 [108]. Also, Han and Tao fabricated Cu$_2$O homojunction solar cells using a two-step electrochemical deposition process and achieved an efficiency of 0.1 % [78], and there too, McShane et al. used electrochemical deposition of the p-Cu$_2$O/n-CuO layer to produce Cu$_2$O homojunction solar cells with a 0.29 % efficiency [109, 110]. And A Cu$_2$O p-i-n homojunction solar cell with an Mn-doped i-type electrodeposited Cu$_2$O film and a Na-doped thermally oxidized Cu$_2$O film has achieved the best efficiency of 4.21 % thus far [111]. The open-circuit voltage of the Cu$_2$O p-n homojunction in the previously reported studies, however, was substantially lower than the theoretically predicted value, which is determined based on the bandgap of Cu$_2$O [102]. Therefore, these studies indicate that the performance of Cu$_2$O p-n homojunction solar cell devices needs to be further improved. The structural scheme and the energy band diagram of the Cu$_2$O homojunction solar cell in Figures 2.10 and Figure 2.11, respectively.
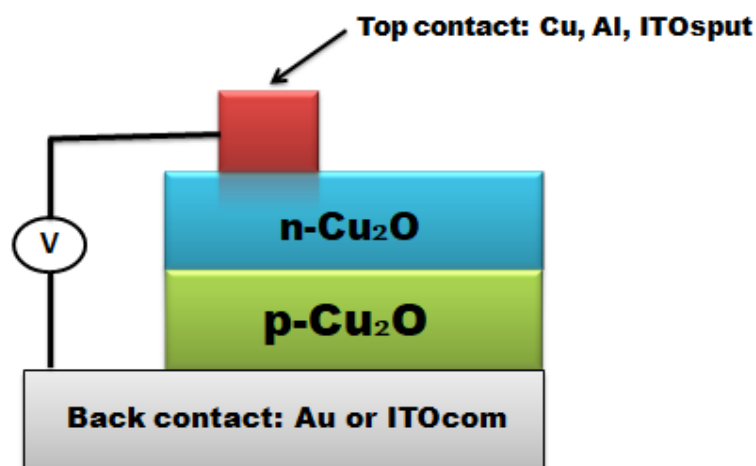
Figure 2.10: p-n Cu$_2$O homojunction solar cell [109].
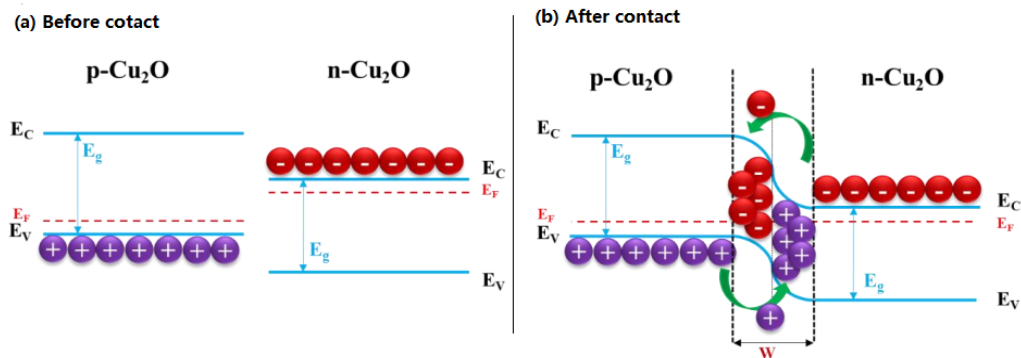
Figure 2.11: Energy diagram (a) before and (b) after contact of p-Cu$_2$O and n-Cu$_2$O.

2.5.2. Heterojunction Cu$_2$O solar cells

Due to a lack of knowledge and development of n-type Cu$_2$O, homojunction Cu$_2$O solar cells are less advanced than heterojunction Cu$_2$O solar cells. This limitation can be solved by forming a heterojunction with a different n-type semiconductor with a band structure compatible with Cu$_2$O. And this is what happened, where many studies have also focused on Cu$_2$O-based heterojunction solar cells. For example; Minami et al. [112] and Mittiga et al. [113], in 2004 and 2006 they made the TCO/Cu$_2$O heterojunction where used two different methods to prepare TCO thin films (pulsed laser deposition (PLD) and ion beam sputtering, respectively) on a Cu$_2$O sheet prepared by oxidizing copper at a high temperature. These cells produced had a conversion efficiency of 1.21 % and 2 %, respectively.

The n-ZnO/p-Cu$_2$O heterojunctions were produced by Izaki in 2007 by low-temperature electrodeposition of ZnO and Cu$_2$O layers in aqueous solutions, with a conversion efficiency of 1.28 % under AM 1.5 illumination [114].

Minami et al. [115] produced an AZO/ ZnO/ Cu$_2$O junction in 2011 using pulsing laser deposition (PLD) of the AZO and ZnO on oxidized copper sheets. This cell has a 3.83% efficiency and a 0.69 V open circuit voltage. In 2013, Nishi et al. [116] and Minami et al. [117] made the same structure of this solar cell with the same methods of deposition. The conversion efficiency this time was much higher, where reached was 4.12 % and 4.13 %, respectively.

More recently, in 2013, Minami et al. [117] made a similar compound in which PLD was used to deposit first a Ga_2O_3 buffer layer and then the n-type AZO layer on a thermally oxidized copper sheet. The conversion efficiency was much higher this time, 5.38 %.

A Cu_2O heterojunction solar cell with $\eta= 3.97$ % and with V_{OC} a of 1.20 V was reported by Lee et al. in 2014 [118]. This device has an electrochemically deposited Cu_2O layer, above it; we deposit a Ga_2O_3 buffer layer 10 nm thick by atomic layer deposition (ALD).

Atmospheric atomic layer deposition of $Zn_{0.79}Mg_{0.21}O$ over thermally oxidized cuprous oxide was used to manufacture $Zn_{0.79}Mg_{0.21}O/$ Cu_2O heterojunctions in the open air at low temperatures by Levskaya et al [119]. These heterojunctions gave solar cells a power conversion efficiency of over 2.2 % and an open-circuit voltage of 0.65 V.

So far, Minami et al [19]. Have reported the best possible Cu_2O heterojunction in 2016, this time again PLD was used to deposit a ZGeO buffer layer on the thermally oxidized copper plate, and then an n-type AZO layer. The realized conversion efficiency is 8 %.

Zang et al [120]. In 2018, used a rapid quenching and post-annealing treatment of radical oxidized Cu_2O to produce precisely oriented and micrometer-sized Cu_2O crystals for ZnO/Cu_2O solar cells. Their experimental results showed that the energy conversion efficiency (PCE) is 3.18 %.

In 2019, Miyata et al [121]. Used sputtering apparatus with their newly invented multi-chamber system to prepare n-type oxide semiconductor thin films for improving the photovoltaic characteristics of Cu_2O-based heterojunction solar cells, where they also achieved the greatest efficiency (3.21 %) in an AZO/ p-Cu_2O heterojunction solar cell. This value achieves the same or better properties than AZO / Cu_2O solar cells of similar structure, manufactured using the pulsed laser deposition process.

In 2020, Miyata et al [122] improved the photovoltaic properties of Cu_2O-based heterojunction solar cells that adopt a binary oxide n-type layer composed of non-doped ZnO thin films. This layer is prepared based on low-damage radio frequency (r.f.) power superimposed direct current (d.c.) magnetron sputtering deposition (MSD) and a multi-chamber system, where the efficiency of this cell was 3.22 %.

In 2021, Soichiro shibasaki et al [123] developed a transparent Cu_2O solar cell with power conversion efficiency (PCE) of 8.4 %, the highest in the world for this type of cell.

All these details of developments in Cu_2O heterojunction solar cells are summarized in Table 2.3.

Table 2.3: Some Cu_2O-based heterojunction solar cell efficiency latest developments (to 2020).

Type of junction	PCE (%)	Deposition method	Year
TCO/ Cu_2O	1.21	Pulsed laser deposition (PLD)	2004
TCO/ Cu_2O	2	Ion beam sputtering	2006
n-ZnO/p-Cu_2O	1.28	low-temperature electrodeposition	2007
AZO/ ZnO/ Cu_2O	3.83	pulsing laser deposition (PLD) on Cu_2O sheet	2011
AZO/ ZnO/ Cu_2O	4.13	pulsing laser deposition (PLD) on Cu_2O sheet	2013
AZO/ Ga_2O_3/ Cu_2O	5.38	pulsing laser deposition (PLD) on Cu_2O sheet	2013
Ga_2O_3/ Cu_2O	3.97	atomic layer deposition (ALD)	2014
$Zn_{0.79}Mg_{0.21}O$/ Cu_2O	2.2	Atmospheric atomic layer deposition	2014
ZGeO/ Cu_2O	8	Pulsed laser deposition (PLD) on Cu_2O sheet	2016
ZnO/ Cu_2O	3.18	rapid quenching and post annealing treatment of radical oxidized	2018
AZO / Cu_2O	3.21	pulsed laser deposition (PLD)	2019
AZO / Cu_2O	3.22	magnetron sputtering deposition (MSD)	2020

Figure 2.12 shows a summary of some significant attempts and achieved conversion efficiencies in the past fifteen years. Cu_2O-based heterojunction solar cells which show progressive and increasing efficiency during the last decade, where the recent industrial development of this technology by Minami groups and etc. portends significant growth in the near future.
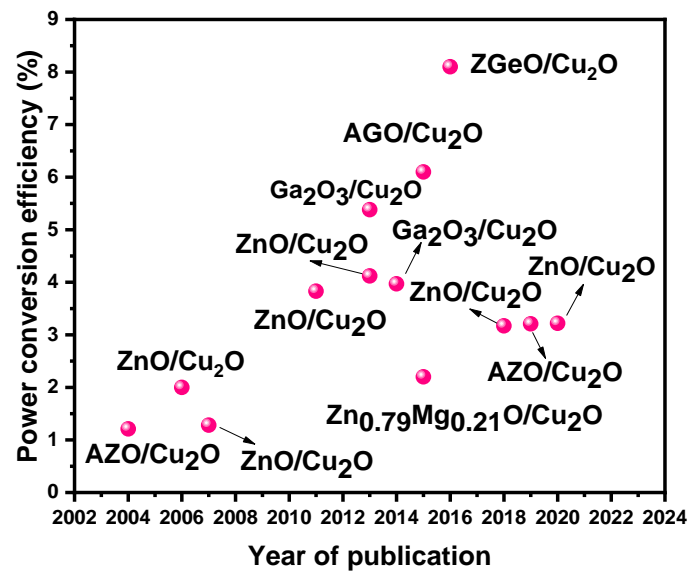
Figure 2.12: Power conversion efficiency in Cu_2O-based solar cells by year of publication.

2.5.2.1. Some buffers layers used in the Cu_2O HJSC

As we mentioned above the production of n-type semiconductor/p-type Cu_2O heterojunction solar cells reported in a large number of scientific papers used. Consequently, there are a number of n-type material candidates for building heterojunctions with cuprous oxide, including ZnO, ZMO, AGO, and ZGeO. And we will only talk briefly about these three oxides.

2.5.2.1.1. Zinc oxide (ZnO)

ZnO is an II-VI semiconductor with an ionicity that falls in between covalent and ionic. It crystallizes in three structures: wurtzite, zinc blended, and the rarely observed rocksalt. In comparison to other possible crystal structures, the wurtzite structure is the most stable and consequently the most frequent under ambient circumstances [124]. With lattice parameters a = 3.25 and c = 5.21, ZnO crystallizes in the wurtzite hexagonal crystal structure (space group P63mc) (see schematic in Figure 2.13). This structure is the result of the superposition of two hexagonal-close-packed (hcp) Zn and O sublattices, where the zinc atoms and oxygen atoms are connected tetrahedral coordination and vice versa [125]. It is an n-type transparent conductive oxide (TCO) having a large exciton binding energy of 60 meV, a wide bandgap of 3.37 eV, high electron mobility, high thermal conductivity, and strong piezoelectric responses

[126]. This made it among the candidate materials to be the buffer layer in Cu_2O-based heterojunction solar cells.
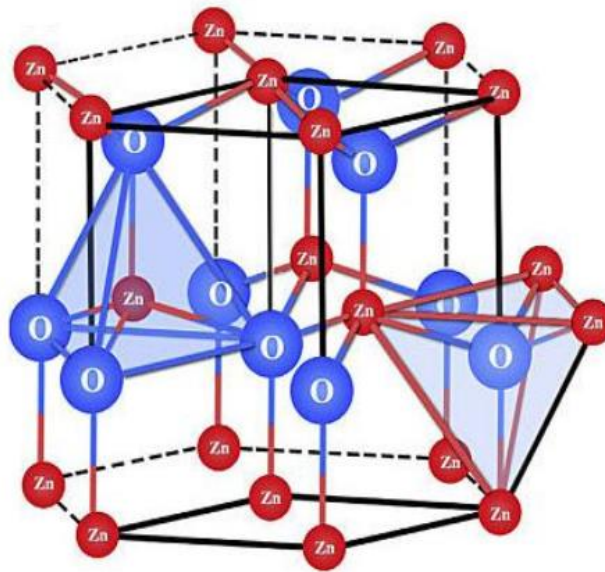
Figure 2.13: Schematic representation of ZnO wurtzite structure [127].

2.5.2.1.2. Zinc– Magnesium –Oxide thin film ($Zn_{1-x}Mg_x O$) ZMO

In order to improve the properties of a ZnO material the addition of the element Mg to zinc oxide, enables controllable changes to the material's work function, band gap energy, and lattice parameters [128]. This by substituting other bivalent metals, like Cd and Mg, for Zn, is one of its most intriguing properties. Mg substitution inside the ZnO lattice would result in an increase in the band gap dependent on the Mg content, whereas MgO is the prototype of an ionic compound semiconductor with a large band gap of 7.8 eV [129]. As shown in Figure 2.14.
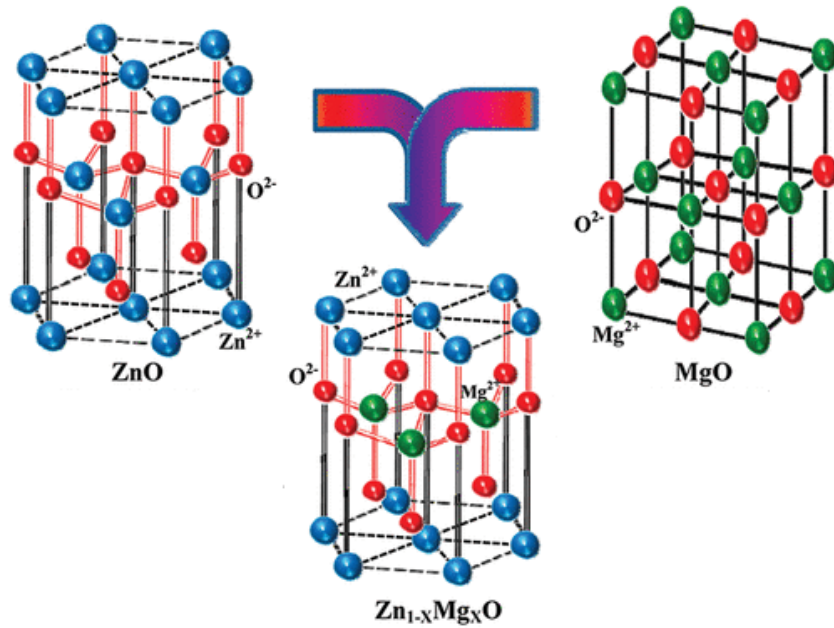
Figure 2.14: Schematic representation of $Zn_{1-x}Mg_xO$ structure [130]**.**

2.5.2.1.3. Aluminum–Gallium–Oxide thin film (Al$_x$ –Ga$_{1-x}$ –O) AGO

Among the five polymorphs (phases) possible of Ga_2O_3 [131], β -Ga_2O_3 has gotten a lot of interest and has gotten a lot of research because of its high physical, chemical, and thermal stability [4], where there are 2 kinds of coordination of metal ions in β-Ga_2O_3, i.e. tetrahedral and octahedral, where the location of both tetrahedral coordination of Ga (1) and octahedral coordination of Ga (2) ions in the unit cell Figure 2.15 (a) [132].

Alloying is a common way of modifying semiconductor features such as lattice constants, bandgaps, and valence- or conduction-band offsets (which are important to control or confine carriers in heterostructures) [133]. And This is the reason for adding In and Al to β-Ga_2O_3, resulting in β-(In, Ga)$_2O_3$ and β-(Al, Ga)$_2O_3$ alloys. Considering that the Al_2O_3 is an excellent candidate, with a bandgap of 8.82 eV in the corundum (sapphire) phase [134], with lattice constants of a = 4.76 Å and c = 12.99 Å, as shown in Figure 2.15 (b). And therefore, the bandgap of (Al$_x$Ga$_{1-x}$)$_2O_3$ alloy can be controlled by changing the Al composition from 0 to 1 [135], which has a tunable bandgap ranging from ∼4.8 eV (β-Ga_2O_3) to 8.7 eV (α-Al_2O_3) [136, 137]. This allows for the implementation of a variety of semiconductor heterostructure designs [136]. Thus these features of (AlGa)$_2O_3$ (Figure 2.16), made it a promising candidate for forming a pn heterojunction with cuprous oxide.
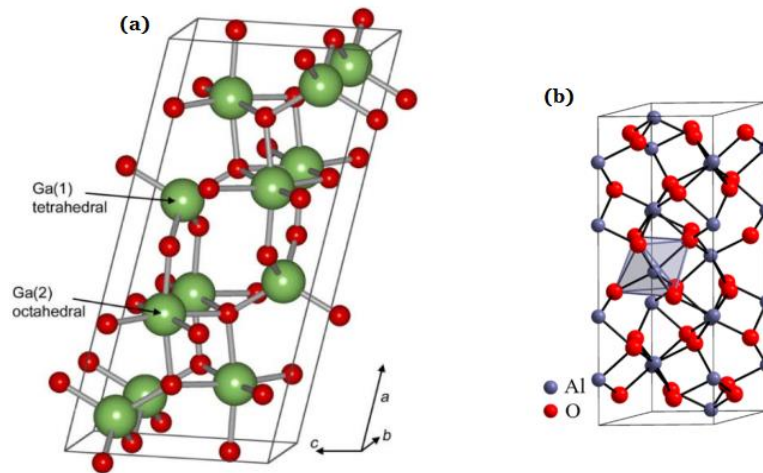
Figure 2.15: Schematic illustrations of (a) the monoclinic (β) phase structure of Gallium oxid [132] (b) Corundum structure of Al_2O_3 [138].
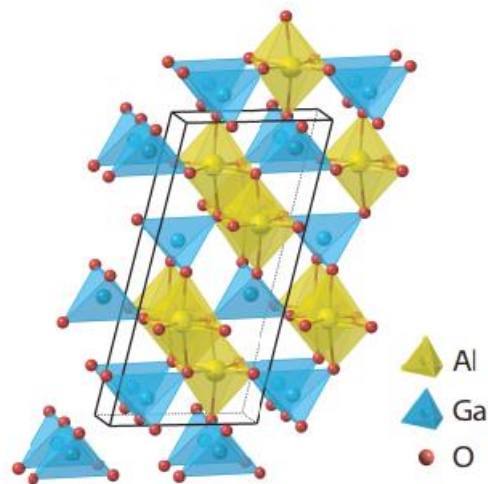
Figure 2.16: Schematic illustrations of $Al_xG_{1-x}O$ structure [139].

2.5.2.1.4. Zinc-Germanium-Oxide thin film ($Zn_{1-x}Ge_xO$) ZGeO

$Zn_{1-x}Ge_xO$ is an alloy of two binary compounds ZnO and GeO_2. Indeed, experimental evidence on the ternary complex Zn_2GeO_4 is limited, with just a few studies focusing on different Zn/Ge ratios. The composition of the material also plays a key role in achieving good performance. Currently, the best cell yields are obtained for Germanium On the optoelectronic level, these ratios influence more or less directly a certain number of the optical properties of $Zn_{1-x}Ge_xO$, in particular the bandgap E_g, and electron affinity χ. They showed that a direct energy gap of the material (homogeneous in composition) is empirically

linked to its Ge ratio, where x is the Ge ratio, typically, the ZGeO gap varies between 3.34 eV for pure ZnO and 6.00 eV for pure GeO_2.

2.5.2.2. **Methods of fabrication of n-type semiconductor Oxide (Buffer layer)**

We also know that the photovoltaic parameters of heterojunction solar cells are affected by the methods and conditions of deposition of absorber layers (active layers). the same with the buffer layer, where it was also found that the obtained photovoltaic properties in the Cu_2O-based heterojunction solar cells are considerably affected by the preparation conditions of the n-type buffer layers used [117]. Among the most common methods of deposition of buffer layers in Cu_2O heterojunction solar cells, such as sputtering, anodic oxidation, electrochemical deposition…etc, we will mention only two methods, as follows:

2.5.2.2.1. Pulsed laser deposition (PLD)

For the production of metal oxide and complex metal oxide, the PLD technique is a versatile, promising, simplest, and frequently used method, where the target material is vaporized in an ultrahigh vacuum or in the presence of gases such as oxygen using a powerful pulsed laser [140, 141]. The deposition is carried out in the presence of chemically reactive gas, where the gas molecules interact with the ablated material and deposit on the substrate in a reactive pulsed deposition [140]. The schematic representation of a pulsed laser deposition technique is shown in Figure 2.17.
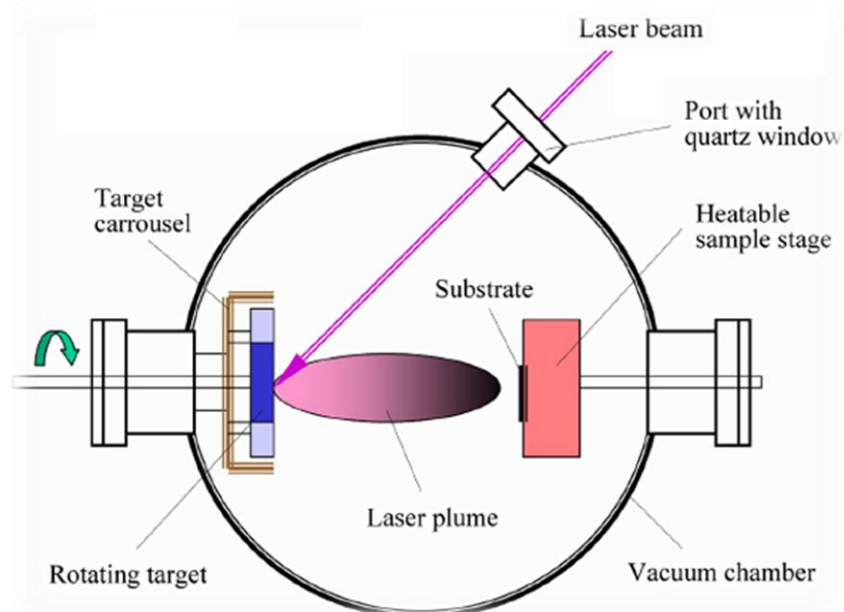
Figure 2.17: Schematic diagram of the PLD system [140].

2.5.2.2.2. Atomic Layer Deposition

Atomic layer deposition (ALD) is a CVD-based technique for growing thin films with high precision and it is considered the most advanced version of the traditional CVD process [142-144]. ALD (atomic layer deposition) is a chemical vapor deposition method depended on self-limiting gas–solid reactions mechanism [145]. ALD, on the other hand, is a cyclic process in which film growth is achieved by the repeating of cycles, each of which contains multiple steps, which it is providing for good surface coverage with extremely precise control of deposited thickness [143]. Figure 2.18 shows how a thin film is formed in units of atomic layers on a wafer.
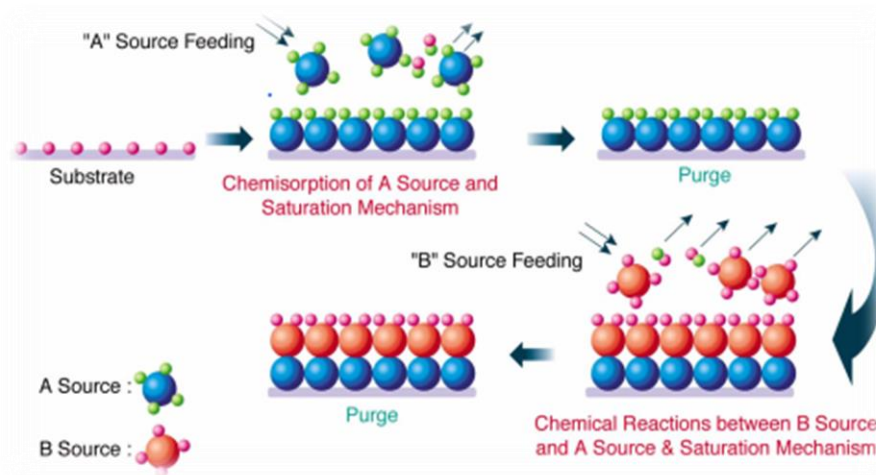
Figure 2.18: Shows the ALD Process deposition technique [146].

2.5.2.3. Some features of the buffer layers to improve the properties of the solar cell

The introduction of a buffer layer (BL) is recommended when heterojunctions are fabricated, since it allows the networks between different crystal structures to be coupled and, consequently, minimizes the density of interfacial states that occur in the contact plane between both materials. The BL must satisfy some conditions:

- **Thickness:** From the point of view of electrical transport, the BL must be minimally thick, a few nanometers, to allow tunneling current, which is one of the transport mechanisms present in heterostructures. In addition, the use of the buffer layer favors the reduction of interfacial recombination [118]. It is necessary that the BL does not have thicknesses comparable to those of the adjacent layers, because it could

contribute to the series electrical resistance of the heterostructure since, generally, the buffer layers used in this type of structure exhibit high resistivity [147, 148].

- **Lattice parameter:** The selection of BL lattice parameter should be chosen to facilitate the coupling between the two semiconductor oxides, that is, to allow a less abrupt transition between both crystalline structures that form the interface.

- **Bandgap width:** The BL will form part of the window layer of the heterostructure; therefore, its Eg is required to be wide, allowing the passage of most of the solar radiation toward the active layer.

2.5.2.4. Challenges associated with the poor performance of Cu$_2$O HJSC

When considering the Schockley–Queisser limit (SQL) and other important factors such as materials abundance, low-cost fabrication, suitable band alignment, and the possibility of having semitransparent devices, Cu$_2$O solar cells emerge as one of the most promising technologies with significant potential. However, the maximum experimental efficiency of 8 % remains to be far from its predicted theoretical efficiency. The origin of this weak efficiency is still unclear, and several relevant issues are thought to be possible sources, we mention the following:

2.5.2.4.1. Interface Problems at the heterojunction

Interfacial defects, which arise from the lattice mismatch between the individual materials as well as roughness and a step structure formed at the grain boundary (i.e., the surface) of the absorber layer sheets by chemical etching associated with differences in the crystal plane (crystalline direction) of the growth, are one of the largest drains on the effectivity of Cu$_2$O-based cells that have been identified. All of this lowers the PN-built-in junction's potential and creates the recombination current that is created at the heterojunction's interface. As a result of which its photovoltaic characteristics are reduced [19, 149]. Also, according to many studies and due to the use of separate deposition techniques, the Cu$_2$O layer has always undergone oxidation before the deposition of the buffer layer, and an undesirable CuO layer was formed at the junction, which is harmful to device performance. CuO will create new interfacial defect states, which will enhance recombination [150].

2.5.2.4.2. Conduction band offset between Cu$_2$O and an n-type layer

For optimum minority carrier transportation, any possible spike-type in the conduction band at the heterojunction should be reduced. Cu$_2$O's electron affinity is as low as 3.2 eV, making it

challenging to find an n-type partner with a similar electron affinity. As illustrated in Figure. 2.22, Brandt et al surveyed band offset between Cu_2O and a wide range of n-type materials, which provides useful information [151]. For example; the conduction band offset between Cu_2O and ZnO is as high as 1.2 eV, which could be the reason for its low open-circuit voltage. In contrast, a low offset of 0.04 eV was observed between Cu_2O and ZGeO, which can explain its high performance to date.
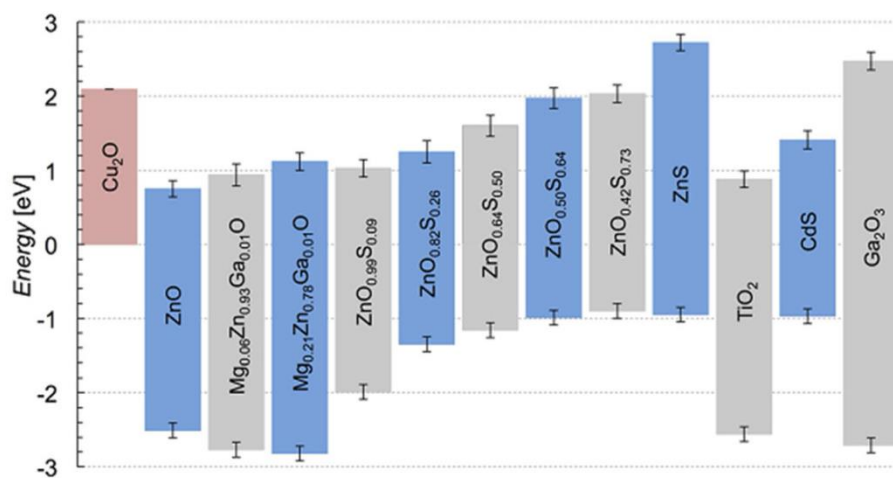
Figure 2.19: Band energies of n-type materials with respect to Cu_2O. All energies are referenced to the valence band of Cu_2O [151].

Chapter 3

SILVACO-ATLAS simulation process

Chapter 3: SILVACO-ATLAS simulation process

3.1. Introduction

The device physics can be investigated using a numerical device simulator, which helps you to "observe and visualize" through cross-sections within a device. Simulation offers a taste of the virtual fabrication laboratory environment, in which we can perform methodical and thorough optimization of device design parameters, with the benefit that a parameter can be varied according to the necessity without costing a penny, and the results can be obtained in a very short time rather than waiting a long time in the actual fabrication laboratory. Furthermore, as numerical simulations are backed up by accurate physical and/or theoretical models, the outcomes can be extremely useful and substantive. A numerical device simulator, in particular, is important for researching novel technologies and understanding device mechanics, such as solar cells, since it helps users to change several device parameters in a limited amount of time. This leads to the continuing research and development of products like this.

3.2. Simulation Tools

The most widely used free-of-charge software for solar cells is PC-1D [152], SCAPS-1D [153], wxAMPS [154], and AFORS-HET [155]. These -mentioned four softwares are useful; however, they all address individual solar cell viewpoints, without providing complete coverage of the complex combination of phenomena that actually take place.

PC1D is computer software for IBM-compatible personal computers that solve the fully coupled nonlinear equations for the quasi-one-dimensional transport of electrons and holes in crystalline semiconductor devices, with a focus on photovoltaic devices [152]. It is designed for Si PVs and is popular because of its easy methods and quick calculations.

SCAPS-1D is a one-dimensional solar cell simulation program developed at the Department of Electronics and Information Systems (ELIS) of the University of Gent, Belgium. This original program is developed for cell structures of the CIS and the CdTe family, considering ion injection conditions that are not uniformly distributed [156]. Kim et al. succeeded in simulating of CIGS/c-Si tandem solar cells using SCAPS-1D [157].

The wxAMPS program is a 1D solar cell modeling program developed at the University of Illinois at Urbana-Champaign in collaboration with Nankai University in China [158]. It follows the physical principles of AMPS, adding the contribution of tunneling current, improving convergence and velocity, and improving visualization [159].

Chapter 3: SILVACO-ATLAS simulation process

AFORS-HET is a numerical simulation tool for modeling heterojunction and homojunction devices [160]. It should also be capable of simulating perovskite/c-Si tandem solar cells [161].

2D and 3D software's such as SILVACO TCAD, etc were also developed for better and more accurate modeling of devices and are very useful for more realistic simulation prior to device design and manufacturing. Unlike the four solar cell simulation models mentioned above, which are based on a combination of discrete electrical components, this novel model enables direct manipulation of materials, dimensions, and doping and may be used to extract the electrical properties of a solar cell based on the virtual manufacturing of its physical structure [162]. Silvaco is an American company corporation based in Santa Clara, California. It is a leading provider of technical simulation software chains, with applications for modeling analogue and computer circuits in all fields of electronics. Since being established by Dr. Ivan Pesic in 1984 [163], SILVACO has developed into the most significant semiconductor device simulator. The company's software includes everything from basic modeling to complex integrated circuit schematics and mining tools.

3.3. SILVACO overview

SILVACO TCAD is referred the acronym for Silicon Valley Corporation Technology Computer Aided Design. It is a package for simulating the semiconductor process that combines numerous physically based simulators (such as ATHENA, ATLAS, MERCURY, SSUPREM3, etc.) into a single environment called DECKBUILD. And due to the large number of these tools, we will mention only the ones that were used in this work, where some of the significant tools included in this software are ATLAS, DECKBUILD, TONYPLOT, etc. Where in this work, the devices were built using DECKBUILD, and the simulations were run in ATLAS. The outputs were viewed using TONYPLOT. A brief on the tools employed are given next.

- **DECKBUILD:** is an interactive runtime and input file development environment within which all TCAD modules can run. Also, it has an extensive library with hundreds of pre-run examples decks that cover a wide range of technologies and materials and enable users to quickly recognize simulations [43].
- **ATLAS:** is a physics-based device simulator. It provides general capabilities for 2D and 3D simulations of semiconductor devices through it defines the physical structure to be simulated, the physical models to be employed, and the bias settings for which the

electrical characteristics of the device are to be reproduced. And predicts the electrical behavior of specified semiconductor structures [164].

- **TONYPLOT:** is a visualization tool that provides comprehensive interactive scientific visualization capabilities. It is used to plot data obtained from device simulations. The usual methods for showing scientific data are all supported. These comprise polar plots, surface and contour plots, Smith charts, and x-y plots with linear and logarithmic axes. Also, user-defined equations with the variables can be plotted, whether the electrical data (such as drain current) or physical parameters (e.g., electric field) [165].

3.4. Principle of the SILVACO-ATLAS simulator

The electrical properties of devices are predicted using ATLAS, a physically-based device simulator, based on physical structures and bias conditions. This device simulator is based on the simultaneous resolution of the Poisson equation and the continuity equations for the electrons and the holes i.e. these equations provide the general framework for device simulation, where the nodes of a grid that is superimposed over the device are subjected to a set of differential equations based on Maxwell's laws and the semiconductor transport equations [166] in order to achieve this, where the electrostatic potential and the concentration of electrons and holes are calculated at all times and at all points in space in a sequence of finite elements.

- **Poisson equation**

    The equation of Poisson gives the relation between the electrostatic potential and the space charge density, as shown by the following equation [50].

$$div(\varepsilon \nabla \psi) = -\rho \tag{3.1}$$

    Where ψ is the electrostatic potential; ε is the dielectric permittivity, and ρ is the space charge density.

    Where, the space charge density is given by:

$$\rho = q(p - n + N_D^+ - N_A^-) \tag{3.2}$$

Where, q is the elementary electric charge; N_D^+ and N_A^- are the concentrations of ionized impurity donors and acceptors respectively; n and p are the electron and hole densities respectively.

- **Continuity equation for electrons and holes**

The continuity equation describes the variation of both electron and hole carriers' densities as a function of time. It is can be written as [167, 168]:

$$\begin{cases} \dfrac{\partial n}{\partial t} = \dfrac{1}{q} div\overrightarrow{J_n} + G_n - R_n \\ \dfrac{\partial p}{\partial t} = -\dfrac{1}{q} div\overrightarrow{J_p} + G_p - R_p \end{cases} \tag{3.2}$$

Where:

$\overrightarrow{J_n}$ and $\overrightarrow{J_p}$ the electron and hole current densities,

G_n and G_p : are the generation rates for electrons and holes,

R_n and R_p are the recombination rates for electrons and holes;

- **Carrier transport equations**

Drift and diffusion are the two fundamental transport modes in a semiconductor. Drift, the movement of charge due to electric fields (the first term of equations below), and diffusion, the flow of charge due to density gradients (the second term of equations below) [168].

$$\begin{cases} \overrightarrow{J_n} = qn\mu_n\vec{E} + qD_n\dfrac{dn}{dx} \\ \overrightarrow{J_p} = qp\mu_p\vec{E} - qD_p\dfrac{dp}{dx} \\ \vec{E} = -\overrightarrow{grad\psi} \end{cases} \tag{3.3}$$

Where:

μ_n and μ_p: the mobility of electrons and holes;

D_n and D_p are the electron and hole diffusion coefficients, which are given through Einstein's relationship [169]:

$$D_n = \frac{K_B T}{q}\mu_n \qquad\qquad ; D_p = \frac{K_B T}{q}\mu_p$$

3.5.   ATLAS Inputs and Outputs
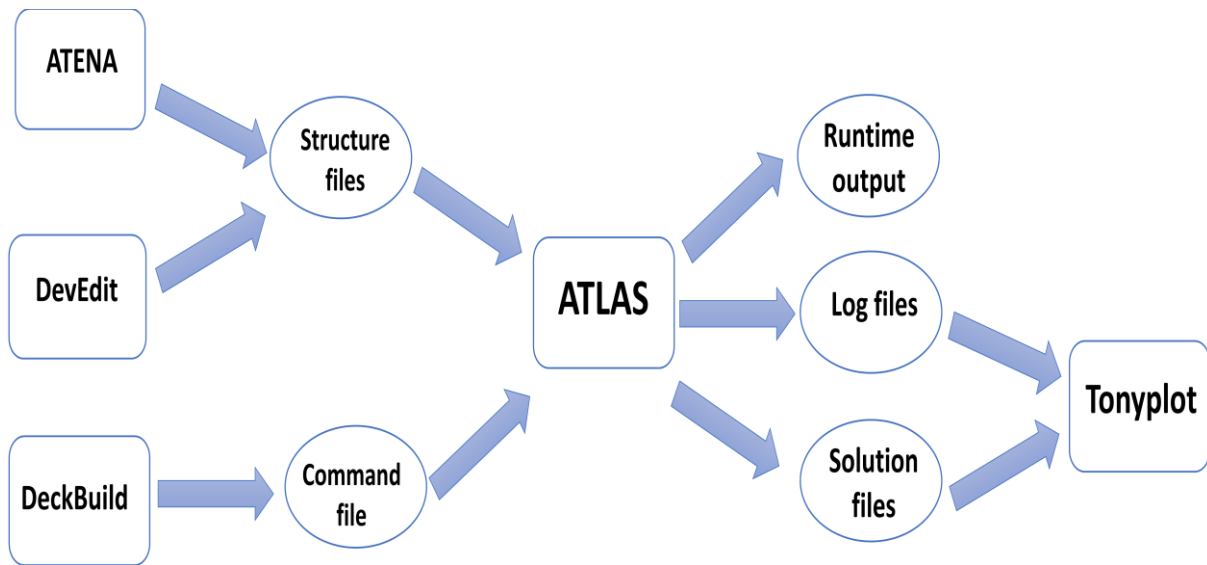
Figure 3.1: Atlas inputs and outputs.

From Figure 3.1, we note the types of information which circulate in the entry and exit of ATLAS. Most of the simulations performed by ATLAS use two input files. The first file is a script file containing the commands for ATLAS to run (represented by the Command file). The second file is a structure file that defines the structure that will be simulated. At the out of ATLAS, we have three types of files. The first of these files is the "Runtime" output which gives the progress, errors and warning messages during the simulation. The second type of file is the "log" file which stores all the voltage and current values from the analysis of the simulated device (this is the electrical behavior file). The third output file is the Solution file, this file stores 2D or 3D data concerning the values of the solution variables in the device at a given point (this is the physical file; it contains the structure in a particular state). The last two files are processed by the TONYPLOT viewing tool [170].

3.6.   The order of Atlas commands

Silvaco-Atlas receives the input files through DeckBuild. The code is written in the input file calls Atlas to work with the following command:

"Go Atlas"

51

Chapter 3: SILVACO-ATLAS simulation process

Following this command, the order of the commands in the input file is significant. The respect of this chain is essential to allow ATLAS to take into account all the specified models correctly. There are five groups of commands shown in the Figure below (Figure 3.2).

(a) Structure Specification

- Structure MESH specification,
- Structure REGION specification
- ELECTRODE placement
- DOPING profile specification

(b) Model Specification

- Defining MATERIAL type for each region (SiO2 or Al, etc.)
- Invoke appropriate physical MODELS
- Setting boundary conditions
- and CONTACT information
INTERFACE specification

(c) Numerical Method Selection

- Invoke suitable numerical solvers such as Gummel, Newton, or Bulk METHOD for different operating conditions with appropriate parameters such as number of iteration, error limit, etc.

(d) Solution Specification

- LOG file declaration to contain I-V characteristics
- Solution of device using SOLVE with intervals for bias voltage (or drive current) specification
- Specifying data types to be solved (e.g., recombination parameter, bad energy, etc.).

(e) Result Analysis

- Parameter extraction via EXTRACT command,
- Analyzing device structure with different bias condition using graphical post-processing tool TONYPLOT

Figure 3.2: The order of command groups to be specified in ATLAS from (a) to (e) [171].

The buildup consists of a well-defined mesh on which cells are built, where the density of the mesh's many triangles determines the simulation's resolution, which also specifies how accurately cells are represented and how long program iterations must take. Then, various materials are allocated to each of the regions of this triangular mesh that have been partitioned. The electrodes are then assigned in order to get the electrical properties needed for the device or for any desired region. Next, every defined material must be linked to doping, and material attributes must be disclosed to the greatest extent feasible for the most

accurate simulation. The user's next step is to select a model from a variety of options, determine which is best for assessing the structure and achieve a better outline for specific cell simulation.

After specifying a structure file in ATLAS, the rest of the configuration (except for outcome analysis) consists of supplying command-line instructions to ATLAS in order for it to complete a simulation run. The order in which these orders are given is critical, and it can be broken down into five classes of statements (see Figure 3.2). It's also necessary to pay attention to the order of statements within each category, such as structural specification, model specification, and solution methods. Failure to obey these orders can result in the premature termination of a simulation run or the appearance of an error message.

3.6.1. Structure Specification

A system structure can be defined in three different ways in ATLAS [172]:

- Can be enable structure by using a file to read an internal structure.
- Through DeckBuild's automated interface feature, the input structure may be transferred from ATHENA or DevEdit.
- The ATLAS command language may be used to construct a structure.

3.6.1.1.   Mesh

To use of Atlas command language to describe the structure device, you must first create a mesh. It consists of horizontal and vertical lines with a user-determined space between them. Where it establishes a set of triangles that define the physical boundaries of the cell within which the simulation runs. Whereas, a node is created at each corner of the triangles; for each node, the equations to be solved are computed [173]. The upper limit of the number of nodes used is 100000—the maximum number of nodes permitted by ATLAS (in 2D) [174].

The simulation's accuracy is determined by whether the mesh is coarse or fine. The simulation is faster with a coarse mesh, but the results are less precise. The simulation is slower with a fine mesh, but the measurements are more precise. As a result, the regions with a finer mesh are the most important in the simulation. The most effective approach to operate is to use a fine grid only in crucial areas (around junctions and depletion regions, areas of a high electric field, areas of the current flow, areas of significant recombination effects, areas of high impact ionization...etc.) and a coarser grid anywhere else [173]. The Mesh can be defined as follows:

MESH SPACE.MULT=<VALUE>

X.MESH LOCATION=<VALUE> SPACING=<VALUE>

Y.MESH LOCATION=<VALUE> SPACING=<VALUE>

3.6.1.2.   Region

After the mesh has been defined, it is necessary to define the regions. The mesh is partitioned into discrete, numbered regions, each of which corresponds to a specific material. This considering that the atlas has a maximum regions definition of 15000 [174]. The boundaries of each region are identified explicitly in the x and y axes (y.min, y.max, x.min, and x.max) in microns. This is done by this statement as follows:

REGION number=<integer> <material_type> /<position parameters>

3.6.1.3.   Electrodes

In this step, electrodes are identified of the device. This is done using the ELECTRODE statement as follows:

ELECTRODE NAME=<electrode name><position_parameters>.

The positions parameters specify are define using y.min, y.max, x.min, and x.max parameters in micron. Instead, you can define the position of electrodes by using the BOTTOM or TOP statement. Further, can be enabled another details about their materials and work functions.

3.6.1.4.   Doping

The doping statement is the structure specification's final necessary input. Inside the previously allocated areas, where the doping statement is used to assign the doping level. Various properties can be added to the doping statement to determine how the semiconductor was doped and whether the region is n- or p-type, as well as whether the doping was uniform or gaussian. The format to define this statement is as follows:

DOPING <distribution_type> <dopant_type> <position_parameters>.

For position parameters, can be define by y.min, y.max, x.min, and x.max parameters or by region number.

All these steps in building the structure specification are shown in Table 3.1.

Chapter 3: SILVACO-ATLAS simulation process

Table *3*.1: Basic steps to design a ZnO/ Cu$_2$O heterojunction solar cell structure specification with the simulator ATLAS.

structure specification	Plot
Mesh: x.m l=0 s=0.5 x.m l=10 s=0.5 y.m l=0 s=0.05 y.m l=0.2 s=0.005 y.m l=0.2+$zno s=0.0002 y.m l=$thick/2 s=$thick/40 y.m l=$thick-1 s=$thick/200 y.m l=$thick+0.2+$zno s=0.2 y.m l=$thick+1.2+$zno s=0.2	
Region: *region num=2 y.min=0.2* *y.max=0.2+$zno material=ZnO* *name=ZnO* *region num=3 y.min=0.2+$zno* *y.max=$thick+0.2+$zno* *name=Cu2O user.material=Cu2O*	
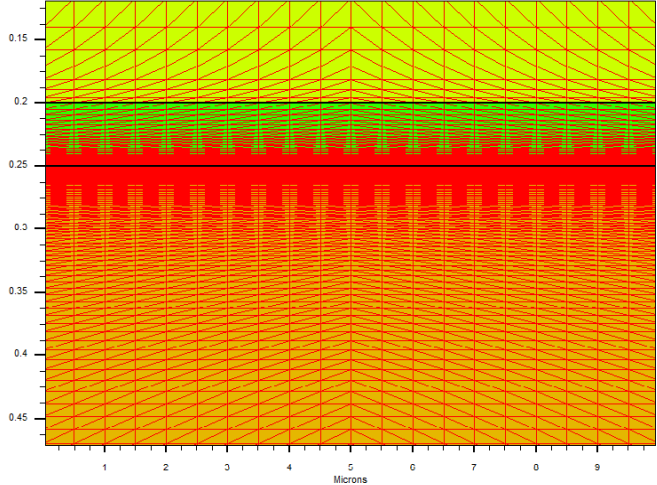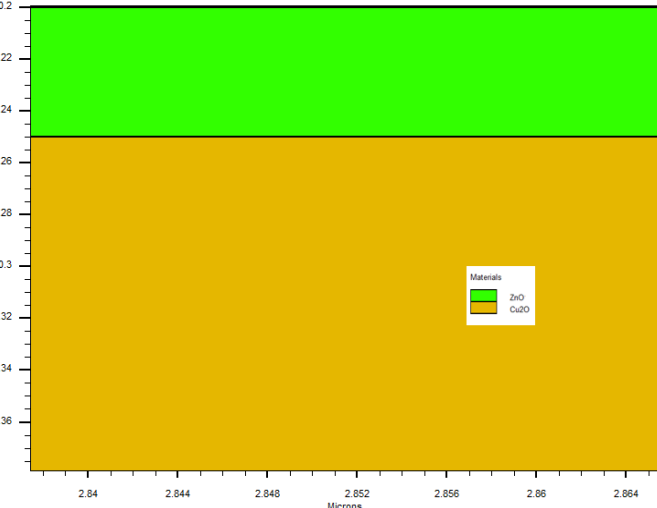
Electrodes: *elec num=1 name=cathode top* *elec num=2 name=anode* *y.min=$thick+0.2+$zno* *y.max=$thick+1.2+$zno* *mat=Gold*	
Doping: *#doping AZO* *doping region=1 uniform n.type* *conc=1e21* *#doping ZnO* *doping region=2 uniform n.type* *conc=1e19* *#doping Cu2O* *doping region=3 uniform p.type* *conc=1.25e14*	
Schematic diagram of the simulated structure.	
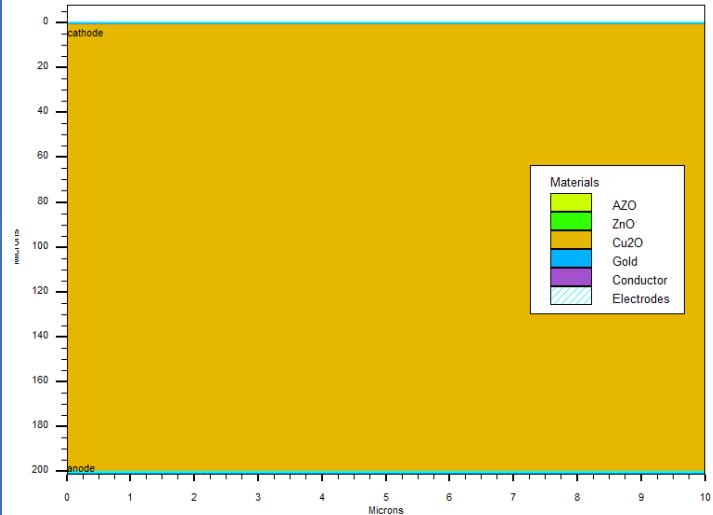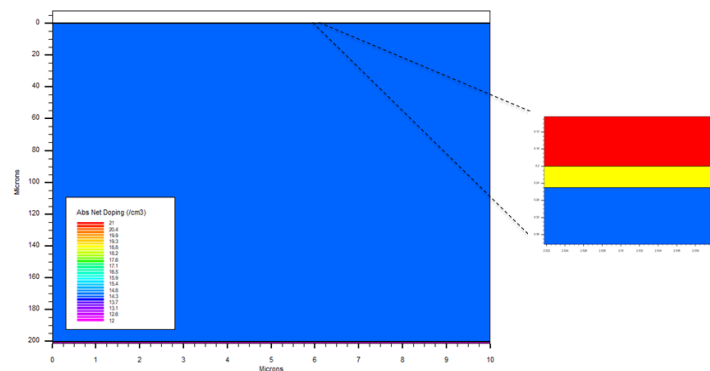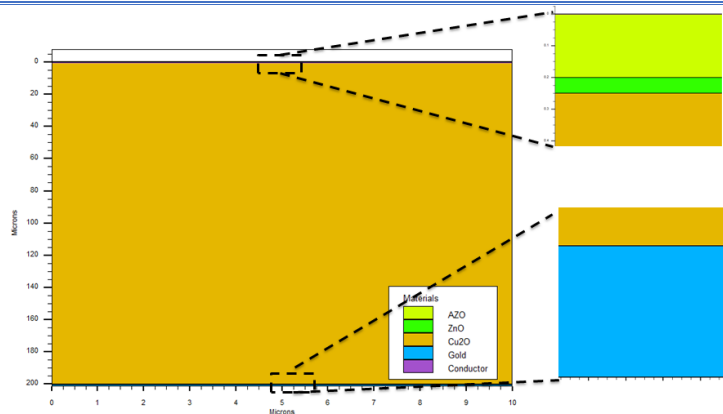
3.6.2. **Materials Model Specification**

After define the structure specification, the materials model specification is the next step.

3.6.2.1. **Materials**

After specifying structure of the device, the material statements describe each of the various materials used in the simulation. The format of the material statement is:

MATERIAL <localization> <material_definition>

Where this statement allows to specify values for basic parameters and properties of material used in the simulation, where there are several parameters that the user can identify for the material of a given region we cite for example lifetimes, mobility (electrons and holes), electron affinity, dielectric constant, bandgap, and an optical file containing the wavelength-dependent refractive index n and extinction coefficient k for a material [175], etc. Otherwise, Atlas will use its default settings which can be recognized in the software help.

For example:

Material material=ZnO EG300=3.3 mun=10 mup=5 affinity=4.4 permittivity=9 NC300=2.2e18 NV300=1.8e19

For new materials that are not recognized by Atlas, this is done by entering a file (nk file) that contains each of the wavelength, the refractive index, as well as the extinction coefficient for the new material to be defined, then replacing the MATERIAL parameter in the REGION statement with the USER.MATERIAL parameter in order to name of the new material. Also must be classified this material through user.group parameter [174]. As well as the known Atlas material is taken as a default material using the user.default parameter. It is as shown in this example:

Material material=Cu2O EG300=2.1 MUN=200 MUP=100 affinity=3.2 permittivity=7.6 NC300=2.43e19 NV300=1.34e19   me.tunnel=0.93 mh.tunnel=0.56   index.File= Cu2O.nk user. Group= semiconductor user. Default=zno

3.6.2.2.   The Models

Atlas includes a large number of physical models. We can pick which physical models Atlas will use throughout the device simulation once we establish the mesh, geometry, and doping profiles, and tweak the properties of electrodes, where mobility, recombination, carrier statistics, impact ionization, and tunneling are the five types of physical models [174]. The MODELS declaration specifies all models, with the exception of impact ionization where the IMPACT statement sets impact ionization. These physical models can be enacted for the entire device or for a material-by-material basis [175]. The model statement has the following syntax:

MODELS <model-name>

Chapter 3: SILVACO-ATLAS simulation process

These models are among those enabled in our simulation:

MODELS BGN CONMOB SRH TEMP=300 PRINT

"BGN: Bandgap narrowing model".

"CONMOB: is the concentration dependent model".

"SRH: Specifies Shockley-Read-Hall recombination using fixed lifetimes".

"PRINT: Prints the status of all models, a variety of coefficients, and constants which will be used during the simulation".

3.6.2.3.   Contact

The usual assumption for an electrode in contact with semiconductor material is that it is ohmic while it is considered a Schottky contact if a work function is defined. The CONTACT statement is used to indicate one or more electrodes' metal work functions. Also, the surface recombination parameters in the CONTACT statement can be enabled by the SURF.REC parameter. For example:

CONTACT NAME=ANODE WORKFUNCTION=5.1

CONTACT NAME=ANODE SURF.REC VSURFN=1e7 VSURFP=1e7

3.6.2.4.   Interface

The "interface" statement is used to the definition of the interface charge density interfaces between semiconductors and insulators also surface recombination velocity. And the statement is as follows [165]:

interface <localization>

3.6.2.5.   Light Beam

Where a device's illumination is critical (as in solar cells), it's possible to use a variety of light sources and change their location, orientation, and intensity. The light spectrum can be described in all of its detail [176].

For the purposes of this work, the cell was exposed to 1- sun illumination AM1.5G with a normal-incidence light source at 100 (mW/cm^2) powers. This can be simulated in the Silvaco database by using the definition of the BEAM statement with the AM1.5 parameter as follows:

Beam number=1 angle=$BeamAngle   y.origin=$BeamYorigin x.origin=$BeamXorigin xmin=$BeamXmin xmax=$BeamXmax AM1.5

The X. ORIGIN and Y. ORIGIN parameters specify the source position, the ANGLE=90 describes vertical illumination from the top of the cell, and the number of points used in the spectrum is defined by "wevel.num."

3.6.3. Numerical Method Selection

Following the specification of the material models, the numerical method form must be defined. A variety of numerical methods exist to calculate the solutions:

- The decoupled method of Gummel.
- The coupled method of Newton.
- The Block method.

The Gummel method solves for each unknown while leaving the other unknowns constant. This process is replicated until a stable solution is found. NEWTON's method solves all of the unknowns at the same time. The BLOCK method for solving uses the NEWTON method for some equations and the GUMMEL method for others [174].

For system equations that are weakly coupled and have only linear convergence, the GUMMEL method is utilized, whereas the NEWTON method is utilized for strongly coupled system equations with quadratic convergence. This leads ATLAS to spend more time when solving for quantities that are essentially constant or weakly coupled. When the NEWTON method is unable to deliver a reliable solution, the BLOCK method can provide faster simulations. The following example is the statement to determine the method [174]:

METHODE NEWTON

3.6.4. Solution Specification

The simulation is ready to take on to the next step (the solution) after the specification of the device structure, material properties, physical models, and the numerical method. This section of the input deck of ATLAS is where the simulation calculates to solve for the specified device. It is divided up into four parts: LOG, SOLVE, OUTPUT, and SAVE.

3.6.4.1.   The "LOG" statement

The "LOG" statement allows the creation of a data file where All results of a run are stored in this file; any DC, transient, or AC data generated by "SOLVE" statements after the "LOG" statement are also saved. Example of this Statement syntax:

LOG OUTFILE=Cuprous_SolarCell.LOG

3.6.4.2.   The "SOLVE" statement

For one or more bias points for either D.C. or A.C., the SOLVE statement determines the solution. To achieve a first estimate of the final solution, it is necessary to perform a simplified initial solution (which solves simply Poisson's equation). The syntax would be as follows:

SOLVE INIT

SOLVE VANODE=0   VSTEP=0.02   VFINAL=0.76   NAME=ANODE

3.6.4.3.   The "LOAD' and "SAVE" statement

In order to get more accurate initial guesses for bias points, the "Load" and "Save" statements are combined. The SAVE statement is used to store all information about the node points, and after that, the LOAD statement retrieves this information and helps solve it.

Save outf=Cuprous_SolarCell.str

3.6.5. Data Extraction and Plotting

The last section of the input deck consists of extracting the data and plotting it. The DeckBuild environment offers the EXTRACT statement, which directly prints out the required data from the file to the output deck. This command allows extracting device parameters, where electrical quantities such as current short circuit (Jsc), open-circuit voltage (Voc), efficiency (η), and others may be extracted from simulation results. The EXTRACT command is operated on the previously solved curve or structure file. EXTRACT By default, it uses the currently open log file, unless a different filename is specified before the extraction routine.

All the results of device simulations in Atlas are plotted by first storing the results in a file and then loading the file into Tonyplot.

Chapter 3: SILVACO-ATLAS simulation process

In the case of a structure file, the data is shown in the form of a 2D mesh plot (structure of device). And as for the case of a log file, Tonyplot will display the data in an x-y plot (the current density-voltage characteristics). (As see Figure 3.3).
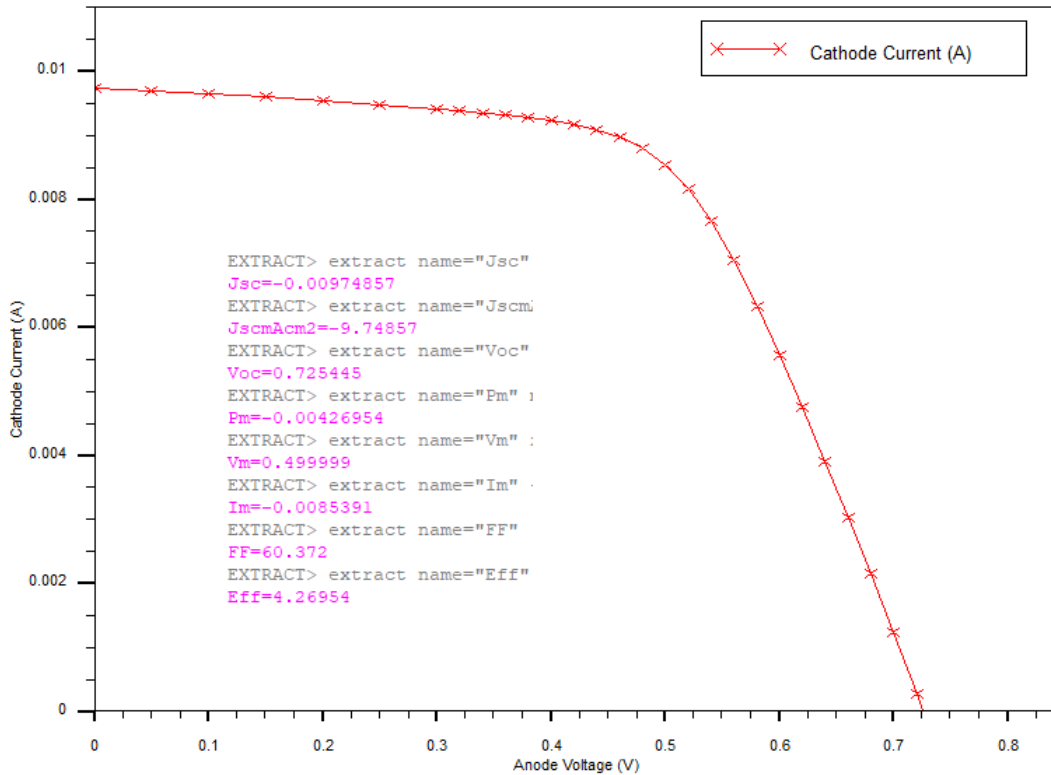
Figure 3.3: Curve I-V of the solar cell from Tonyplot.

Chapter 4

Results and discussion

Chapter 4: Results and discussion

4.1. Introduction

Given the growing need for low-cost solar cells, the abundant semiconductors on Earth are considered promising candidates [177, 178]. Among them, cuprous oxide has been very popular in this field. Cu_2O has long been thought to be difficult to make a p-n homojunction due to its natural p-type conductivity [82, 179, 180]. Instead, a heterojunction device design with an n-type transparent conducting oxide (TCO) comprising aluminum-doped zinc oxide has shown to be the most successful method of constructing Cu_2O-based solar cells (AZO) [117]. However, the PCEs of Cu_2O-based heterojunction devices have remained low, owing to a high density of defects at the heterojunction interface [117, 181, 182], leading to a greater interface recombination rate and a dramatically lower open-circuit voltage (Voc) [183].

Various buffer layers [19, 115, 117, 184] have been added between the Cu_2O and TCO layers to minimize the non-ideal heterojunction. The device's performance has been greatly improved because of the well-controlled electrical band alignment of the buffer layer and defect density at the interface. So far, among Cu_2O-based solar cells with a V_{OC} of 1.2 V, a Zinc-Germanium-Oxide (ZGeO) buffer layer produced by pulsed laser deposition has achieved the greatest PCE of 8 % [19].

In this chapter, the simulation of Cu_2O solar cells using SILVACO TCAD software is achieved. Our approach consists in modeling several heterojunction solar cells based on Cu_2O and in identifying the optimization variables, that is to say, the parameters of the solar cell resulting in the best performance. To do this, we adopted optimization, dependent on varying one of the physical parameters and observing its influence on the performance of the device. It, therefore, allows above all highlighting the influence of a given parameter that we want to optimize to maximize the performance of a device. In the case of the optimization of the efficiency of a solar cell, it would make it possible, for example, to know the influence of the physical and geometric parameters of the cell, thus making it possible to know the optimum value of the efficiency according to each parameter and its sensitivity in relation to these different parameters. The advantage of this type of optimization lies in the fact that the influence of each parameter on the efficiency of the cell is easily visualized and thus makes it possible to classify these parameters according to their degree of influence.

First, we will simulate the AZO/Cu_2O solar cell, and the validation with experimental results is made based on the comparison of J-V characteristics. Next, we will study the possibility of introducing four different types of buffer layers (ZnO, ZMO, AGO, and ZGeO) between AZO

and Cu_2O and compare the respective J-V characteristics with experimental results. Based on the experimental studies available, we have chosen to continue with the two solar cells; that with a ZnO buffer layer and with ZGeO. The optimization of the first solar cell $AZO/ZnO/Cu_2O$ is done by introducing HTL (hole transport layer) of different materials and studying the effect of contact work function. The optimization of $AZO/ZGeO/Cu_2O$ solar cell is based mainly on the band gap energy of the buffer layer and the affinity of both the buffer layer and front window.

4.2. **AZO/ Cu_2O solar cell structure**

The first Cu_2O-based solar cell structure proposed by Minami et al was n+/p, as shown in Figure 4.1. It is a very simpler design with an n-AZO thin film window layer of 0.2 μm thick, a p-Cu_2O as an absorber layer of 200 μm thick, and a gold layer of 1μm thick as back contact (anode). The simulation of this structure is performed using material parameter values described in Table 4.1.
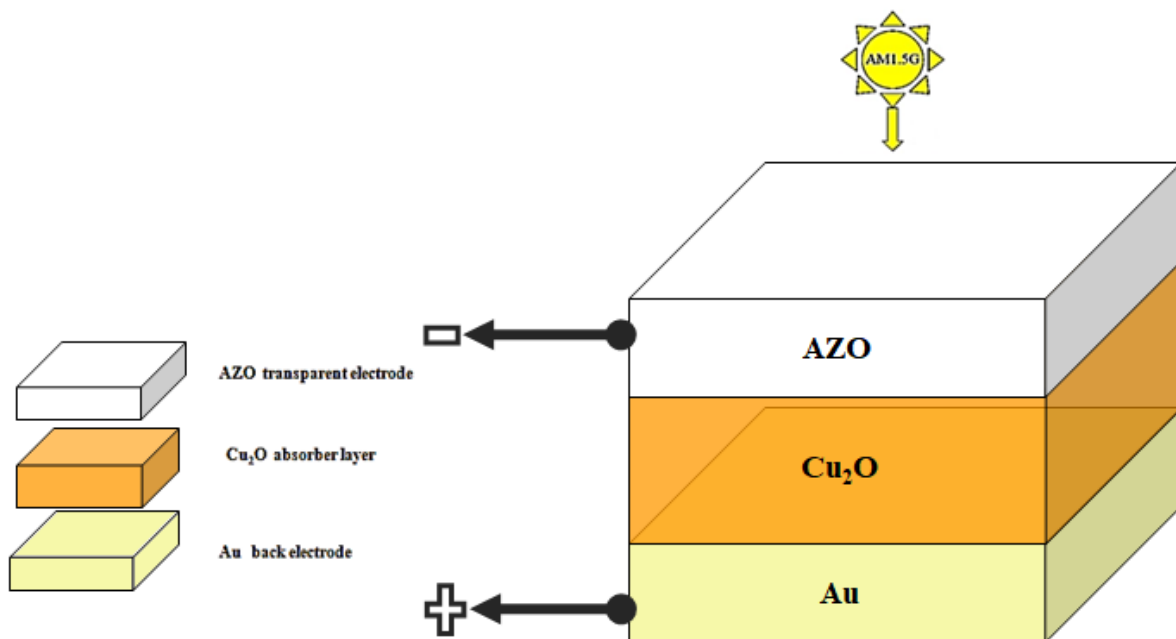
Figure 4.1: Schematic diagram of the n+-AZO/ p-Cu_2O heterojunction structures.

Chapter 4: Results and discussion

Table 5.1: Semiconductor material parameters of TCO (AZO) and the absorber layer (Cu₂O) [115, 117, 185-189].

Parameters	Description	TCO	Absorber
		AZO	Cu₂O
$W(\mu m)$	Thickness	0.2	200
ε_r	Dielectric constant	9	7.6
$E_g(eV)$	Bandgap	3.35	2.1
$\chi(eV)$	Electron affinity	4.4	3.2
$N_C(cm^{-3})$	Effective density of states of conduction band minimum	2.2×10^{18}	2.43×10^{19}
$N_V(cm^{-3})$	Effective density of states of the valence band maximum	1.8×10^{19}	1.34×10^{19}
$\mu_e(cm^2/V.s)$	Electron mobility	10	200
$\mu_h(cm^2/V.s)$	Hole mobility	5	100
$N_D(cm^{-3})$	Donor concentration	1×10^{21}	-
$N_A(cm^{-3})$	Acceptor concentration	-	$10^{13}\ to\ 10^{16}$
Defect type	-	D-like, Gaussian	D-like, Gaussian
$N_{DG}(cm^{-3})$	Gaussian state density for donor-like	1×10^{18}	1×10^{13}
$N_{AG}(cm^{-3})$	Gaussian state density for acceptor –like	-	-
$E_D/_{E_A}(eV)$	Gaussian peak energy level	midgap	midgap
$W_G(eV)$	Gaussian defect standard deviation	0.1	0.1
$\sigma_e(cm^2)$	*Capture cross-section of electrons*	1×10^{-12}	5×10^{-13}
$\sigma_h(cm^2)$	*Capture cross-section of holes*	1×10^{-15}	1×10^{-15}

Chapter 4: Results and discussion

The AZO/Cu₂O configuration was simulated at AM1.5G solar spectrum with an incident power density of 100 mW/cm² at room temperature (300 K).
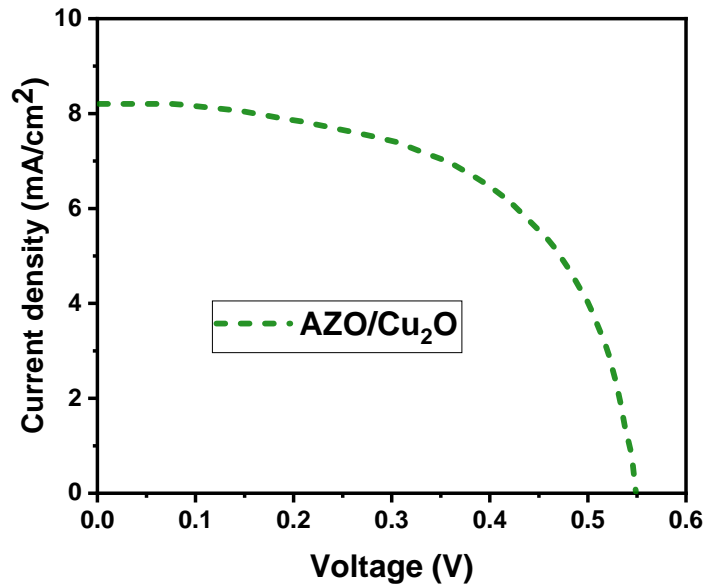
Figure 4.2: Simulated J–V characteristics of AZO/Cu₂O structure under AM1.5 illumination solar spectrum at 300 °K.

Table 4. 2: Simulated output parameters of AZO/Cu₂O cell.

Structure	Simulation				Experimental [117]			
	J_{SC} (mA/cm^2)	$V_{oc}(V)$	$FF(\%)$	$Eff(\%)$	J_{SC} (mA/cm^2)	$V_{oc}(V)$	$FF(\%)$	$Eff(\%)$
AZO/Cu₂O	8.221	0.55	57	2.578	8.19	0.55	57	2.53

The obtained current density-voltage characteristic (J-V) curve is shown in Figure 4.2, respectively. The cell exhibits low output parameters $J_{SC} = 8.221 \, mA/cm^2$, Voc= 0.55 V, FF= 57 %, and a power conversion efficiency (PCE) of ~2.578 %. These values are in agreement with the corresponding experimental values as shown in Table 4.2.

Chapter 4: Results and discussion

This device however seems to give poor PCE. Among the possible causes of the poor performance of this structure are the interfacial defects between the AZO layer and the cuprous oxide layer shown by the simplified diagram in Figure 4.2. These interfacial defects may be due to lattice mismatch, different grain boundary sizes, and impurity injection during the formation of AZO/Cu_2O transitions. It can be also due to incomplete bonds at the interface AZO/Cu_2O because this act as a trap for the charge carriers generated by the photons. Therefore, all these interfacial defect conditions cause high interfacial recombination and a shunting path for carriers that induce considerable losses in the solar cell performance.
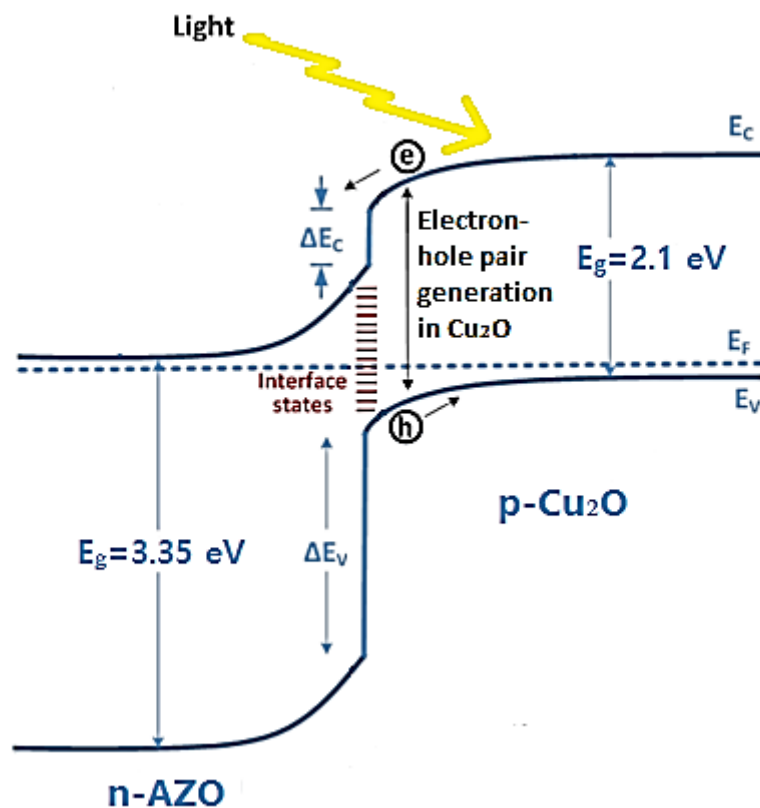
Figure 4.3: Energy band diagram of AZO/Cu_2O solar cell showing the possible interface defects.

The tunneling effect, in which electrons pass through from the conduction band of AZO to the valance band of Cu_2O, has also played a significant role in cell performance in addition to defects problems at the junction interface.

4.3. Effect of different buffer layers on Cu₂O-based solar cells

In a heterojunction, a buffer layer's function is to join with the absorber layer to form a junction and direct the most quantity of incoming light possible toward the absorber layer [190]. During the transport of the photo-generated carriers to the outside circuit, the buffer layer should have minimum absorption losses, low surface recombination, and minimal electrical resistance [191]. In addition, the band alignment, electrical qualities, and the creation of a large depletion zone with the p-type absorber layer are also important futures of the buffer layer. All of these can reduce carrier tunneling and keep open circuit voltage values higher to provide a higher contact potential [190].

In this section, we will study the effect of different buffer layer materials between the window layer (AZO) and the absorber layer (Cu₂O) .The suggested materials are ZnO, ZMO, AGO, and ZGeO. The input parameters of these buffer materials layers are illustrated in Table 4.3.

Table 4.3: The material parameters of the buffer layers [19, 115, 117, 184-189, 192-194].

Parameters	Description	Buffer			
		ZnO	Zn$_{0.91}$Mg$_{0.09}$O	(Al$_{0.025}$Ga$_{0.975}$)$_2$O$_3$	Zn$_{0.38}$Ge$_{0.62}$O
$W(\mu m)$	Thickness	0.05	0.05	0.06	0.06
ε_r	Dielectric constant	9	10	10	10
$E_g(eV)$	Bandgap	3.35	3.48	4.9	5
$\chi(eV)$	Electron affinity	4.4	4.37	4	3.24
$N_C(cm^{-3})$	Effective density of states of conduction band minimum	2.2×10^{18}	2.2×10^{18}	3.72×10^{18}	3.72×10^{18}
$N_V(cm^{-3})$	Effective density of states of the valence band maximum	1.8×10^{19}	1.8×10^{19}	3.72×10^{18}	3.72×10^{18}
$\mu_e(cm^2/V.s)$	Electron mobility	10	10	118	10
$\mu_h(cm^2/V.s)$	Hole mobility	5	5	50	5
$N_D(cm^{-3})$	Donor concentration	1×10^{19}	4×10^{19}	1.25×10^{18}	1×10^{20}
Defect type	-	D-like, Gaussian	D-like, Gaussian	D-like, Gaussian	D-like, Gaussian
$N_{DG}(cm^{-3})$	Gaussian state density for donor-like	5×10^{17}	5×10^{17}	5×10^{17}	1×10^{18}

E_D/E_A (eV)	Gaussian peak energy level	midgap	midgap	midgap	midgap
W_G (eV)	Gaussian defect standard deviation	0.1	0.1	0.05	0.05
σ_e (cm²)	Capture cross-section of electrons	1×10^{-12}	1×10^{-12}	1×10^{-12}	1×10^{-12}
σ_h (cm²)	Capture cross-section of holes	1×10^{-15}	1×10^{-15}	1×10^{-15}	1×10^{-15}

Numerous investigations have shown that the Cu_2O layer has always experienced oxidation prior to the deposition of the buffer layer, resulting in the formation of an undesirable CuO layer at the junction all because of the employment of separate deposition methods [150]. Numerous techniques have been used to lessen but not entirely get rid of these oxidized layers [150]. To reduce the CuO layer, for instance, reactive precursor vapors can be introduced prior to the commencement of the buffer layer deposition [150].

Although, the buffer layers are used to reduce interfacial recombination by enhancing band alignment across the heterojunction and lowering the density of interface defects. However, some interface defects still exist and are even required in simulation to reproduce electrical outputs that are close to experimental values. By simulating solar cells without enabling surface defects at the interface, we noted that the solar cells have a far greater V_{OC} than the baseline heterojunction solar cells (experimental devices), (data not shown here). In addition, the simulation of the Cu_2O layer as defect-free leads to an unreasonably efficient carrier transport over the contact.

Yuki Takiguchi and al. [185] developed a reliable model of simulation through the introduction of an interfacial layer (IL) and a defective Cu_2O layer with a defect density of $10^{19} cm^{-3}$. One potential cause of the surface defect layer was a non-stoichiometric Cu_2O oxide phase, which was unstable under most circumstances and was mentioned in various reports about the heterojunction interface [185]. In order to describe interface defect states, rnulf Nordseth and al [187] and Christyves Chevallier and al [189] created an interface defect layer between the buffer and Cu_2O layers.

Therefore, we have considered these interfacial defect states indicated in [150, 195] and summarized in Table 4.4 for the four heterojunction solar cell structures.

Table 4.4: Interface defects parameters used in our simulation [185-189].

HJSC structure	Interface defects			
	$N_{DG}(cm^{-3})$	$W_G(eV)$	$E_{DG}(eV)$	σ_n/σ_p
ZnO/Cu₂O	4×10^{15}	0.1	1.05	5×10^2
ZMO/Cu₂O	7×10^{15}	0.1	1.05	5×10^2
AGO/Cu₂O	1×10^{17}	0.1	1.05	5×10^2
ZGeO/Cu₂O	1×10^{17}	0.1	1.05	5×10^2

Results of the simulation of AZO/Cu₂O solar cells with different buffer layers are shown in Table 4.5 and Figure 4.4. The comparison is done with what was reported by Minami group [19, 115, 117, 184, 192, 193].

Table 4.5: The output parameters of the AZO/Cu₂O heterojunction solar cells with different buffer layers.

HJSC structure	Simulation				Experimental [19, 117, 184, 193]			
	J_{SC} (mA/cm^2)	$V_{OC}(V)$	$FF(\%)$	$Eff(\%)$	J_{SC} (mA/cm^2)	$V_{OC}(V)$	$FF(\%)$	$Eff(\%)$
AZO/ZnO/Cu₂O	9.74	0.72	60.37	4.26	9.69	0.71	60	4.13
AZO/ZMO/Cu₂O	9.756	0.728	61.071	4.342	9.38	0.73	63	4.31
MgF₂/ AZO/AGO/Cu₂O:Na	11.55	0.85	66.20	6.56	10.95	0.84	66	6.10

MgF₂/ AZO/ZGeO/Cu₂O:Na	10.88	1.08	73.92	8.72	10.80	1.20	63	8.23
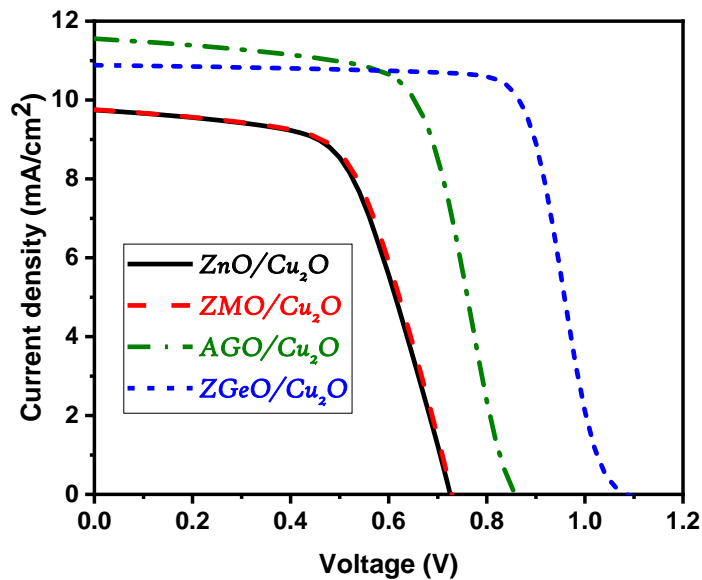
Figure 4.4: Calculated J–V characteristics of the four HJSC structures under AM1.5 illumination solar spectrum at 300 °K.

We found that the results of the simulation and the experiment were nearly in good agreement. However, the fourth structure (AZO/ZGeO/Cu₂O) has given higher FF and lower Voc than the experimental. This can be attributed to additional defects in the interface between the buffer layer and the absorber layer that we have not taken into account in our simulation. Minami and all [19] mentioned the possibility of surface defects in the interface. It was difficult for us to introduce these defects since we have no idea about their electronic features (positions in band gap capture cross section, density, etc…). We envisage studying the effect of such defects by using their electronic features as fitting parameters.

By returning to the obtained results, the primary heterojunction solar cell simulated with ZnO buffer layer exhibits solar output parameters of $J_{SC} = 9.78\ mA/cm^2$, $V_{OC} = 0.72\ V$, FF= 60.37 % and efficiency of 4.26 %. A significant improvement is noticed by replacing the ZnO buffer layer with Magnesium doped zinc oxide (ZMO) where the output parameters

were$J_{SC} = 9.75 \, mA/cm^2$, Voc= 0.727 V, FF= 61.07 %, and Eff= 4.34 %. Also, more significant improvement is achieved by using aluminum-doped gallium oxide (AGO) as a buffer layer and replacing the absorber Cu_2O layer with Cu_2O:Na (doped by sodium), and adding MgF_2 as a top anti-reflecting coating. Under these considerations, J_{SC}, V_{OC}, FF, and efficiency reached 11.55 mA/cm^2, 0.85 V, 66.20 %, and 6.56%. For the fourth structure, the same considerations as the third structure were taken, except for the buffer layer, which was of ZGeO. Further improvement is remarked for this structure and we noted that the solar cell with a ZGeO buffer layer had the best efficiency of 8.72 %. The other parameters are $J_{SC} = $ 10.88 mA/cm^2,$V_{OC} = 1.08 \, V$, and FF= 73.92 %. Here J_{SC} decreases a little bit to 10.88 mA/cm^2 compared to the third structure. For the measured values, the same remark holds except for FF which is equal to 63 %. The further improvement in the simulated Voc, FF, and hence the efficiency can be explained by the additional reduction in ΔEc and the significant extension of the Cu_2O layer type inversion. The small reduction in Jsc can be related to the increase of ΔEc at the interface AZO/ZGeO and the reduction of the potential barrier in front of holes in the Cu_2O region that have become a minority due to the type inversion at the interface. This favors additional interface recombination between opposite free carriers.

The reduction noticed in the experimental value of FF can be related to the significant increase of the measured Voc. It is known that $FF = \frac{P_m}{V_{oc}J_{sc}}$, then, apparently the significant increase in Voc over Pm (which reflects the efficiency of the cell) induced a reduction in FF. However, in the simulation, the proportional increase of Voc with the efficiency results in a FF this rather increases. A possible reason to explain the reduction of the measured FF can be the presence of additional resistive losses in the real structure.

 Among the most possible reasons that explain this increase in the efficiency of solar cells from 4.26 % (ZnO/ Cu_2O) to 8.72 % (ZGeO/ Cu_2O) is the conduction band offset (CBO) at the interface between the buffer layer and the absorber layer. This results from the band alignment at the buffer/ absorber contact.

CBO is the energy difference (ΔEc) between the absorber layer's CB level and the buffer layer's CB level. Conduction band offset (CBO) comes in two kinds: cliff-like and spike-like band alignment, as seen in Figure 4.5. An energy cliff will occur at the buffer/absorber interface and ΔEc will be negative when the CB level of the buffer layer is lower than that of the absorber. However, if the buffer layer's conduction band edge is higher, then it is formed an energy spike at the interface and ΔEc will be positive [196-198]. The band alignments

were likewise based on the electron affinity rule —or vacuum level alignment—. According to Anderson's rule, the valence and conduction band discontinuities at the hetero-interfaces are displayed as follows [197]:

$$\Delta E_C = \chi_{SC1} - \chi_{SC2} \tag{4.1}$$

$$\Delta E_V = I_{SC1} - I_{SC2} \tag{4.2}$$

$$\Delta E_V = \left(\chi_{SC1} + E_g^{SC1}\right) - \left(\chi_{SC2} + E_g^{SC2}\right) \tag{4.3}$$

With χ_{SC1}, I_{SC1} and χ_{SC2}, I_{SC2} are the electron affinity and ionization potential of sc1 and Sc2, respectively. The sum of electron affinity and bandgap indicates the ionization potential.
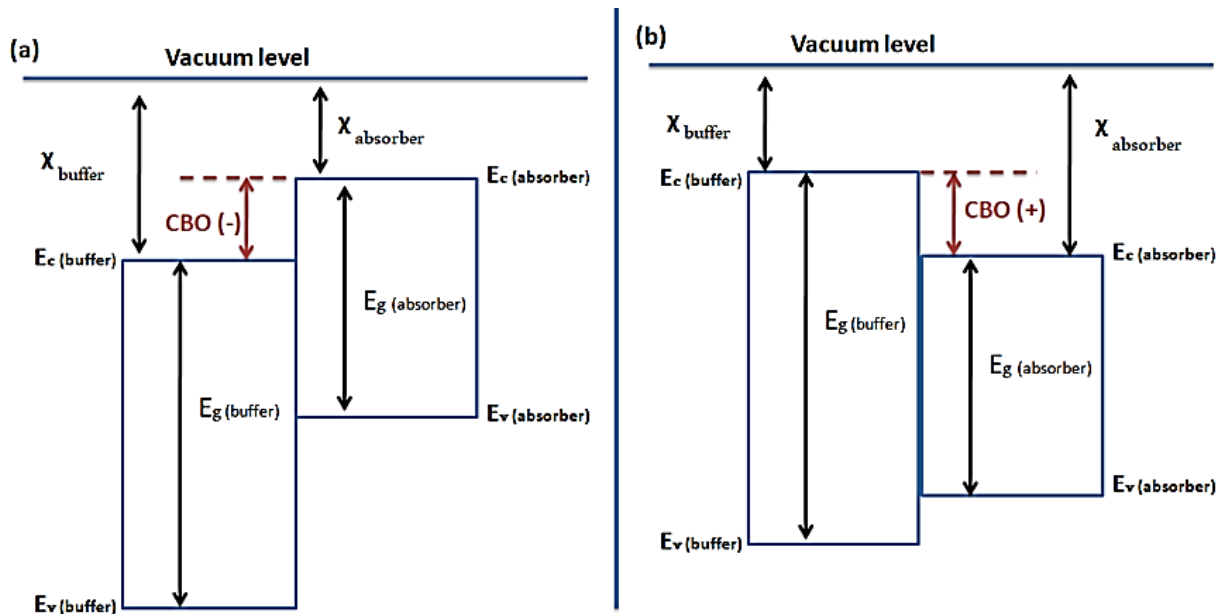
Figure 4.5: Band structure of CBO: (a) negative CBO; (b) positive CBO.
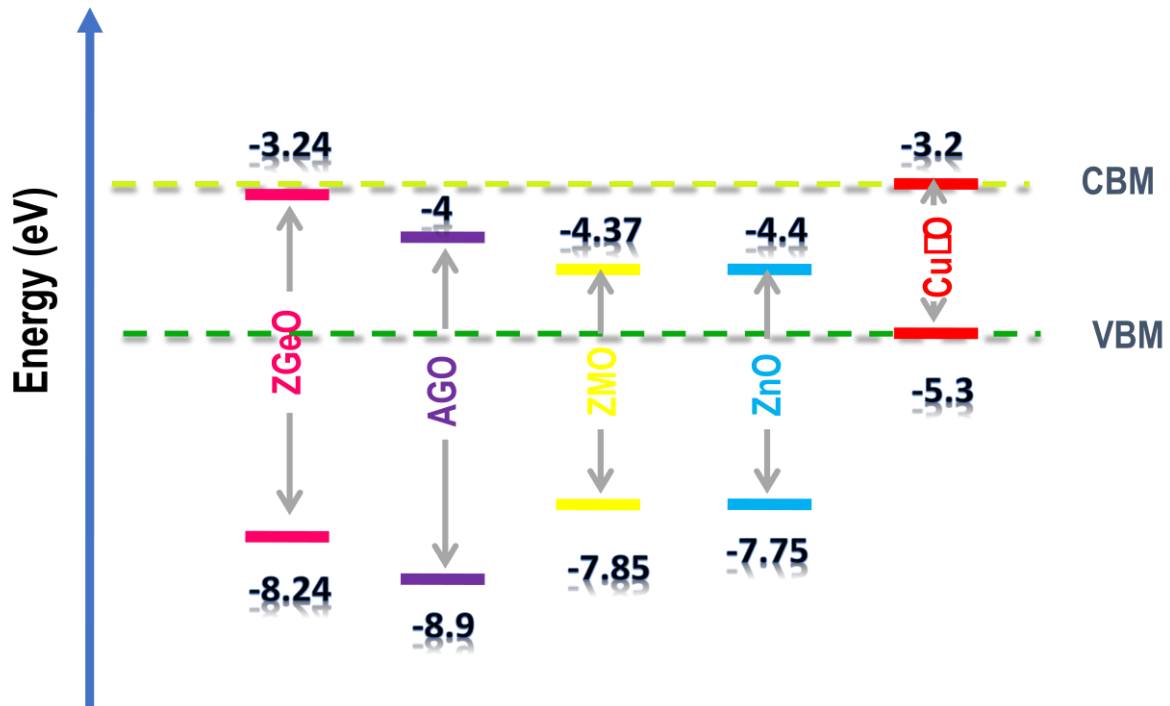
Figure 4.6: Bands alignment between different buffer layers materials and Cu_2O.

In our cases, the n-p junction of the different buffer layers (ZnO, ZMO, AGO, and ZGeO) and Cu_2O have a cliff-type discontinuity of the conduction band because of the low electron affinity of Cu_2O compared to that of the buffer layers. This is shows in Figure 4.6.
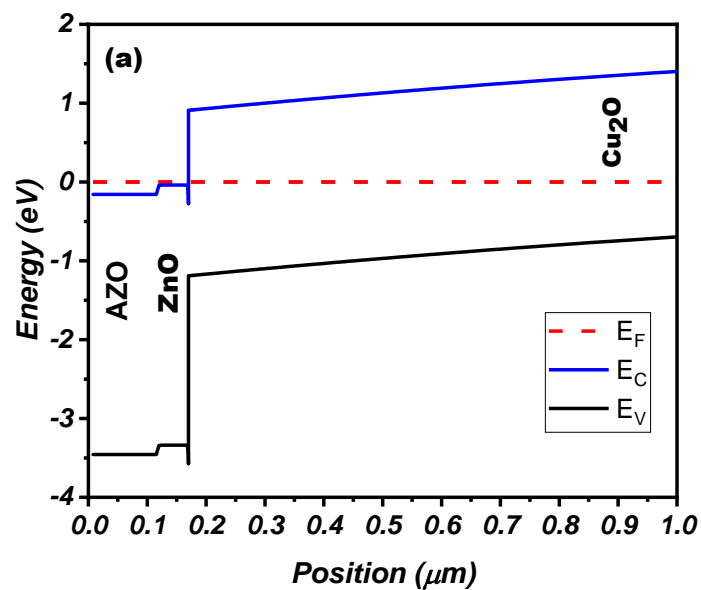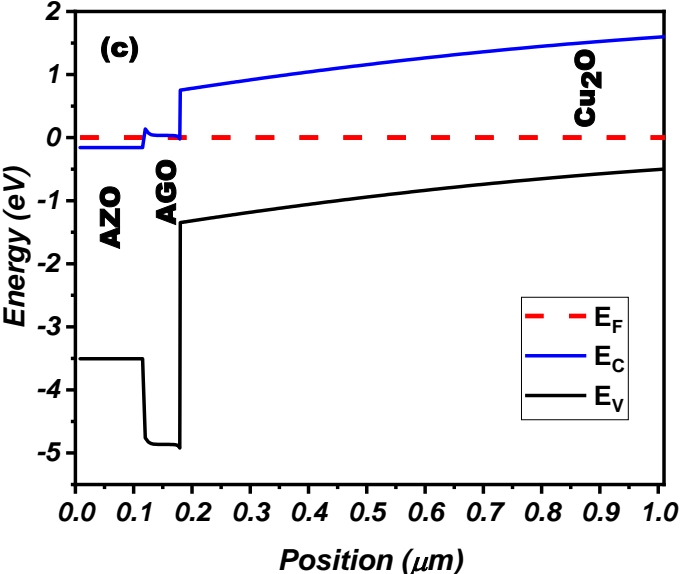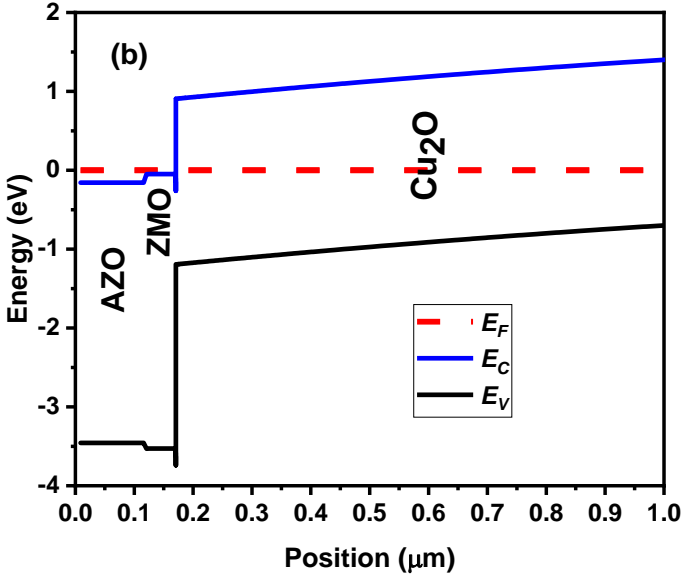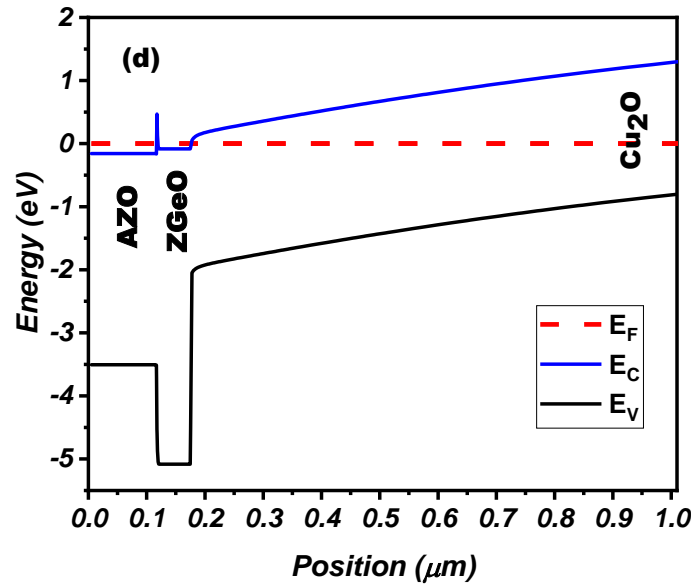
Figure 4.7: Schematic energy band diagram of n-type buffer/ p-Cu$_2$O solar cell (a) ZnO (b) ZMO (c) AGO (d) ZGeO.

The reduction of the value of the conduction band offset (ΔEc) from -1.2 eV (ZnO) to -0.05 eV (ZGeO) (the value of affinity from 4.4 (ZnO) to 4.23 (ZGeO)) gives the band diagrams illustrated in Figure 4.7 (a), (b), (c), (d), where the band discontinuities between the buffer and the absorber layer have changed significantly. The built-in potential at the n-p interface increases when ΔEc decreased from -1.2 to -0.05 because it lowers the barrier in front of electrons moving from the p-side to the n-side. As a result, as the electron affinity decreases, so do both the electric field and the width of the depletion region increase. Also, we remark by examining the band diagrams in Figure 4.7 (c) and (d), an inversion of the type occurred at the n-p interface and induced a noticeable shift of the junction toward the Cu$_2$O absorber layer. This endorses the separation of photo-generated free carriers at the absorber layer by the internal field of the shifted depletion region. Consequently, achievable photovoltaic characteristics such as the open-circuit voltage and fill factor for Cu$_2$O-based heterojunction solar cells manufactured using a more appropriate n-semiconductor may be improved due to a decrease in the height of the conduction band discontinuity [117]. And is what theoretical research demonstrate that the recombination of majority carriers increases with an increase in CBO and the open circuit voltage drops concurrently in a heterojunction solar cell [18].

The conduction band discontinuity between the buffer and absorber layers is not the only cause that affects the efficiency of the cell. Also, the band gap of the buffer layer plays an

important role. It is known, that it is preferable that the band gap of the buffer layer be large in order to allow a greater number of photons, which have less energy, to pass through toward the absorber layer. This means that they are absorbed effectively where the band gap of 5 eV of ZGeO is larger than 4.9 eV of AGO, 3.48 eV of ZMO, and 3.35 eV of ZnO which certifies a better selectivity of minority carriers (electrons) at the interface buffer/Cu_2O and reduces interface recombination. This explains the increase in efficiency of the cells by increasing the bandgap of the buffer layers, respectively.

In addition, the efficiency of the cell is significantly influenced by the carrier concentration of the absorber layer, where a higher hole concentration in Cu_2O would result in higher V_{OC} values and a higher electric field. The depletion width is therefore significantly influenced by the carrier concentration [199]. This explains the high efficiency and high open circuit voltage of both (AGO/Cu_2O) and (ZGeO/Cu_2O) structures, respectively.

Keeping in mind the function of the MgF_2 anti-reflective coating utilized in structures (AGO/Cu_2O) and (ZGeO/Cu_2O), which has a role in raising the efficiency of the solar cell for both of them. All of these explain the noticeable improvement between these structures judging from the structure (ZnO/Cu_2O) with its efficiency of 4.26 % to the structure (ZGeO/Cu_2O) with its efficiency of 8.73 %.

4.4. Optimization of a ZnO/Cu₂O structure solar cell

4.4.1. Effect of hole transport layer (HTL)

In this part, we will try to improve the AZO/ZnO/Cu_2O/Au solar cell which was the first cell suggested for Cu_2O-based solar cell and was previously in section 4.2 simulated and verified to be consistent with the experimental results. We suggest including a back-hole transport layer (HTL) as shown in Figure 4.8. This aims to enhance free hole extraction and block electrons that are responsible of recombination. Three-hole transport materials (HTM) are proposed CuSCN (Copper (I) thiocyanate), CuI (Copper (I) iodide), and NiO (Nickel (II) Oxide), and the optimization of the cell parameters is done in terms of thicknesses and doping concentrations of the device layers.
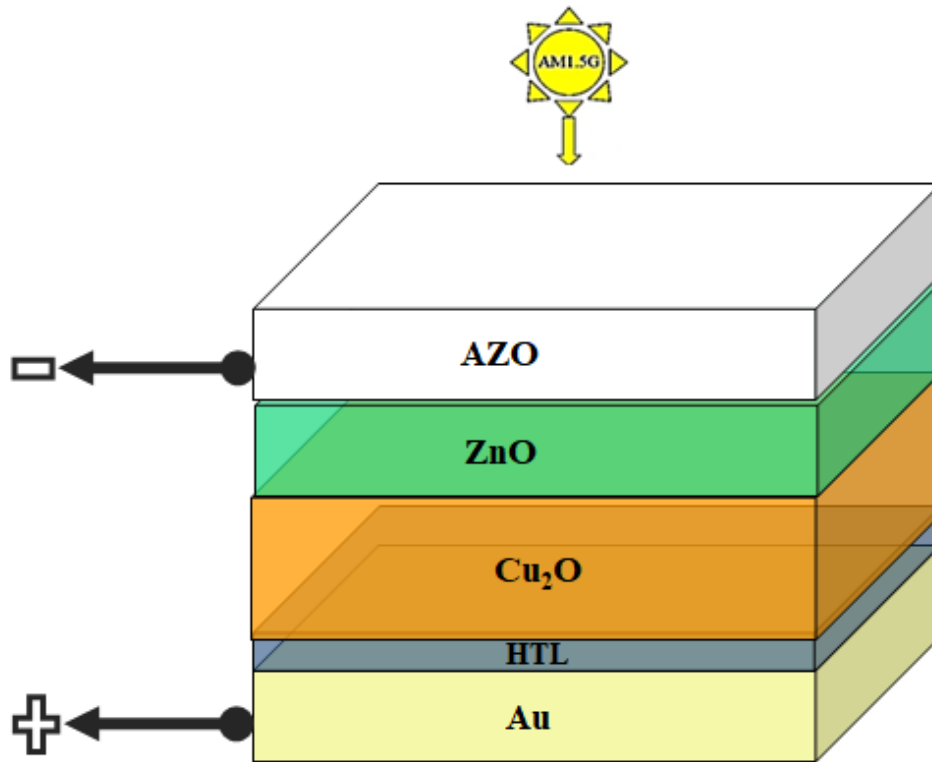
Figure 4.8: Schematic diagram of the proposed structure of the solar cell.

The study of the effect of the HTM on the performance of the solar cell was done using the primary parameters obtained in the preceding section for AZO/ZnO/Cu₂O solar cell. CuSCN, CuI, and NiO are used as hole transport materials with the input parameters given in Table 4.6.

Table 4.6: Summary of the simulation parameters for different HTM [200-206].

Parameters	Description	Layers		
		CuI	NiO	CuSCN
$W(\mu m)$	Thickness	0.05	0.05	0.05
ε_r	Dielectric constant	6.5	11	10
$E_g(eV)$	Bandgap	2.98	3.8	3.4
$\chi(eV)$	Electron affinity	2.1	1.46	1.7
$N_C(cm^{-3})$	Effective density of states of conduction band minimum	2.8×10^{19}	1.6×10^{19}	1.7×10^{19}

$N_V (cm^{-3})$	Effective density of states of the valence band maximum	1×10^{19}	1.1×10^{19}	2.5×10^{21}
$\mu_e (cm^2/V.s)$	Electron mobility	1.7×10^{-4}	50	1×10^{-4}
$\mu_h (cm^2/V.s)$	Hole mobility	2×10^{-4}	50	1×10^{-1}
$N_A (cm^{-3})$	Acceptor concentration	1×10^{18}	1×10^{18}	1×10^{18}
Defect type	-		D-like, Gaussian	
$N_t (cm^{-3})$	Gaussian state density for donor-like	1×10^{15}	1×10^{14}	1×10^{14}

Figure 4.9 and Table 4.7 show the J-V characteristics curves and the photovoltaic output parameters, respectively, of the solar cell having different HTLs. We note that with the use of HTL, all output parameters of the solar cell are further improved compared to the referential solar cell. For instance, the power conversion efficiency (PCE) increases from 4.26 % (without an HTL) to 5.589 % (with an HTL). Solar cell performance with HTLs is improved for many reasons, and the main reason can be traced back to the HTL adjusting the conduction band's and valence band's alignment to pass through holes and block electrons from reaching back contacts. By doing this, the rear-contact surface's recombination rate is decreased and carrier collecting effectiveness is increased [207], where it is the responsibility of HTM to ensure that holes are diffused from the absorber (Cu_2O) to the back contact Au via the internal potential and ultimately to the external circuit. The diffusion-dissociation of the photogenerated charge carriers depends on this layer.

Chapter 4: Results and discussion
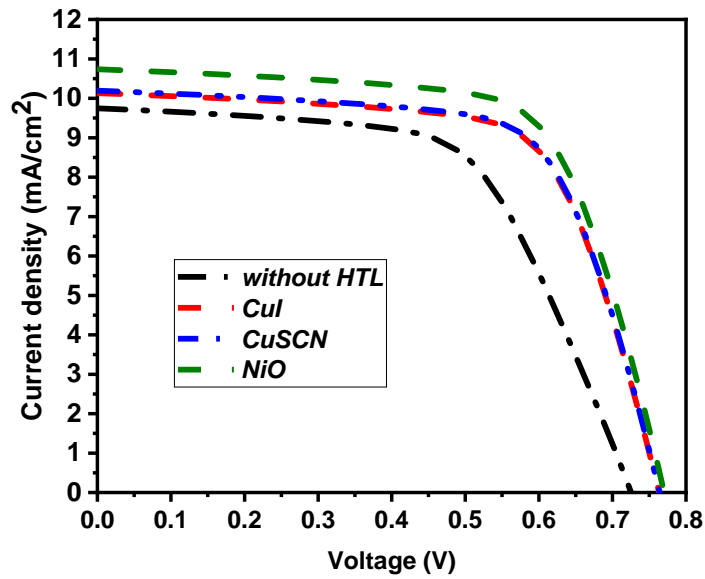
Figure 4.9: J − V characteristics of the simulated solar cells, with and without different HTL layers.

Table 4.7: Photovoltaic parameters of the solar cells with different HTM.

HTM	J_{SC} (mA/cm^2)	$V_{OC}(V)$	$FF(\%)$	$Eff(\%)$
CuSCN	10.1924	0.764215	67.5755	5.26358
NiO	10.7355	0.770302	67.5896	5.58937
CuI	10.1298	0.763487	67.5742	5.22617

In addition, according to the obtained results, we noticed that the efficiency with the NiO HTM was the best compared to the other HTMs (CuI and CuSCN), and the corresponding output parameters are $J_{SC} = 10.735 \, mA/cm^2$, $V_{OC} = 0.77 \, V$, $FF = 67.589$ %, and efficiency = 5.589 %. With CuSCN the solar cell has delivered an efficiency= 5.263 %, $J_{SC} = 10.19 \, mA/cm^2$, $V_{OC} = 0.764 \, V$, and $FF = 67.575$ %. While with CuI provided the lowest efficiency of 5.226 % with $J_{SC} = 10.12 \, mA/cm^2$, $V_{OC} = 0.763 \, V$, and $FF = 67.574$ %.

Chapter 4: Results and discussion

The superior performance of the solar cell with NiO as an HTL was attributed to the alignment of frontier energy levels, suitable electron affinity, and hole mobility of the as-simulated materials, as will be discussed below.

As shown in Figure 4.10, a favorable band alignment at the Cu_2O/NiO interface results from the fact that the valence band maximum, VBM of NiO (- 5.26 eV) is close to that of the Cu_2O layer (- 5.3 eV). This means that the barrier height formatted for free holes is so small with a cliff-like VBO of (- 0.04 eV) at the Cu_2O/NiO interface. Consequently, the flow of free holes from Cu_2O to NiO is easier compared to the other HTMs. Indeed, in the cases of the CuI, and CuSCN HTMs, an energy barrier height of −0.22 eV, and −0.20 eV, respectively, were obtained. This overdue the transport of holes from the absorber layer to the HTL.
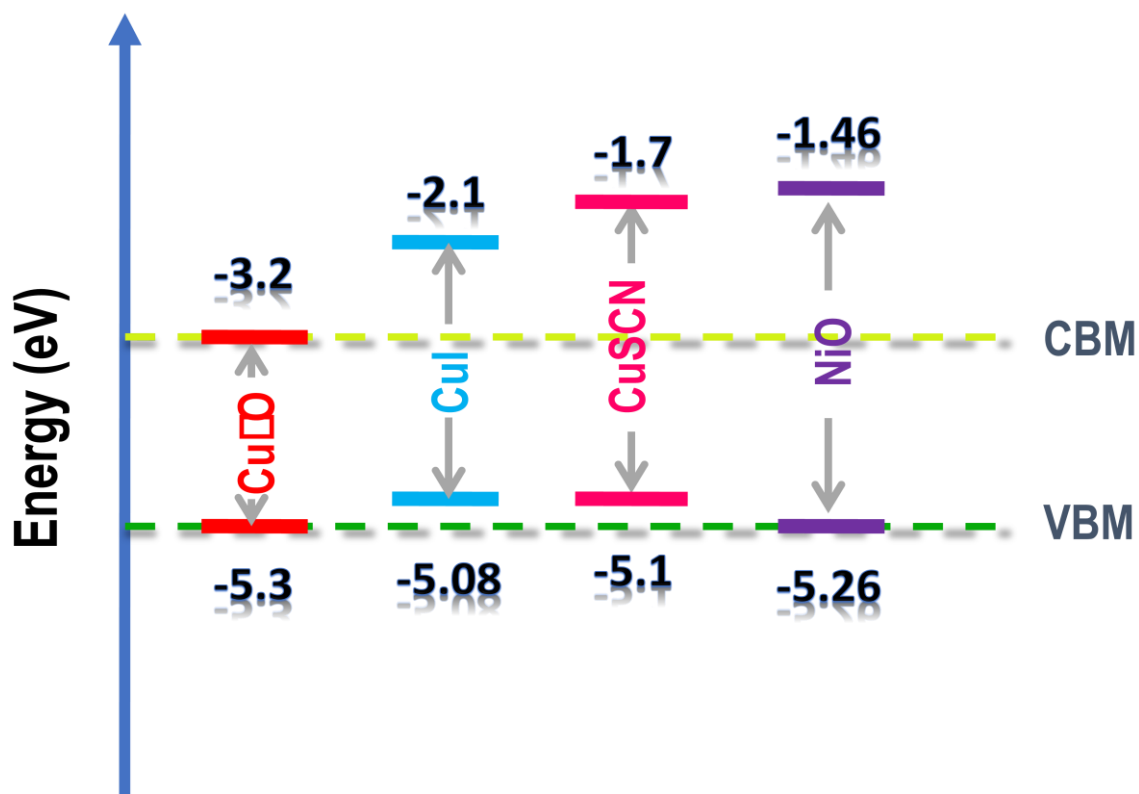
Figure 4.10: The band alignment between the Cu_2O absorber layer and different HTM layers.

In addition, suitable electron affinity between the absorber layer and HTMs leads to rising the conduction band offset (ΔEc) to block electrons. From Figure 4.10, it was proven that NiO has the highest electron-blocking barrier at Cu_2O/HTM interface. The calculated ΔEc values were 1.74 eV, 1.5 eV, and 1.1 eV for NiO, CuSCN, and CuI, respectively.

Chapter 4: Results and discussion

The mobility of the carriers in the material of HTM is an important factor in the efficiency of the solar cell and obviously the hole mobility (μ_p) of the used HTM should be high enough to transport holes before they recombine. The hole mobility in NiO is bigger than the one in the other HTMs. The NiO's hole mobility is 50 cm^2/V s [206] which is the highest compared to its competitors, and is part responsible for the high Voc value obtained, due to the effective extraction and transport of holes in the HTL prior to radiation recombination.

NiO was considered as the best HTM for usage in our study. Therefore, we will reserve it as the HTM in the following sections.

4.4.2. Effect of thickness of absorber layer (Cu$_2$O)

In order to examine the effect of thickness on device performance, we have changed the Cu$_2$O absorber layer thickness from 1 to 300 μm with keeping other parameters constant. The optimal thickness is determined by tracing the J-V characteristics. The obtained characteristic curves and the variation of the PV output parameters with the change in absorber layer thickness are shown in Figures 4.11 and 4.12, respectively.
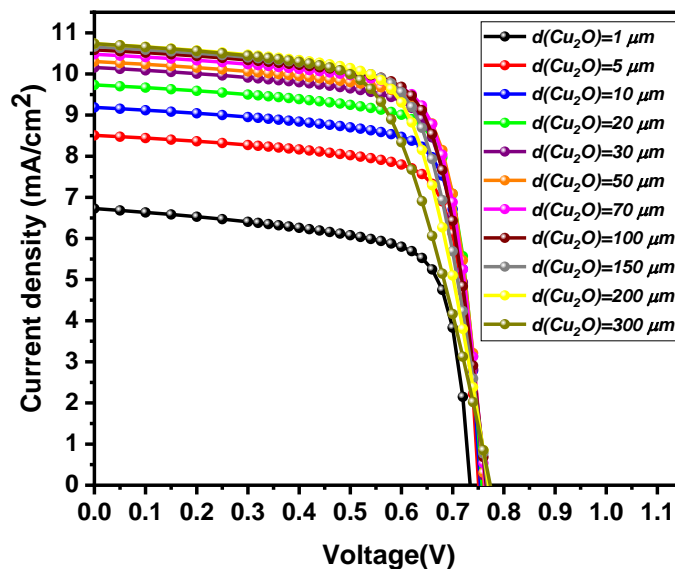
Figure 4.11: Thick of Cu$_2$O with NiO layer as HTL layer.
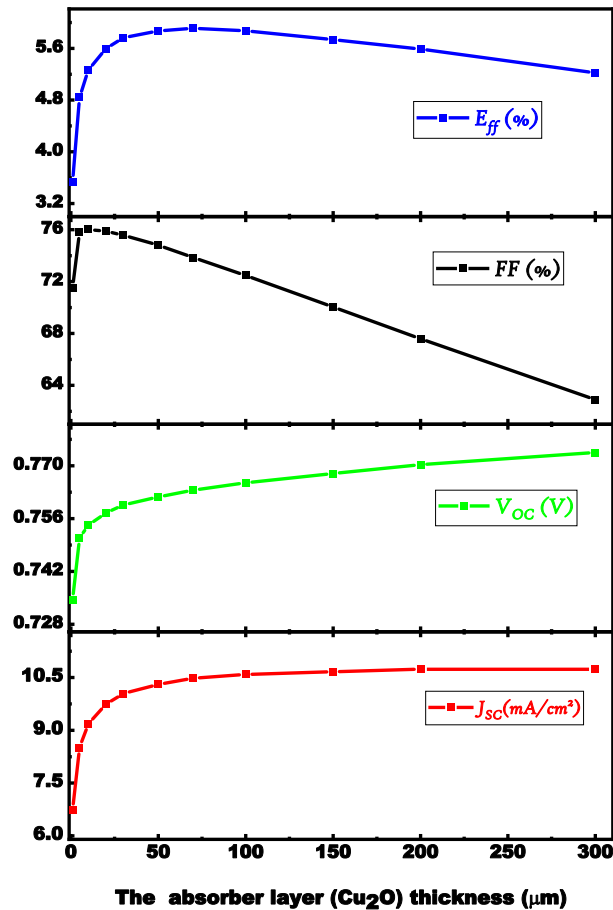
Figure 4. 12: Effect of absorber layer thickness on output parameters with NiO as HTL.

Figures 4.11 and 4.12 depict the effect of absorber layer thickness (1 μm to 300 μm) on the photovoltaic parameters. We can observe the Jsc, the open circuit voltage and the efficiency are rising rapidly with increased absorber thickness until the thickness is 70 μm, which is considered to be the optimal thickness for the solar cell, where they reach their highest values of 10.48 mA/cm^2 and 0.76 V, and 5.909 %, respectively. The reason for this increase in these output parameters is the improving light absorption i.e. the high absorption of wavelength photons in the absorber layer, which leads to the generation of additional charge carriers and an increase in Jsc, and the efficiency is enhanced [208, 209], but after this point, the short circuit current saturates and tends to as nearly almost constant that value. And the open circuit voltage continues to rise slightly, while the efficiency starts decreasing afterward. This deterioration can be attributed to the thickness of the absorber layer increasing relative to the minority carrier length [210], and more charge carriers recombining before reaching the contacts [207, 211]. While the solar cell's FF decreased when the thickness of the absorber

layer was raised, this is attributed to a drop in shunt resistance and increased series resistance [211].

It is clear that a thin absorber layer is not beneficial for a solar cell due to poor light absorption which results in reduced both Jsc and efficiency. But regarding the thicker absorber layer, which increases the probability of recombination for the photogenerated charge carriers, is also not appropriate. Therefore, choosing the optimum cuprous oxide absorber thickness is essential for good efficiency.

4.4.3. Impact of the HTL (NiO) thickness

Figures 4.13 and 4.14 show the variation of the J-V characteristic and output parameters of the solar cell, respectively, for various thicknesses of the HTL ranging from 0.03 to 0.2 μm with the absorber's thickness maintained at 70 μm. And the value of N_A of HTL was fixed to $1 \times 10^{18} cm^{-3}$.
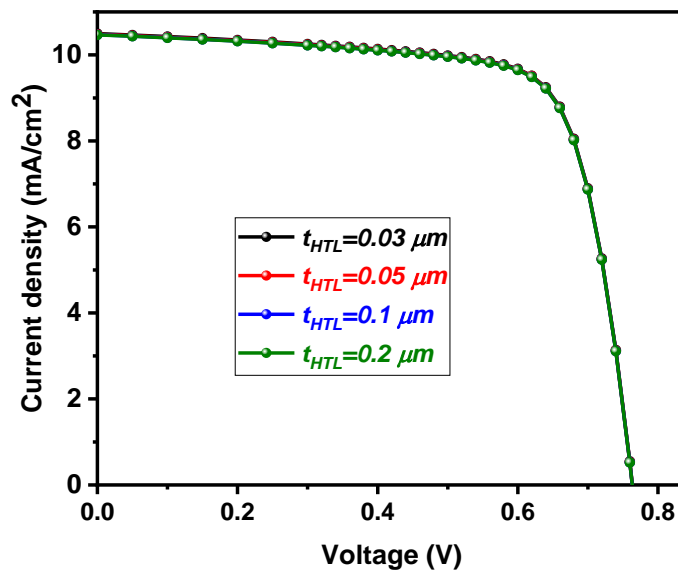
Figure 4.13: Thickness effect of the HTL layer on the J-V characteristic of the solar cell.
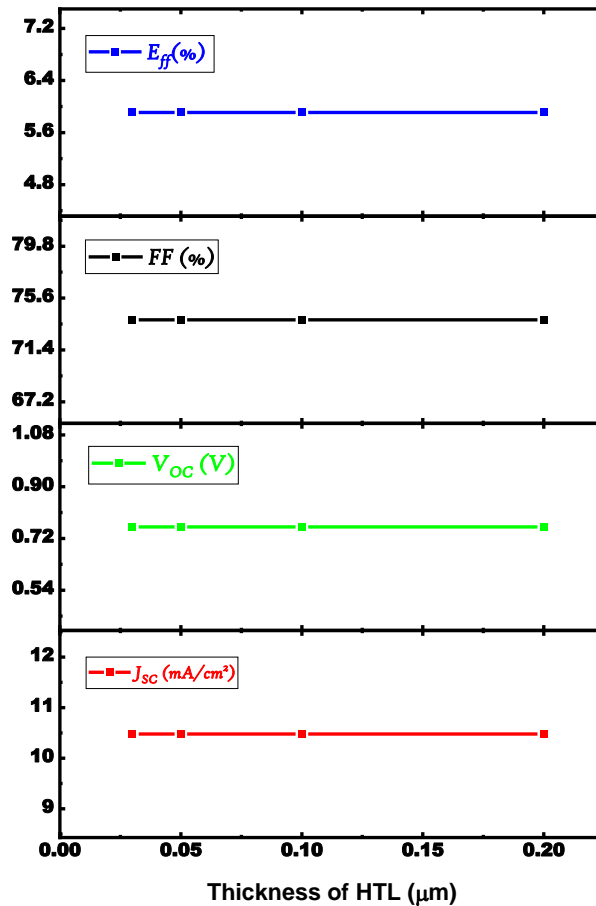
Figure 4.14: Effect of thickness of the HTL on solar cell parameters (Jsc, Voc, FF, and η).

As shown in Figures 4.13 and 4.14 it can be seen that when the thickness of the HTL (NiO) is increased from 0.03 to 0.02 μm the photovoltaic outputs remain constant. This is due to the fact; that sunlight passes through the active absorber layer before reaching the HTL in the solar cell. As a result, most photons are absorbed by the absorber layer and the buffer layer, leaving the HTL with minimal absorption. Therefore, the change in the thickness of the HTL has no effect on the amount of photo-generated charge carriers. Thus, it does not affect the performance of the solar cell.

4.4.4. Impact of the HTL doping concentration

Finding the ideal HTL material and its appropriate thickness is important, but it's also vital to find an optimal value of the acceptor doping concentration (N_A). For this, the impact of the doping concentration of the NiO HTL on the J-V characteristic and output parameters of the solar cell has been investigated. It can be seen in Figures 4.15 and 4.16, respectively; where the doping concentration of an HTL was changed from $1 \times 10^{16} cm^{-3}$ to $1 \times 10^{19} cm^{-3}$,

while keeping the thickness of the absorber layer and HTL at optimal values of 70 μm, and 0.05 μm, respectively.
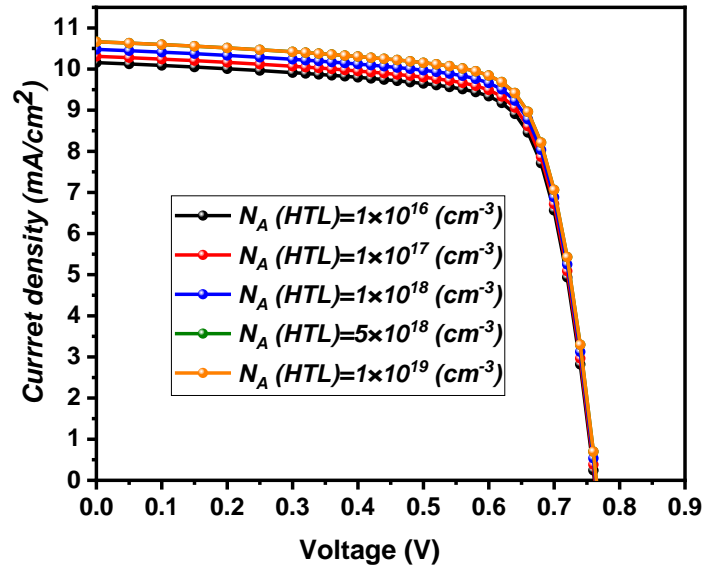
Figure 4.14: J-V characteristic as a function of the HTL doping concentration.
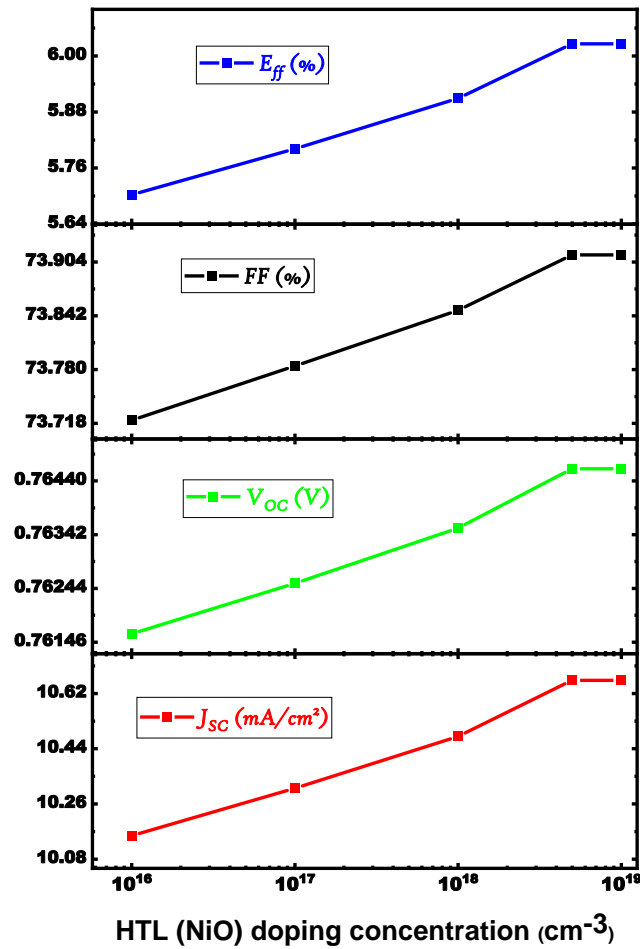
Figure 4.16: Output parameters as a function of the HTL doping concentration.

From Figures 4.14 and 4.16, it can be observed that all the solar cell output parameters are slightly improved with an increase in the doping concentration of HTL. Where the Jsc slightly increased from 10.1565 to 10.663 mA/cm^2 as the doping concentration of the HTL was increased from $1 \times 10^{16} cm^{-3}$ to $1 \times 10^{19} cm^{-3}$. As well as the Voc was increased from 0.7616 to 0.7646 V. The efficiency was thus improved from 5.7025 to 6.026 %. The reason for this improvement is that an increase in the doping concentration results in it moving the Fermi level of HTL toward to valence band, resulting in ohmic contact with the Au back-metal electrode and, in turn, an efficient collection of holes at the contact [212]. Also, this is when the HTL is highly doped; the interface recombination is reduced because of the strong electric field generated at the HTL/absorber interface, which prevents minority electrons from flowing toward the interface [212].

Chapter 4: Results and discussion

And we observe an increase in FF was thus changed from 73.7216 to 73.91 %, the reason for the improvement of the fill factor with increasing the doping of HTL is due to the improvement of the sheet resistance and conductivity [213].

4.4.5. Effect of back metal work function

Figures 4.17 and 4.18 illustrate the J-V characteristics curve and the efficiency calculated from different back-contact work functions, by changing the back electrode work function from 4.65 to 5.3 eV. The work function of several metals used as PSC back contact electrodes is displayed in Table 4.8.

Table 4.8: Back electrode metals work function [214].

Back Electrode	Ag	Pd	Cu	Ni	Au
Work Function (eV)	4.7	5.3	4.65	5.0	5.1
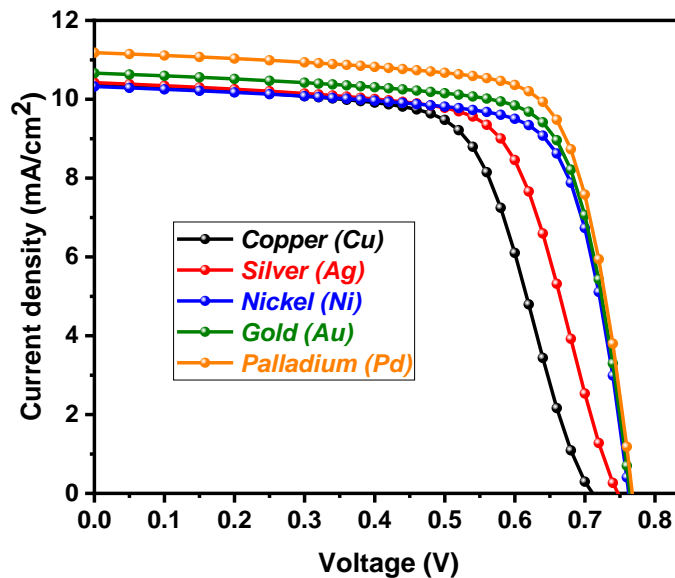
Figure 4.17: J-V curves of the solar cell for different work functions of the back electrode.

Figure 4.18: Power conversion efficiency as a function of the different work functions of the back electrode.

From our results, we can observe that the efficiency of the solar cell and the work function of the back electrode are increased together. where when φ (metal back work function) is at low values as a Cu (4.65 eV), can observe the decline in Voc (0.71V) is due to the decline in Vbi, which results in an ineffective collection of photogenerated carriers, and it can be seen Jsc is also slightly reduced [215]. And leading to a Schottky junction forming at the HTL/back-contact interface, which causes the cell performance to decrease dramatically, where in this case, the efficiency is 4.792 %.

But with an increase in the metal's work function, the barrier height for holes at the back-contact interface decreases, allowing for easy hole transport from the HTL to the back contact, leading to an enhancing the efficiency of solar cells [207]. As in the case of gold (5.1 eV), it gave an efficiency of 6.03 %, and an open circuit voltage is 0.765 V. Also, the greatest efficiency, which is 6.36 %, is achieved when the back electrode is made of palladium material (Pd), which has a work function of 5.3 eV. Because it is well known that solar cells become more effective as their work function is increased. This happens because more ohmic contact is produced when the work function value increases due to a drop in the majority carrier's barrier height [216, 217]. And for this, we will choose our study palladium as the best material for the back electrode.

Chapter 4: Results and discussion

It was created the new ideal structure for the ZnO/Cu$_2$O solar cell by integrating the optimal parameters that were found. This through to establish the optimum doping values and thickness of the HTL and the optimal thickness of the absorber layer as well as the optimum metal-work function for back contact. As it has been demonstrated, in comparison to the reference efficiency, where it was conversion efficiency initially in the ZnO/Cu$_2$O heterojunction solar cell was 4.26 %, our optimization enabled us to achieve an efficiency of 6.36 %. Table 4.9 and Figure 4.19 reveal the results of our simulation for comparison between the photovoltaic parameters of the cell after the optimization and those of the same cell before the optimization.

All these simulated results can be useful, for experimenters looking to enhance the performance of their cells in the future.
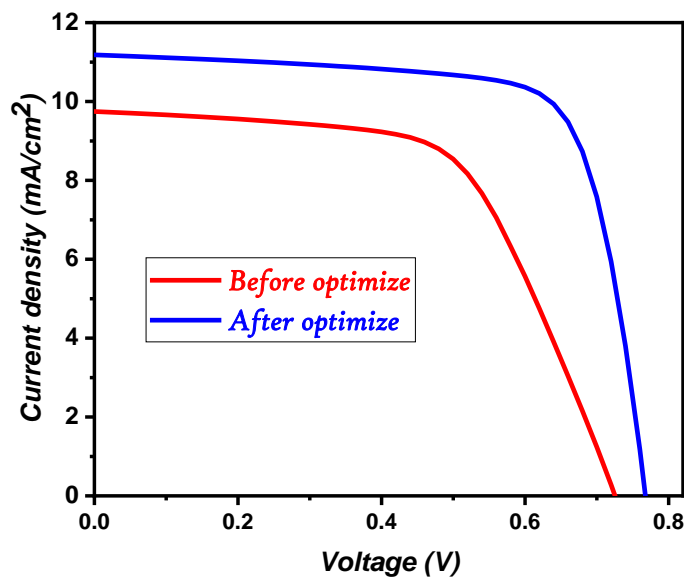
Figure 4.19: J-V characteristics of the ZnO/ Cu$_2$O heterojunction solar cell; before optimize (Red), after optimize (Blue).

Table 4.9: Comparison of output parameters of the ZnO/ Cu$_2$O heterojunction solar cell before and after optimization.

Parameters	$J_{sc}(mA/cm^2)$	$V_{oc}(V)$	$FF(\%)$	$Eff(\%)$
Simulation initial	9.74	0.72	60.37	4.26
Simulation optimized	11.18	0.77	74.07	6.36

4.5. Optimized of ZGeO/ Cu₂O heterojunction solar cell

When choosing the material that composes the cell's buffer layer, many criteria that have an effective role in the efficiency of the solar cell must be taken into consideration, including the bandgap and the electron affinity, as well as the alignment between it and the absorber layer and also not forgetting the role of the TCO in the efficiency. This is what we will cover in the fourth part of this work; we will optimize the structure ZGeO/Cu₂O through changing input parameters for both ZGeO and AZO, where this device was verified to be consistent with the experimental results in the previous part (second part).

4.5.1. Effect of the bandgap of the buffer layer (ZGeO) on the performance of the solar cells

The obtained J-V characteristics and parameters photovoltaic are shown in Figures 4.20 and 4.21, respectively, by varying the band gap of the buffer layer from of 4.8 to 5.5 eV while fixing the electron affinity for both ZGeO and AZO at 3.24 eV and 4.4 eV, respectively.
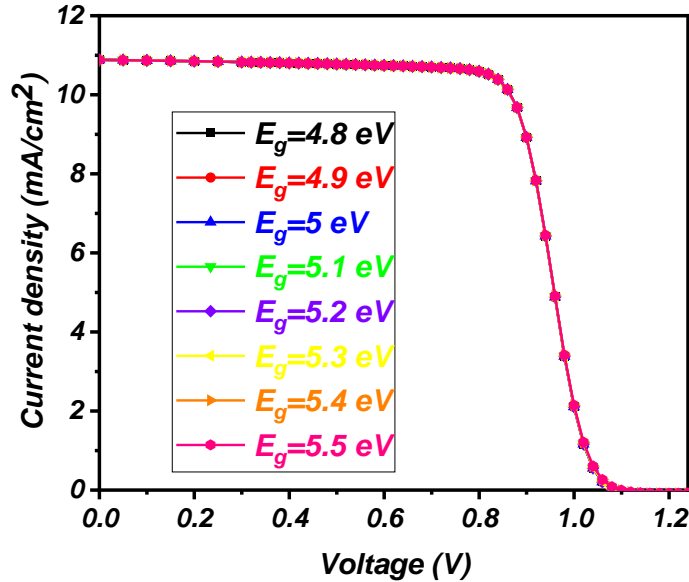
Figure 4.20: Effect of band gap of the buffer layer (ZGeO) on J-V characteristics.

91
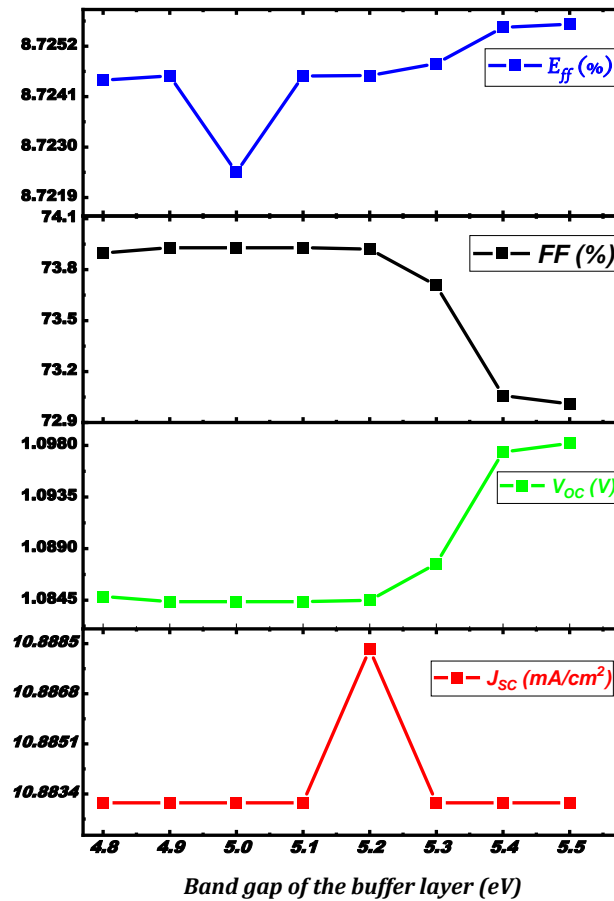
Figure 4.21: The electrical parameters of the solar cell as a function of the bandgap of the buffer layer (ZGeO).

In our results, we observe in all outputs very little changes. For example, V_{oc} increases slightly from 1.08 to ~ 1.1 V with the band gap of the buffer layer while the *FF* decreases also slightly from 73.8 to 72.9 %. This gives efficiency unaffected. It is well known that there is a relationship between band gap energy and V_{oc} and its little increase is responsible for the minor diminution in fill factor (FF).

It is worth noting that an increase in the band gap of the buffer layer gets the output parameters of the structure ZGeO/Cu$_2$O closer to the experimental results.

4.5.2. Effect of electron affinity of the buffer layer on the performance of the cell

Figure 4.22 illustrates J-V characteristics as a function of electron affinity where it ranged from 4 to 3 eV. While taking into account the band gap of the ZGeO layer is $5.5 eV$.
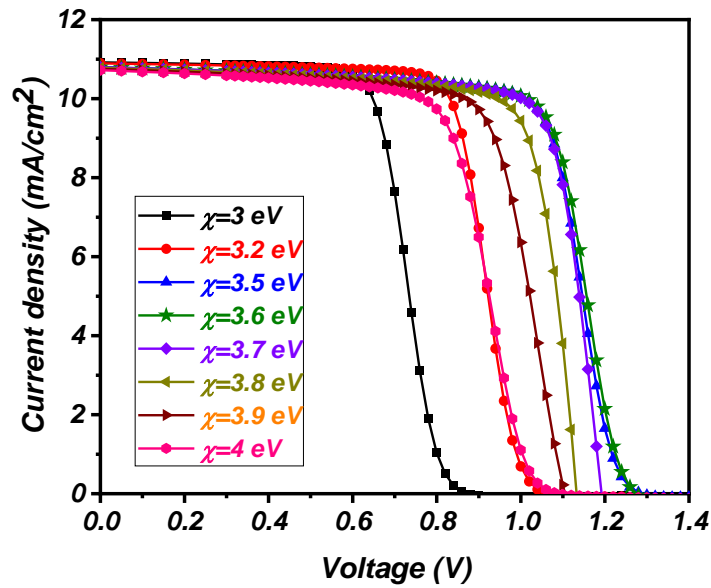
Figure 4.22: Effect of the electron affinity of the buffer layer (ZGeO) on J-V characteristics.

Through analysis of the J-V characteristics, the solar cell's output parameters were determined and are presented in Figure 4.23. We can observe that electronic affinity has a significant impact. At an electronic affinity of 3.5–3.6 eV, V_{OC} and efficiency are at their optimum values, respectively ~1.29 V and 10.2%, before declining to lower values; FF peaks at 78.4% at 3.7 eV. However, as the affinity increases from 3 to 4 eV, J_{SC} decreases from 10.92 to 10.72 mA/cm^2.
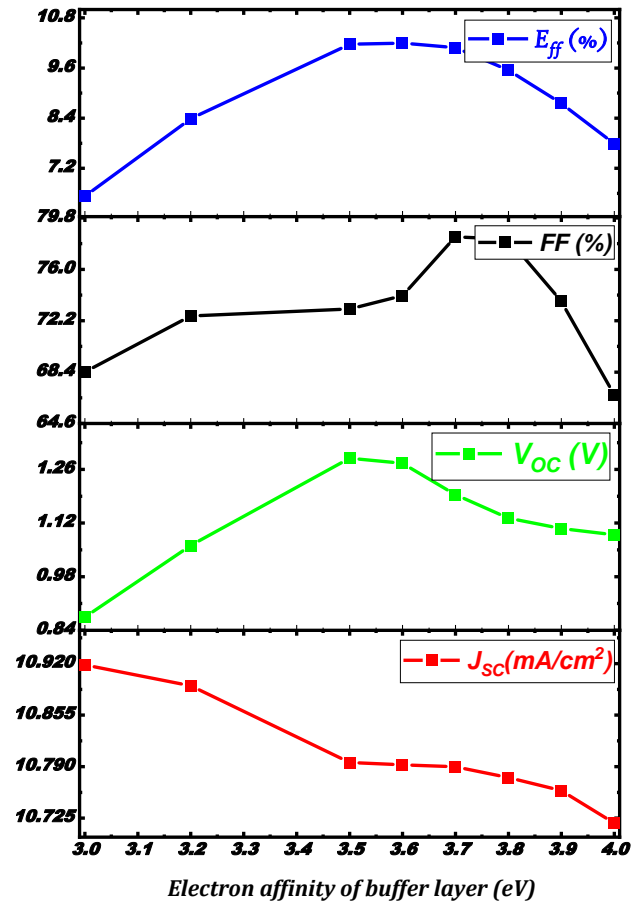
Figure 4.23: The electrical parameters of the solar cell as a function of the electron affinity of the buffer layer.
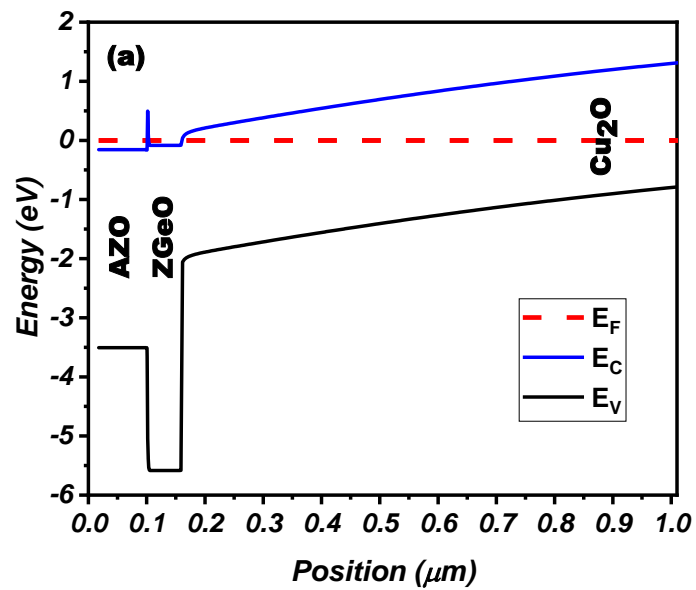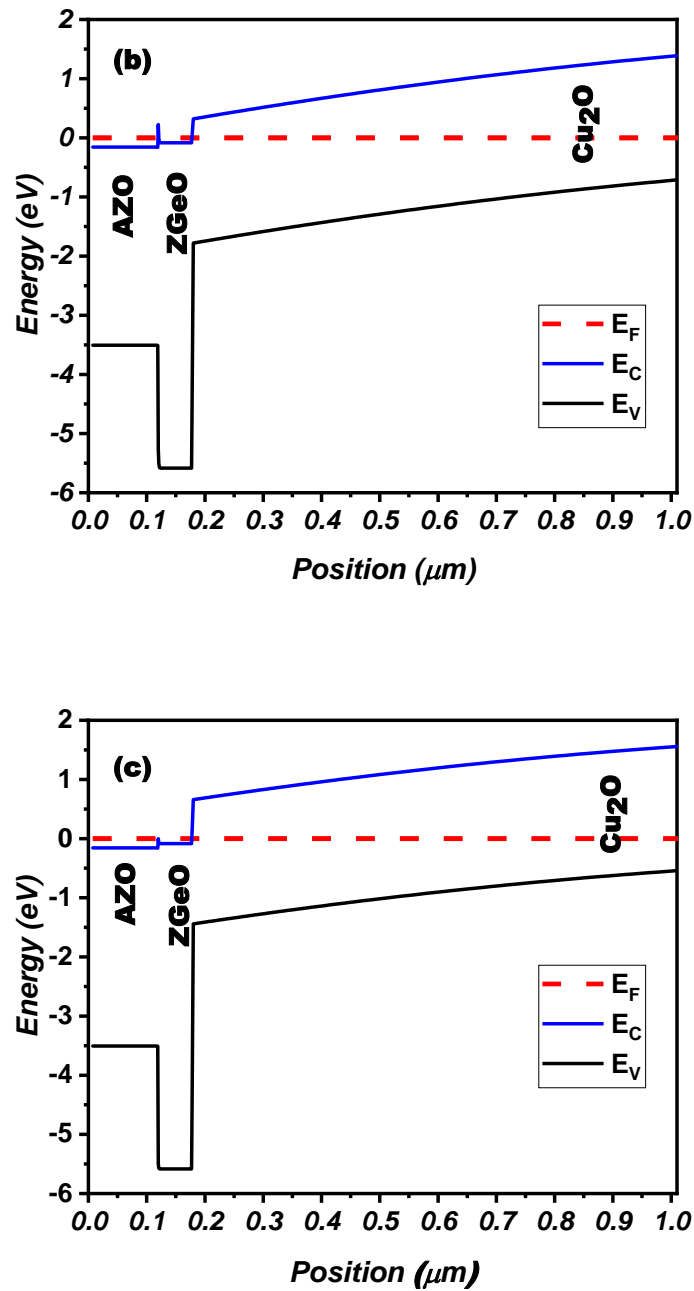
Figure 4.24: The band gap of the buffer layer (ZGeO) at equilibrium for electronic affinity of (a) 3.2 eV, (b) 3.6 eV and (c) 4 eV.

On the basis of the band gap diagram shown in Figure 4.24 (a), (b), and (c), more explanation is provided. At an electron affinity of 3eV, we see a significant the ΔE_C at the AZO/ZGeO interface, as well as a dramatic drop in Voc and FF. The ZGeO/Cu$_2$O side maintains the necessary inversion type while also establishing the depletion region, as well as the n/p

junction, which is well established and extended in the absorber layer. When an affinity of 3.6 eV, ΔE_C is decreasing at the AZO/ZGeO interface and increases at the ZGeO/Cu$_2$O interface. This is because the strong type inversion remains preserved and this has a positive effect on the values of Voc and FF, and hence on the efficiency. And with the affinity of 4 eV ΔE_C becomes more significant, and thus, the n/p junction moves toward ZGeO/Cu$_2$O. This undesirably influences the separation of photo-generated carriers in the Cu$_2$O absorber layer.

Moreover, for large conduction band offset, the carriers (electrons) resulting from photo-generated in the absorber layer will be confined, this leading to recombination at the interface-by-interface defects [218-220], It explains the decrease in the open circuits voltage. We can see that as the electron affinity of the buffer layer increased to a value greater than 3.7 eV, all of the output parameters of the solar cell decreased, primarily because of the cliff form between the buffer and absorber layers, which increased recombination between carriers and defects at the interface and, which it led decreasing Voc. Decreased FF can be attributed to decreasing in the electric field caused by insufficient carrier collection [220, 221]. Also, the fill factor decreases when the formation of a high spike or a deep cliff [219]. Hence, this will result in a decline in efficiency.

4.5.3. Effect of the affinity of the front window AZO on the performance of solar cell

This section will study the influence of the electron affinity of the front window (AZO) on the electrical characteristics of the AZO/ZGeO/Cu$_2$O solar cell structure. This was achieved by keeping bandgap (E_g) and electron affinity (χ) of ZGeO constant at 5.5 eV and 3.6 eV, respectively; where the two values match the previously discussed optimal values for best efficiency. The electron affinity of AZO is changed from 4 to 4.5 eV. Figures 4.25 and 4.26 illustrate both the modeled J-V characteristics and output parameters.
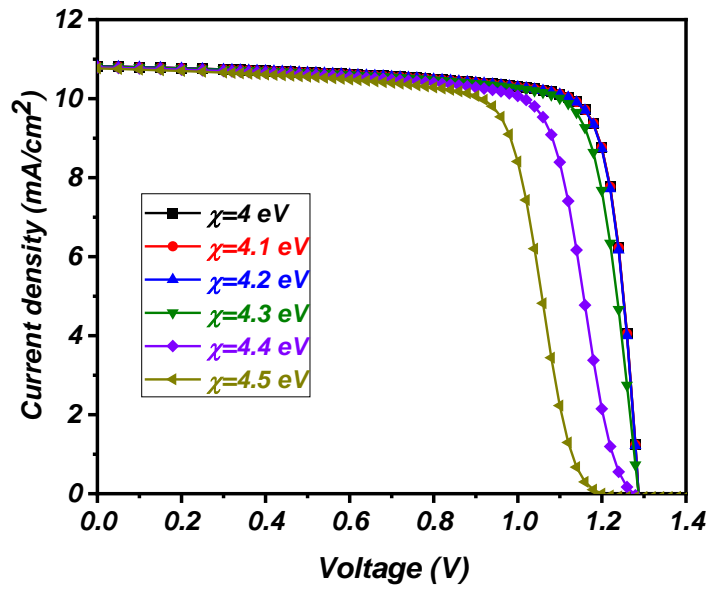
Figure 4.25: Effect of the electron affinity of front window on J-V characteristics.
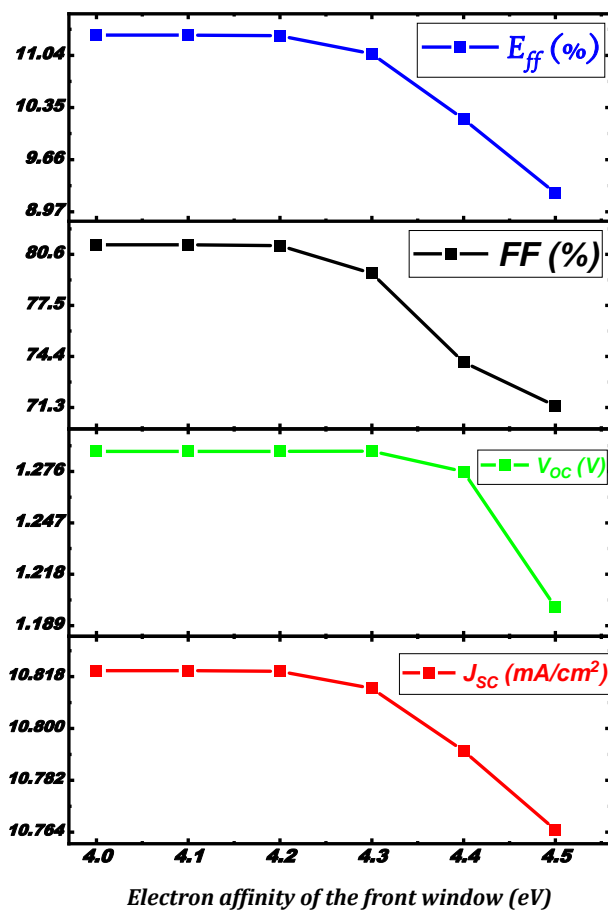
Figure 4.26: Simulation of output parameters of the solar cell as a function of the electron affinity of the front window.

Chapter 4: Results and discussion

Figures 4.25 and 4.26 show that as the electron affinity of AZO was increased from 4 to 4.5eV, all of the solar cell's output parameters dropped during the simulation process. This is because the discontinuity between the AZO and the buffer layer (ZGeO) increases whenever the electron affinity of the AZO is great, which results in slowing down the transport of electrons resulting from the absorption of photons in the absorber layer (Cu_2O) and their separation at the interface ($ZGeO/Cu_2O$) while the holes are transported to the anode (Au). As can be observed in Figure 4.28, the band gap diagram of this solar cell, the decrease in output of the solar cell is due to the impeding in the transport of the electrons.
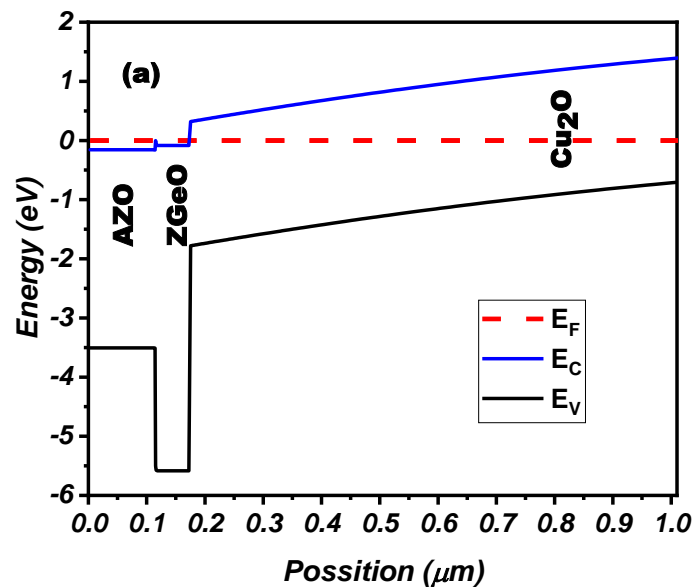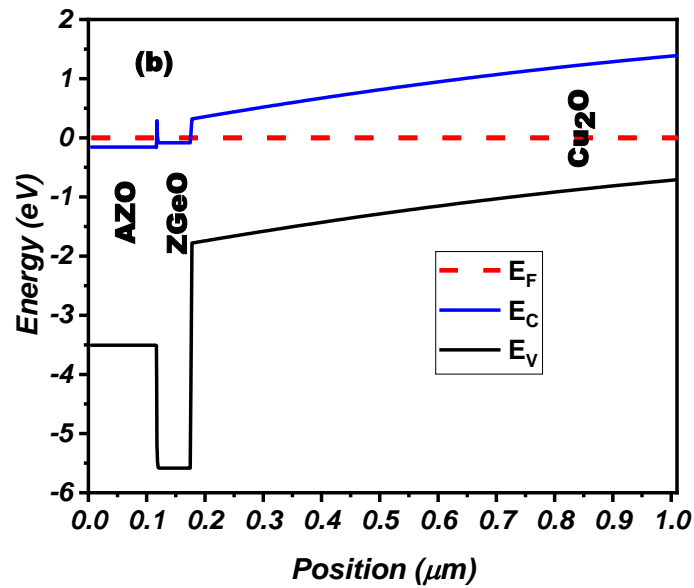
Figure 4.27: The band gap diagram at equilibrium for electron affinity of the front window (AZO) (a) 4eV (b) 4.5 eV.

The best values that lead to the high efficiency of the ZGeO/Cu$_2$O solar cell were achieved after studying the effect of improving the parameters of each of the band gap of the buffer layer as well as the electron affinity for each of the buffer and the front window layers, respectively. The J-V characteristics and output parameters for comparison of both the optimized and the initial ZGeO/Cu$_2$O solar cell are shown in Figure 4.28, and Table 4.10, respectively.
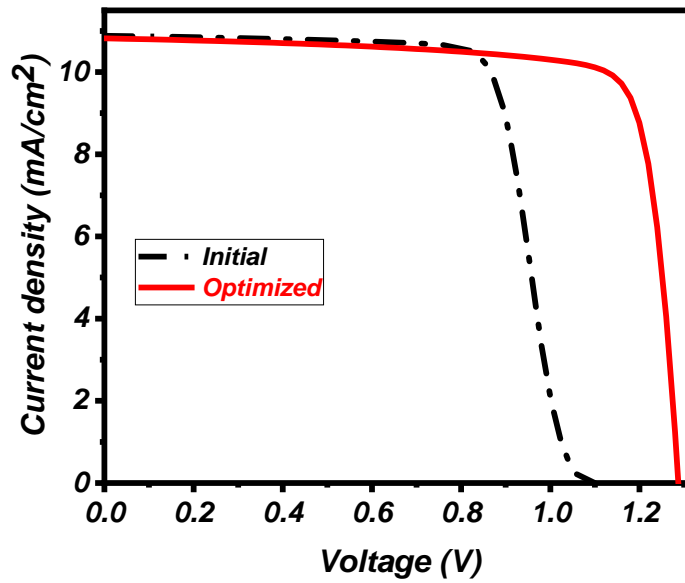
Figure 4.28: J-V characteristics comparison of the ZGeO/Cu₂O solar cell before and after optimization.

Table 4.10: Comparison of the ZGeO/Cu₂O solar cell output parameters before and after optimization.

Parameters	Initial	Simulation optimization
$J_{SC}(mA/cm^2)$	10.88	10.82
$V_{OC}(V)$	1.08	1.28
$FF(\%)$	73.92	81.18
$Eff(\%)$	8.72	11.30

General Conclusion

General Conclusion

Cuprous oxide (Cu_2O) has attracted great interest from research scientific due to its low-cost, abundance, non-toxic and high absorption coefficient as well as theoretical power conversion efficiency of about 20%. All these features did make cuprous oxide as interesting as solar cell material. However, due to the difficulty of forming the n-type of this material, that's made these materials encountered challenges that would restrict their capabilities in building a p-n homojunction solar cell, instead, researchers focused on p-n heterojunction, and indeed many reports have emerged on heterojunction solar cells based on cuprous oxide (Cu_2O) as an active layer with different n-type semiconductors.

In order to optimize the device performance proficiently and to provide a clear understanding of Cu_2O-based-heterojunction solar cell performance, we developed a comprehensive simulation that accurately describes the device operation, by performing several sets of simulations over main physical parameters based on experimental results.

In the preliminary study, AZO/Cu_2O heterojunction solar cell structures were simulated at AM1.5G solar spectrum with an incident power density of $100mW/cm^2$ at room temperature (300 K). This structure showed relatively poor performance, where the power conversion efficiency was about 2.578 % for this structure which is consistent with the experimental results. The poor performance of this structure was related to the defect states at the junction interface where these act as traps for the charge carriers generated by the photons.

In order to improve the performance of this structure, so, several materials were effect studied for possible buffer layers (n-type) where we added different buffer layers between the n+-AZO layer and the absorber layer ZnO, ZMO, AGO, and ZGeO and compared to their experimental results, where we found that it's a good agreement with the measured values. And we found that replacing the buffer layer with a small band gap and high-conduction band offset buffer for a buffer layer large with a band gap and low-conduction band offset improved the solar cells performance where the power conversion efficiency was 4.26 % for a solar cell with ZnO as a buffer layer to 8.73 % for a solar cell with ZGeO as a buffer layer. Also, it was good band alignment between the buffer layer and the absorber layer one of the most prominent reasons that led to this remarkable improvement.

Based on the experimental studies available, we have pursued two types of solar cells, one with a ZnO buffer layer and another with ZGeO, where the primary solar cell (ZnO/Cu_2O)

was improved by several optimization techniques. First, we added an HTM layer between the absorber layer and the metal back contact. where several hole transport materials (CuI, CuSCN, and NiO) were studied to choose the most suitable one for the solar cell, after analyzing the obtained results, we noticed a significant increase in efficiency with all HTL materials, but it was found that NiO HTL gives the best efficiency of $\eta = 5.58$ %. Then, was also studied the effect of the thickness of the absorber layer, as well as the thickness and doping concentration of the HTL on the performance of the solar cell, in these considerations, the efficiency has improved to $\eta = 6.02$ %. The third step suggested in this improvement was choosing the suitable metal for the back electrode to form good contact with high efficiency. Where we found that the efficiency, in this case, has increased significantly to $\eta = 6.36$ % with the palladium (ϕ=5.3 eV) as the best back electrode.

But regarding the ZGeO/Cu$_2$O heterojunction solar cell, we have improved it through study the bandgap and electron affinity of the buffer layer (ZGeO) and the electron affinity of the front window (AZO), and studied their effects. Under these considerations, the power conversion efficiency of the ZGeO/Cu$_2$O heterojunction solar cell reached 11.30 %.

These studies, which also included choosing the optimal parameters and adding various optimization, it can be made a significant impact on the development of Cu$_2$O-based heterojunction solar cells and enhance their performance in the future.

References

References

1. Owusu, P.A. and S. Asumadu-Sarkodie, A review of renewable energy sources, sustainability issues and climate change mitigation. Cogent Engineering, 2016. **3**(1): p. 1167990.

2. Parida, B., S. Iniyan, and R. Goic, A review of solar photovoltaic technologies. Renewable and sustainable energy reviews, 2011. **15**(3): p. 1625-1636.

3. Renewables, I., Analysis and Forecast to 2025. IEA: New York, NY, USA, 2020.

4. Grätzel, M., Dye-sensitized solar cells. Journal of photochemistry and photobiology C: Photochemistry Reviews, 2003. **4**(2): p. 145-153.

5. Yang, W.S., et al., Iodide management in formamidinium-lead-halide–based perovskite layers for efficient solar cells. Science, 2017. **356**(6345): p. 1376-1379.

6. Shi, Z. and A.H. Jayatissa, Perovskites-based solar cells: A review of recent progress, materials and processing methods. Materials, 2018. **11**(5): p. 729.

7. Boyd, C.C., et al., Understanding degradation mechanisms and improving stability of perovskite photovoltaics. Chemical reviews, 2018. **119**(5): p. 3418-3451.

8. Baines, T., et al., Incorporation of CdSe layers into CdTe thin film solar cells. Solar Energy Materials and Solar Cells, 2018. **180**: p. 196-204.

9. Jackson, P., et al., Effects of heavy alkali elements in Cu (In, Ga) Se2 solar cells with efficiencies up to 22.6%. physica status solidi (RRL)–Rapid Research Letters, 2016. **10**(8): p. 583-586.

10. Green, M.A., et al., Solar cell efficiency tables (version 56). Progress in Photovoltaics: Research and Applications, 2020. **7**(28): p. 629-638.

11. Ramanujam, J., et al., Flexible CIGS, CdTe and a-Si: H based thin film solar cells: A review. Progress in Materials Science, 2020. **110**: p. 100619.

12. Rix, A., et al., First Solar's CdTe module technology–performance, life cycle, health and safety impact assessment. Centre for Renewable and Sustainable Energy Studies, 2015.

13. Bhatnagar, A., A. Johari, and V. Janyani, PHOTON RECYCLING FOR IMPROVED ABSORPTION IN THIN FILM ITO/INP HETEROSTRUCTURE SOLAR CELL.

14. Chuangchote, S., et al., Review of environmental, health and safety of CdTe photovoltaic installations throughout their life-cycle. First Solar http://www. firstsolar.

com/-/media/First-Solar/Sustainability-Documents/Sustainability-Peer-Reviews/Thai-EHS-Peer-Review_EN. ashx, 2012.

15. Tolstova, Y., et al., Polycrystalline Cu2O photovoltaic devices incorporating Zn (O, S) window layers. Solar Energy Materials and Solar Cells, 2017. **160**: p. 340-345.

16. Tanaka, H., et al., Electrical and optical properties of TCO–Cu2O heterojunction devices. Thin solid films, 2004. **469**: p. 80-85.

17. Wei, H., et al., Photovoltaic efficiency enhancement of Cu2O solar cells achieved by controlling homojunction orientation and surface microstructure. The Journal of Physical Chemistry C, 2012. **116**(19): p. 10510-10515.

18. Yang, M., et al., Asymmetric interface band alignments of Cu2O/ZnO and ZnO/Cu2O heterojunctions. Journal of alloys and compounds, 2013. **578**: p. 143-147.

19. Minami, T., Y. Nishi, and T. Miyata, Efficiency enhancement using a Zn1− x Ge x-O thin film as an n-type window layer in Cu2O-based heterojunction solar cells. Applied Physics Express, 2016. **9**(5): p. 052301.

20. Georgieva, V. and A. Tanusevski. Characterization of p-Cu 2 O/n-ZnO Heterojunction Solar Cells. in AIP Conference Proceedings. 2010. American Institute of Physics.

21. Kara, R., et al., Electrochemical growth and characterization of Cu2O: Na/ZnO heterojunctions for solar cells applications. Journal of alloys and compounds, 2020. **817**: p. 152748.

22. Owens, A., Compound semiconductor radiation detectors2016: Taylor & Francis.

23. Mertens, K., Photovoltaics: fundamentals, technology, and practice2018: John Wiley & Sons.

24. Streetman, B.G. and S. Banerjee, Solid state electronic devices2006: Pearson Prentice Hall.

25. Balkan, N. and A. Erol, Semiconductors for Optoelectronics2021: Springer.

26. Becquerel, M., Mémoire sur les effets électriques produits sous l'influence des rayons solaires. Comptes rendus hebdomadaires des séances de l'Académie des sciences, 1839. **9**: p. 561-567.

27. Green, M.A., Photovoltaic principles. Physica E: Low-dimensional Systems and Nanostructures, 2002. **14**(1-2): p. 11-17.

28. Fritts, C.E., On a new form of selenium cell, and some electrical discoveries made by its use. American Journal of Science, 1883. **3**(156): p. 465-472.

29. Zaidi, B., Introductory chapter: Introduction to photovoltaic effect. Solar Panels and Photovoltaic Materials, 2018: p. 1-8.

30. Chapin, D.M., C.S. Fuller, and G.L. Pearson, A new silicon p-n junction photocell for converting solar radiation into electrical power. Journal of Applied Physics, 1954. **25**(5): p. 676-677.

31. Singh, R., G.F. Alapatt, and A. Lakhtakia, Making solar cells a reality in every home: Opportunities and challenges for photovoltaic device design. IEEE Journal of the Electron Devices Society, 2013. **1**(6): p. 129-144.

32. Bagher, A.M., M.M.A. Vahid, and M. Mohsen, Types of solar cells and application. American Journal of optics and Photonics, 2015. **3**(5): p. 94-113.

33. Baghzouz, Y., Basic photovoltaic theory. Handbook of Clean Energy Systems, 2015: p. 1-13.

34. Kasap, S.O., Principles of electronic materials and devices2006: Tata McGraw-Hill.

35. Kavaz, A., et al., Solar Tree Project, 2014.

36. Tao, Y., Screen-printed front junction n-type silicon solar cells2016: IntechOpen.

37. Zeman, M., Introduction to photovoltaic solar energy. Delft University of Technology, 2003. **2**(6).

38. Markvart, T. and L. Castaner, Solar Cells: Materials. Manufacturing and Operation, 2005. **84**.

39. Smets, A.H., et al., Solar Energy: The physics and engineering of photovoltaic conversion, technologies and systems2015: UIT Cambridge.

40. McEvoy, A., L. Castaner, and T. Markvart, Solar cells: materials, manufacture and operation2012: Academic Press.

41. Moliton, A., Electronique et optoélectronique organiques. Vol. 37. 2011: Springer.

42. Ramalingam, K. and C. Indulkar, Solar energy and photovoltaic technology. Distributed Generation Systems, 2017: p. 69-147.

43. Maiti, C.K., Computer aided design of micro-and nanoelectronic devices2016: World Scientific.

44. Abdullah, M., et al., Research and development efforts on texturization to reduce the optical losses at front surface of silicon solar cell. Renewable and sustainable energy reviews, 2016. **66**: p. 380-398.

45. Nayfeh, M., Advanced and low cost energy and lighting devices. Fundam. Appl. Nano Silicon Plasmonics Fullerines, 2018. **2018**: p. 363-429.

46. Lin, P., et al., Numerical simulation of Cu2ZnSnS4 based solar cells with In2S3 buffer layers by SCAPS-1D. Journal of Applied Science and Engineering, 2014. **17**(4): p. 383-390.

47. Liang, L., et al., Efficient perovskite solar cells by reducing interface-mediated recombination: a bulky amine approach. Advanced Energy Materials, 2020. **10**(14): p. 2000197.

48. Heidarzadeh, H., A. Rostami, and M. Dolatyari, Management of losses (thermalization-transmission) in the Si-QDs inside 3C–SiC to design an ultra-high-efficiency solar cell. Materials Science in Semiconductor Processing, 2020. **109**: p. 104936.

49. Zuo, L., et al., Tackling energy loss for high-efficiency organic solar cells with integrated multiple strategies. Advanced Materials, 2018. **30**(16): p. 1706816.

50. Green, M.A., Solar cells: operating principles, technology, and system applications. Englewood Cliffs, 1982.

51. Qin, J., et al., The effect of solar cell shunt resistance change on the bus voltage ripple in spacecraft power system. Microelectronics Reliability, 2018. **88**: p. 1047-1050.

52. Niu, W., et al., Photoresponse enhancement of Cu2O solar cell with sulfur-doped ZnO buffer layer to mediate the interfacial band alignment. Solar Energy Materials and Solar Cells, 2016. **144**: p. 717-723.

53. Fujimoto, K., et al. Fabrication and characterization of copper oxide-zinc oxide solar cells prepared by electrodeposition. in Journal of Physics: Conference Series. 2013. IOP Publishing.

54. Biccari, F., Defects and doping in Cu2O2009: Lulu. com.

55. Zoolfakar, A.S., et al., Nanostructured copper oxide semiconductors: a perspective on materials, synthesis methods and applications. journal of materials chemistry c, 2014. **2**(27): p. 5247-5270.

56. Chen, K., et al., Polymorphic crystallization of Cu 2 O compound. CrystEngComm, 2014. **16**(24): p. 5257-5267.

57. Murali, D.S. and A. Subrahmanyam, Synthesis of low resistive p type Cu4O3 thin films by DC reactive magnetron sputtering and conversion of Cu4O3 into CuO by laser irradiation. Journal of Physics D: Applied Physics, 2016. **49**(37): p. 375102.

58. Wang, Y., et al., Electronic structures of C u 2 O, C u 4 O 3, and CuO: A joint experimental and theoretical study. Physical Review B, 2016. **94**(24): p. 245418.

59. Zheng, W., et al., The phase evolution and physical properties of binary copper oxide thin films prepared by reactive magnetron sputtering. Materials, 2018. **11**(7): p. 1253.

60. Živković, A., A. Roldan, and N.H. De Leeuw, Density functional theory study explaining the underperformance of copper oxides as photovoltaic absorbers. Physical Review B, 2019. **99**(3): p. 035154.

61. Young, J.A., Copper (I) Oxide, Cu2O. Journal of Chemical Education, 2003. **80**(3): p. 257.

62. Nandy, S., et al., A review on Cu2O and CuI-based p-type semiconducting transparent oxide materials: promising candidates for new generation oxide based electronics. Reviews in Advanced Sciences and Engineering, 2013. **2**(4): p. 273-304.

63. Soon, A., et al., Native defect-induced multifarious magnetism in nonstoichiometric cuprous oxide: First-principles study of bulk and surface properties of Cu 2− δ O. Physical Review B, 2009. **79**(3): p. 035205.

64. Zhang, L., L. McMillon, and J. McNatt, Gas-dependent bandgap and electrical conductivity of Cu2O thin films. Solar Energy Materials and Solar Cells, 2013. **108**: p. 230-234.

65. Brandt, I., et al., Electrodeposition of Cu2O: growth, properties, and applications. Journal of Solid State Electrochemistry, 2017. **21**(7): p. 1999-2020.

66. Ke, N.H., et al., The characteristics of IGZO/ZnO/Cu2O: Na thin film solar cells fabricated by DC magnetron sputtering method. Journal of Photochemistry and Photobiology A: Chemistry, 2017. **349**: p. 100-107.

67. Minami, T., Y. Nishi, and T. Miyata, Efficiency enhancement using a Zn1− xGex-O thin film as an n-type window layer in Cu2O-based heterojunction solar cells. Applied Physics Express, 2016. **9**(5): p. 052301.

68. Minami, T., Y. Nishi, and T. Miyata, Impact of incorporating sodium into polycrystalline p-type Cu2O for heterojunction solar cell applications. Applied physics letters, 2014. **105**(21): p. 212104.

69. Jacob, S.S.K., et al., Improving the conductivity of cuprous oxide thin film by doping Calcium via feasible nebulizer spray technique for solar cell (FTO/ZnO/Ca-Cu2O). Materials Research Express, 2019. **6**(4): p. 046405.

70. Kikuchi, N. and K. Tonooka, Electrical and structural properties of Ni-doped Cu2O films prepared by pulsed laser deposition. Thin solid films, 2005. **486**(1-2): p. 33-37.

71. Ivill, M., et al., Properties of Mn-doped Cu2O semiconducting thin films grown by pulsed-laser deposition. Solid-State Electronics, 2003. **47**(12): p. 2215-2220.

72. Resende, J., et al., Grain-boundary segregation of magnesium in doped cuprous oxide and impact on electrical transport properties. Scientific reports, 2021. **11**(1): p. 1-10.

73. Wang, Y., et al., Nitrogen chemical state in N-doped Cu2O thin films. Applied physics letters, 2017. **110**(13): p. 131902.

74. Elfadill, N.G., et al., Electrochemical deposition of Na-doped p-type Cu2O film on n-type Si for photovoltaic application. Journal of Electroanalytical Chemistry, 2016. **767**: p. 7-12.

75. Meyer, B., et al., Binary copper oxide semiconductors: From materials towards devices. physica status solidi (b), 2012. **249**(8): p. 1487-1509.

76. Siripala, W., et al., Study of annealing effects of cuprous oxide grown by electrodeposition technique. Solar Energy Materials and Solar Cells, 1996. **44**(3): p. 251-260.

77. Fernando, C. and S. Wetthasinghe, Investigation of photoelectrochemical characteristics of n-type Cu2O films. Solar Energy Materials and Solar Cells, 2000. **63**(3): p. 299-308.

78. Han, K. and M. Tao, Electrochemically deposited p–n homojunction cuprous oxide solar cells. Solar Energy Materials and Solar Cells, 2009. **93**(1): p. 153-157.

79. Jayewardena, C., et al., Fabrication of n-Cu2O electrodes with higher energy conversion efficiency in a photoelectrochemical cell. Solar Energy Materials and Solar Cells, 1998. **56**(1): p. 29-33.

80. Garuthara, R. and W. Siripala, Photoluminescence characterization of polycrystalline n-type Cu2O films. Journal of Luminescence, 2006. **121**(1): p. 173-178.

81. Wang, W., et al., p H-dependence of conduction type in cuprous oxide synthesized from solution. Journal of Applied Physics, 2010. **107**(12): p. 123717.

82. Scanlon, D.O. and G.W. Watson, Undoped n-type Cu2O: fact or fiction? The Journal of Physical Chemistry Letters, 2010. **1**(17): p. 2582-2585.

83. Scanlon, D.O. and G.W. Watson, Uncovering the complex behavior of hydrogen in Cu 2 O. Physical review letters, 2011. **106**(18): p. 186403.

84. Heinemann, M., B. Eifert, and C. Heiliger, Band structure and phase stability of the copper oxides Cu 2 O, CuO, and Cu 4 O 3. Physical Review B, 2013. **87**(11): p. 115111.

85. Raebiger, H., S. Lany, and A. Zunger, Origins of the p-type nature and cation deficiency in Cu 2 O and related materials. Physical Review B, 2007. **76**(4): p. 045209.

86. Wisz, G., et al., Morphology, composition, structure and optical properties of thermally annealed Cu2O thin films prepared by reactive DC sputtering method. Molecular Crystals and Liquid Crystals, 2018. **672**(1): p. 81-91.

87. Wang, Y., et al., Transmittance enhancement and optical band gap widening of Cu2O thin films after air annealing. Journal of Applied Physics, 2014. **115**(7): p. 073505.

88. Zhai, Y., et al., Morphology evolutions and optical properties of Cu2O films by an electrochemical deposition on flexible substrate. Applied Surface Science, 2012. **258**(7): p. 3232-3236.

89. Bergerot, L., Etude de l'élaboration d'oxyde transparent conducteur de type-p en couches minces pour des applications à l'électronique transparente ou au photovoltaïque, 2015, Université Grenoble Alpes.

90. Abdu, Y. and A. Musa, Copper (I) oxide (Cu2) based solar cells-a review. Bayero Journal of Pure and Applied Sciences, 2009. **2**(2): p. 8-12.

91. Bentarzi, H., Transport in metal-oxide-semiconductor structures: mobile ions effects on the oxide properties2011: Springer Science & Business Media.

92. Siripala, W.P., Electrodeposition of n-type cuprous oxide thin films. ECS Transactions, 2008. **11**(9): p. 1.

93. Katayama, J., et al., Performance of Cu2O/ZnO solar cell prepared by two-step electrodeposition. Journal of applied electrochemistry, 2004. **34**(7): p. 687-692.

94. Jayathilaka, C., et al., Improved efficiency of electrodeposited p-CuO/n-Cu2O heterojunction solar cell. Applied Physics Express, 2015. **8**(6): p. 065503.

95. Georgieva, V. and M. Ristov, Electrodeposited cuprous oxide on indium tin oxide for solar applications. Solar Energy Materials and Solar Cells, 2002. **73**(1): p. 67-73.

96. McShane, C.M. and K.-S. Choi, Photocurrent enhancement of n-type Cu2O electrodes achieved by controlling dendritic branching growth. Journal of the American Chemical Society, 2009. **131**(7): p. 2561-2569.

97. Brandt, I.S., et al., Electrical characterization of Cu/Cu2O electrodeposited contacts. ECS Transactions, 2008. **14**(1): p. 413.

98. Thörnberg, J., Synthesis and Characterization of Transition Metal Diborides, 2021, Linköping University Electronic Press.

99. Campbell, S.A., Fabrication engineering at the micro-and nanoscale2008.

100. Hishimone, P.N., H. Nagai, and M. Sato, Methods of fabricating thin films for energy materials and devices, in Lithium-ion Batteries-Thin Film for Energy Materials and Devices2020, IntechOpen.

101. Buitrago, E., A.M. Novello, and T. Meyer, Third-Generation Solar Cells: Toxicity and Risk of Exposure. Helvetica Chimica Acta, 2020. **103**(9): p. e2000074.

102. Shockley, W. and H.J. Queisser, Detailed balance limit of efficiency of p-n junction solar cells. Journal of Applied Physics, 1961. **32**(3): p. 510-519.

103. Georgieva, V., A. Tanusevski, and M. Georgieva, Low cost solar cells based on cuprous oxide. Solar Cells-Thin-Film Technologies, 2011: p. 55-56.

104. Korzhavyi, P.A. and B. Johansson, Literature review on the properties of cuprous oxide Cu {sub 2} O and the process of copper oxidation. 2011.

105. Siddiqui, H., et al., A review: synthesis, characterization and cell performance of Cu2O based material for solar cells. Oriental Journal Of Chemistry, 2012. **28**(3): p. 1533.

106. Xiong, L., et al., p-Type and n-type Cu2O semiconductor thin films: Controllable preparation by simple solvothermal method and photoelectrochemical properties. Electrochimica Acta, 2011. **56**(6): p. 2735-2739.

107. Fernando, C., et al., Investigation of n-type Cu2O layers prepared by a low cost chemical method for use in photo-voltaic thin film solar cells. Renewable energy, 2002. **26**(4): p. 521-529.

108. Siripala, W. and J. Jayakody, Observation of n-type photoconductivity in electrodeposited copper oxide film electrodes in a photoelectrochemical cell. Solar energy materials, 1986. **14**(1): p. 23-27.

109. McShane, C.M. and K.-S. Choi, Junction studies on electrochemically fabricated p–n Cu 2 O homojunction solar cells for efficiency enhancement. Physical Chemistry Chemical Physics, 2012. **14**(17): p. 6112-6118.

110. McShane, C.M., W.P. Siripala, and K.-S. Choi, Effect of junction morphology on the performance of polycrystalline Cu2O homojunction solar cells. The Journal of Physical Chemistry Letters, 2010. **1**(18): p. 2666-2670.

111. Minami, T., J. Yamazaki, and T. Miyata, Efficiency enhanced solar cells with a Cu2O homojunction grown epitaxially on p-Cu2O: Na sheets by electrochemical deposition. MRS Communications, 2016. **6**(4): p. 416-420.

112. Minami, T., et al., High-efficiency oxide heterojunction solar cells using Cu2O sheets. Japanese Journal of Applied Physics, 2004. **43**(7A): p. L917.

113. Mittiga, A., et al., Heterojunction solar cell with 2% efficiency based on a Cu 2 O substrate. Applied physics letters, 2006. **88**(16): p. 163502.

114. Izaki, M., et al., Electrochemically constructed p-Cu2O/n-ZnO heterojunction diode for photovoltaic device. Journal of Physics D: Applied Physics, 2007. **40**(11): p. 3326.

115. Minami, T., et al., High-efficiency oxide solar cells with ZnO/Cu2O heterojunction fabricated on thermally oxidized Cu2O sheets. Applied Physics Express, 2011. **4**(6): p. 062301.

116. Nishi, Y., T. Miyata, and T. Minami, The impact of heterojunction formation temperature on obtainable conversion efficiency in n-ZnO/p-Cu2O solar cells. Thin solid films, 2013. **528**: p. 72-76.

117. Minami, T., Y. Nishi, and T. Miyata, High-efficiency Cu2O-based heterojunction solar cells fabricated using a Ga2O3 thin film as n-type layer. Applied Physics Express, 2013. **6**(4): p. 044101.

118. Lee, Y.S., et al., Atomic layer deposited gallium oxide buffer layer enables 1.2 V open-circuit voltage in cuprous oxide solar cells. Advanced Materials, 2014. **26**(27): p. 4704-4710.

119. Ievskaya, Y., et al., Fabrication of ZnO/Cu2O heterojunctions in atmospheric conditions: Improved interface quality and solar cell performance. Solar Energy Materials and Solar Cells, 2015. **135**: p. 43-48.

120. Zang, Z., Efficiency enhancement of ZnO/Cu2O solar cells with well oriented and micrometer grain sized Cu2O films. Applied physics letters, 2018. **112**(4): p. 042106.

121. Miyata, T., et al., Photovoltaic properties of Cu2O-based heterojunction solar cells using n-type oxide semiconductor nano thin films prepared by low damage magnetron sputtering method. Journal of Semiconductors, 2019. **40**(3): p. 032701.

122. Miyata, T., et al., Photovoltaic properties of low-damage magnetron-sputtered n-type ZnO thin film/p-type Cu2O sheet heterojunction solar cells. Thin solid films, 2020. **697**: p. 137825.

123. Shibasaki, S., et al., Highly transparent Cu2O absorbing layer for thin film solar cells. Applied physics letters, 2021. **119**(24): p. 242102.

124. Özgür, Ü., et al., A comprehensive review of ZnO materials and devices. Journal of Applied Physics, 2005. **98**(4): p. 11.

125. Jagadish, C. and S.J. Pearton, Zinc oxide bulk, thin films and nanostructures: processing, properties, and applications2011: Elsevier.

126. Janotti, A. and C.G. Van de Walle, Fundamentals of zinc oxide as a semiconductor. Reports on progress in physics, 2009. **72**(12): p. 126501.

127. Adegoke, K.A., et al., Photocatalytic conversion of CO2 using ZnO semiconductor by hydrothermal method. 2018.

128. Diachenko, O.V., et al. The optimization of functional layers of solar cells based on n-ZnMgO/p-CuO and n-ZnMgO/p-Cu 2 O heterojunctions. in 2017 IEEE 7th International Conference Nanomaterials: Application & Properties (NAP). 2017. IEEE.

129. Hoggas, K., et al., Structural, microstructural, and optical properties of Zn_{1-x} Mg x O thin films grown onto glass substrate by ultrasonic spray pyrolysis. Applied Physics A, 2015. **120**(2): p. 745-755.

130. Kumar, S., et al., Nanoscale zinc oxide based heterojunctions as visible light active photocatalysts for hydrogen energy and environmental remediation. Catalysis Reviews, 2020. **62**(3): p. 346-405.

131. Horie, R., et al., Epitaxial growth of γ-(AlxGa1-x) 2O3 alloy thin films on spinel substrates via mist chemical vapor deposition. Journal of alloys and compounds, 2021. **851**: p. 156927.

132. Åhman, J., G. Svensson, and J. Albertsson, A reinvestigation of β-gallium oxide. Acta Crystallographica Section C: Crystal Structure Communications, 1996. **52**(6): p. 1336-1338.

133. Seacat, S., J.L. Lyons, and H. Peelaers, Orthorhombic alloys of Ga 2 O 3 and Al 2 O 3. Applied physics letters, 2020. **116**(23): p. 232102.

134. Peelaers, H., et al., Structural and electronic properties of Ga2O3-Al2O3 alloys. Applied physics letters, 2018. **112**(24): p. 242101.

135. Zhang, F., et al., Wide bandgap engineering of (AlGa) 2O3 films. Applied physics letters, 2014. **105**(16): p. 162107.

136. Zhang, Y., et al., Demonstration of high mobility and quantum transport in modulation-doped β-(AlxGa1-x) 2O3/Ga2O3 heterostructures. Applied physics letters, 2018. **112**(17): p. 173502.

137. Feng, Z., et al., Band alignment of SiO2/(AlxGa1-x) 2O3 ($0 \leq x \leq 0.49$) determined by X-ray photoelectron spectroscopy. Applied Surface Science, 2018. **434**: p. 440-444.

138. Zhang, J., et al., Recent progress on the electronic structure, defect, and doping properties of Ga2O3. APL Materials, 2020. **8**(2): p. 020906.

139. Wang, T., et al., Band gap and band offset of Ga 2 O 3 and (Al x Ga $_{1-}$ x) 2 O 3 alloys. Physical Review Applied, 2018. **10**(1): p. 011003.

140. Madhuri, K., Thermal protection coatings of metal oxide powders, in Metal Oxide Powder Technologies2020, Elsevier. p. 209-231.

141. Huang, J., et al., Ferroelectric thin films and nanostructures: current and future, in Nanostructures in Ferroelectric Films for Energy Applications2019, Elsevier. p. 19-39.

142. Pehkonen, S.O. and S. Yuan, The inorganic film coatings for corrosion protection, in Interface Science and Technology2018, Elsevier. p. 185-255.

143. Hashmi, S., Comprehensive materials processing2014: Newnes.

144. Oviroh, P.O., et al., New development of atomic layer deposition: processes, methods and applications. Science and technology of advanced materials, 2019. **20**(1): p. 465-496.

145. Puurunen, R.L., Surface chemistry of atomic layer deposition: A case study for the trimethylaluminum/water process. Journal of Applied Physics, 2005. **97**(12): p. 9.

146. Hwang, C., ALD (Atomic Layer Deposition) Process Technology in the Semiconductor Industry. Physics & High Technology, Jan/Feb, 2012: p. 37-41.

147. Minami, T., Y. Nishi, and T. Miyata, Effect of the thin Ga_2O_3 layer in n+-ZnO/n-Ga_2O_3/p-Cu_2O heterojunction solar cells. Thin solid films, 2013. **549**: p. 65-69.

148. Wilhelm, H., H.-W. Schock, and R. Scheer, Interface recombination in heterojunction solar cells: Influence of buffer layer thickness. Journal of Applied Physics, 2011. **109**(8): p. 084514.

149. Akimoto, K., et al., Thin film deposition of Cu_2O and application for solar cells. Solar Energy, 2006. **80**(6): p. 715-722.

150. Chua, D., S.B. Kim, and R. Gordon, Enhancement of the open circuit voltage of Cu_2O/Ga_2O_3 heterojunction solar cells through the mitigation of interfacial recombination. AIP Advances, 2019. **9**(5): p. 055203.

151. Brandt, R.E., et al., Band offsets of n-type electron-selective contacts on cuprous oxide (Cu_2O) for photovoltaics. Applied physics letters, 2014. **105**(26): p. 263901.

152. Clugston, D.A. and P.A. Basore. PC1D version 5: 32-bit solar cell modeling on personal computers. in Conference Record of the Twenty Sixth IEEE Photovoltaic Specialists Conference-1997. 1997. IEEE.

153. Burgelman, M., P. Nollet, and S. Degrave, Modelling polycrystalline semiconductor solar cells. Thin solid films, 2000. **361**: p. 527-532.

154. Liu, Y., Y. Sun, and A. Rockett, A new simulation software of solar cells—wxAMPS. Solar Energy Materials and Solar Cells, 2012. **98**: p. 124-128.

155. Froitzheim, A., et al. AFORS-HET: a computer-program for the simulation of heterojunction solar cells to be distributed for public use. in 3rd World Conference onPhotovoltaic Energy Conversion, 2003. Proceedings of. 2003. IEEE.

156. Burgelman, M., et al., Advanced electrical simulation of thin film solar cells. Thin solid films, 2013. **535**: p. 296-301.

157. Kim, K., et al., Simulations of chalcopyrite/c-Si tandem cells using SCAPS-1D. Solar Energy, 2017. **145**: p. 52-58.

158. Hadjab, M., et al., A numerical optimization study of CdS and Mg0. 125Zn0. 875O buffer layers in CIGS-based solar cells using wx AMPS-1D package. International Journal of Modelling and Simulation, 2022. **42**(2): p. 179-191.

159. Liu, Y., Y. Sun, and A. Rockett, An improved algorithm for solving equations for intra-band tunneling current in heterojunction solar cells. Thin solid films, 2012. **520**(15): p. 4947-4950.

160. Varache, R., et al., Investigation of selective junctions using a newly developed tunnel current model for solar cell applications. Solar Energy Materials and Solar Cells, 2015. **141**: p. 14-23.

161. Nakanishi, A., Y. Takiguchi, and S. Miyajima, Device simulation of CH3NH3PbI3 perovskite/heterojunction crystalline silicon monolithic tandem solar cells using an n-type a-Si: H/p-type μc-Si1–xOx: H tunnel junction. physica status solidi (a), 2016. **213**(7): p. 1997-2002.

162. Zahari, S.M., et al. The comparison between gallium arsenide and indium gallium arsenide as materials for solar cell performance using Silvaco application. in AIP Conference Proceedings. 2015. AIP Publishing LLC.

163. Sharma, H., P. Alvi, and J. Akhtar, A Simple model for complex fabrication of MEMS based Pressure Sensor: A Challenging Approach. Sensors & Transducers, 2010. **119**(8): p. 30.

164. Maiti, C.K., Introducing Technology Computer-Aided Design (TCAD): Fundamentals, Simulations, and Applications2017: CRC Press.

165. Sarkar, C., Technology computer aided design2018: CRC Press Boca Raton, FL.

166. ATLAS, A.U.M., Silvaco International. Santa Clara, CA, 2015.

167. Manual, A.U.s., Device Simulation Software, Version 5.20. 2. R, SILVACO International, Santa Clara, CA, 2015.

168. Sze, S.M. and M.-K. Lee, Semiconductor Devices: Physics and Technology: Physics and Technology2012: Wiley Global Education.

169. Simon M. Sze, K.K.N., Physics of Semiconductor Devices. third ed2006.

170. file:///D:Download/Silvacomanual_1.pdf.

171. Saha, S.K. and C. Sarkar, Introduction to technology computer aided design, in Technology Computer Aided Design: Simulation for VLSI MOSFET2013, CRC Press Boca Raton, FL. p. 1.

172. Zandi, B., D. Vasileska, and P. Wijewarnasuriya, Modeling Mercury Cadmium Telluride (HgCdTe) Photodiodes, 2009, ARMY RESEARCH LAB ADELPHI MD SENSORS AND ELECTRON DEVICES DIRECTORATE.

173. Bouhdjar, A., Study and numerical simulation of (a-Si: H/μc-Si: H) heterojunction solar cells. Etude et simulation numérique des cellules solaires à hétérojonction (a-Si: H/μc-Si: H, 2016, Université Mohamed Khider-Biskra.

174. Manual, A.U.s., Device Simulation Software, Version 5.20. 2. R, SILVACO International, Santa Clara, CA, 2016.

175. Michael, S., A. Bates, and M. Green. Silvaco ATLAS as a solar cell modeling tool. in Conference Record of the Thirty-first IEEE Photovoltaic Specialists Conference, 2005. 2005. IEEE.

176. Michalopoulos, P., A novel approach for the development and optimization of state-of-the-art photovoltaic devices using Silvaco, 2002, NAVAL POSTGRADUATE SCHOOL MONTEREY CA.

177. Wadia, C., A.P. Alivisatos, and D.M. Kammen, Materials availability expands the opportunity for large-scale photovoltaics deployment. Environmental science & technology, 2009. **43**(6): p. 2072-2077.

178. Ruhle, S., et al., All-oxide photovoltaics. The Journal of Physical Chemistry Letters, 2012. **3**(24): p. 3755-3764.

179. Robertson, J. and S. Clark, Limits to doping in oxides. Physical Review B, 2011. **83**(7): p. 075205.

180. Lee, Y.S., et al., Ultrathin amorphous zinc-tin-oxide buffer layer for enhancing heterojunction interface quality in metal-oxide solar cells. Energy & Environmental Science, 2013. **6**(7): p. 2112-2118.

181. Minami, T., et al., Effect of ZnO film deposition methods on the photovoltaic properties of ZnO–Cu2O heterojunction devices. Thin solid films, 2006. **494**(1-2): p. 47-52.

182. Musselman, K.P., et al., A novel buffering technique for aqueous processing of zinc oxide nanostructures and interfaces, and corresponding improvement of

electrodeposited ZnO-Cu2O photovoltaics. Advanced Functional Materials, 2011. **21**(3): p. 573-582.

183. Scheer, R., Activation energy of heterojunction diode currents in the limit of interface recombination. Journal of Applied Physics, 2009. **105**(10): p. 104505.

184. Minami, T., Y. Nishi, and T. Miyata, Heterojunction solar cell with 6% efficiency based on an n-type aluminum–gallium–oxide thin film and p-type sodium-doped Cu2O sheet. Applied Physics Express, 2015. **8**(2): p. 022301.

185. Takiguchi, Y. and S. Miyajima, Device simulation of cuprous oxide heterojunction solar cells. Japanese Journal of Applied Physics, 2015. **54**(11): p. 112303.

186. Rizi, M.T., M.S. Abadi, and M. Ghaneii, Two dimensional modeling of Cu2O heterojunction solar cells based-on β-Ga2O3 buffer. Optik, 2018. **155**: p. 121-132.

187. Nordseth, Ø., et al., Metal Oxide Thin-Film Heterojunctions for Photovoltaic Applications. Materials, 2018. **11**(12): p. 2593.

188. Rizi, M.T. and M.S. Abadi, Numerical investigation on efficiency improvement of double layer antireflection coating AZO/buffer/Cu 2 O/CuO on back-surface fluorine-doped tin oxide heterostructure solar cells. JOSA B, 2019. **36**(4): p. 1155-1165.

189. Chevallier, C., et al., Numerical investigations of the impact of buffer germanium composition and low cost fabrication of Cu2O on AZO/ZnGeO/Cu2O solar cell performances. EPJ Photovoltaics, 2021. **12**(3).

190. Khoshsirat, N., et al., Analysis of absorber and buffer layer band gap grading on CIGS thin film solar cell performance using SCAPS. Pertanika J. Sci. Technol., 2015. **23**(2): p. 241-250.

191. McCandless, B. and S. Hegedus. Influence of CdS window layers on thin film CdS/CdTe solar cell performance. in The Conference Record of the Twenty-Second IEEE Photovoltaic Specialists Conference-1991. 1991. IEEE.

192. Minami, T., et al., Photovoltaic properties in Al-doped ZnO/non-doped Zn1-XMgXO/Cu2O heterojunction solar cells. ECS Transactions, 2013. **50**(51): p. 59.

193. Minami, T., T. Miyata, and Y. Nishi, Efficiency improvement of Cu2O-based heterojunction solar cells fabricated using thermally oxidized copper sheets. Thin solid films, 2014. **559**: p. 105-111.

194. Ahmad, W., et al., Optimization of Thin-Film Carbon Nitride (C2N) based solar cell via Zn1− xMgxO as a buffer layer. 2022.

195. Lee, S.W., et al., Improved Cu2O-based solar cells using atomic layer deposition to control the Cu oxidation state at the p-n Junction. Advanced Energy Materials, 2014. **4**(11): p. 1301916.

196. Gao, S., et al., Interfaces of high-efficiency kesterite Cu2ZnSnS (e) 4 thin film solar cells. Chinese Physics B, 2018. **27**(1): p. 018803.

197. Liu, Z., et al., Energy-band alignments at ZnO/Ga2O3 and Ta2O5/Ga2O3 heterointerfaces by X-ray photoelectron spectroscopy and electron affinity rule. Journal of Applied Physics, 2019. **126**(4): p. 045707.

198. Ding, C., et al., Effect of the conduction band offset on interfacial recombination behavior of the planar perovskite solar cells. Nano Energy, 2018. **53**: p. 17-26.

199. Resende, J.A., Copper-based p-type semiconducting oxides: from materials to devices, 2017.

200. Islam, M.T., et al., Numerical simulation studies of Cs3Bi2I9 perovskite solar device with optimal selection of electron and hole transport layers. Optik, 2021. **231**: p. 166417.

201. Li, S., et al., A brief review of hole transporting materials commonly used in perovskite solar cells. Rare Metals, 2021. **40**(10): p. 2712-2729.

202. Umar, A., et al., Modeling and Simulation of Tin Sulfide (SnS)-Based Solar Cell Using ZnO as Transparent Conductive Oxide (TCO) and NiO as Hole Transport Layer (HTL). Micromachines, 2022. **13**(12): p. 2073.

203. Shamna, M., K. Nithya, and K. Sudheer, Simulation and optimization of CH3NH3SnI3 based inverted perovskite solar cell with NiO as Hole transport material. Materials Today: Proceedings, 2020. **33**: p. 1246-1251.

204. Alam, I. and M.A. Ashraf, Effect of different device parameters on tin-based perovskite solar cell coupled with In2S3 electron transport layer and CuSCN and Spiro-OMeTAD alternative hole transport layers for high-efficiency performance. Energy Sources, Part A: Recovery, Utilization, and Environmental Effects, 2020: p. 1-17.

205. Casas, G., et al., Analysis of the power conversion efficiency of perovskite solar cells with different materials as Hole-Transport Layer by numerical simulations. Superlattices and Microstructures, 2017. **107**: p. 136-143.

206. Azri, F., et al., Electron and hole transport layers optimization by numerical simulation of a perovskite solar cell. Solar Energy, 2019. **181**: p. 372-378.

207.	Pandey, K., A.K. Patel, and R. Mishra, Numerical study on performance enhancement of CZTSSe solar cells with Cu2O and MoTe2 as hole transport layer. Journal of Computational Electronics, 2022. **21**(4): p. 895-904.

208.	Sobayel, K., et al., NUMERICAL MODELING ON PROSPECTIVE BUFFER LAYERS FOR TUNGSTEN DI-SULFIDE (WS 2) SOLAR CELLS BY SCAPS-1D. Chalcogenide Letters, 2018. **15**(6).

209.	Stanić, D., et al., Simulating the performance of a formamidinium based mixed cation lead halide perovskite solar cell. Materials, 2021. **14**(21): p. 6341.

210.	Sawicka-Chudy, P., et al. Numerical analysis and optimization of Cu2O/TiO2, CuO/TiO2, heterojunction solar cells using SCAPS. in Journal of Physics: Conference Series. 2018. IOP Publishing.

211.	Yu, X., et al., Numerical simulation analysis of effect of energy band alignment and functional layer thickness on the performance for perovskite solar cells with Cd1-xZnxS electron transport layer. Materials Research Express, 2020. **7**(10): p. 105906.

212.	Ahmed, A., et al., Performance optimization of CH3NH3Pb (I1-xBrx) 3 based perovskite solar cells by comparing different ETL materials through conduction band offset engineering. Optical Materials, 2020. **105**: p. 109897.

213.	Bag, A., et al., Effect of absorber layer, hole transport layer thicknesses, and its doping density on the performance of perovskite solar cells by device simulation. Solar Energy, 2020. **196**: p. 177-182.

214.	Rai, S., B. Pandey, and D. Dwivedi, Modeling of highly efficient and low cost CH3NH3Pb (I1-xClx) 3 based perovskite solar cell by numerical simulation. Optical Materials, 2020. **100**: p. 109631.

215.	Lin, L., et al., A modeled perovskite solar cell structure with a Cu2O hole-transporting layer enabling over 20% efficiency by low-cost low-temperature processing. Journal of Physics and Chemistry of Solids, 2019. **124**: p. 205-211.

216.	Alkhammash, H.I., et al., Design and defect study of Cs2AgBiBr6 double perovskite solar cell using suitable charge transport layers. Semiconductor science and technology, 2022. **38**(1): p. 015005.

217.	Gautam, S., et al., Performance analysis of WSe2 solar cell with Cu2O hole transport layer by optimization of electrical and optical properties. Journal of Computational Electronics, 2022. **21**(6): p. 1373-1385.

218.	Mandal, L., et al., Band offset engineering for p-SnO/n-mc-Si heterojunction solar cell. Applied physics letters, 2020. **116**(23): p. 234106.

219. Sylla, A., S. Touré, and J. Vilcot, Theoretical analysis of the effects of band gaps and the conduction band offset of ZnS-CIGS layers, as well as defect layer thickness. Int. J. Sci. Res, 2017. **6**(11): p. 855-861.

220. Kim, J. and B. Shin, Strategies to reduce the open-circuit voltage deficit in Cu2ZnSn (S, Se) 4 thin film solar cells. Electronic Materials Letters, 2017. **13**(5): p. 373-392.

221. Song, T., A. Kanevce, and J.R. Sites, Emitter/absorber interface of CdTe solar cells. Journal of Applied Physics, 2016. **119**(23): p. 233104.